

MODELING AND SIMULATION OF THE BOILING CRISIS
WITHIN PWR AT CFD SCALE

LUC FAVRE

Improving the Modeling of Wall Boiling for Multiphase CFD Simulations

Paris, December 2022

test

ABSTRACT

To write!

PUBLICATIONS

Some ideas and figures have appeared previously in the following publications:

Put your publications from the thesis here. The packages `multibib` or `bibtopic` etc. can be used to handle multiple different bibliographies in your document.

We have seen that computer programming is an art,
because it applies accumulated knowledge to the world,
because it requires skill and ingenuity, and especially
because it produces objects of beauty.

— knuth:1974 [knuth:1974]

ACKNOWLEDGEMENTS

Put your acknowledgements here.

Many thanks to everybody who already sent me a postcard!

Regarding the typography and other help, many thanks go to Marco Kuhlmann, Philipp Lehman, Lothar Schlesier, Jim Young, Lorenzo Pantieri and Enrico Gregorio¹, Jörg Sommer, Joachim Köstler, Daniel Gottschlag, Denis Aydin, Paride Legovini, Steffen Prochnow, Nicolas Repp, Hinrich Harms, Roland Winkler, and the whole L^AT_EX-community for support, ideas and some great software.

Regarding LyX: The LyX port was initially done by Nicholas Mariette in March 2009 and continued by Ivo Pletikosić in 2011. Thank you very much for your work and the contributions to the original style.

¹ Members of GuIT (Gruppo Italiano Utilizzatori di T_EX e L^AT_EX)

CONTENTS

I	INTRODUCTION	1
II	MODELING AND SIMULATION OF BOILING FLOWS USING CFD	2
1	NEPTUNE_CFD CODE	3
1.1	Introduction	3
1.2	Governing Equations for Turbulent Boiling Bubbly Flows	3
1.2.1	Mass Conservation :	4
1.2.2	Momentum Balance :	4
1.2.3	Energy Conservation :	4
1.3	Interfacial transfers closure laws	4
1.3.1	Heat and mass transfers :	4
1.3.2	Interfacial Forces :	5
1.4	Turbulence Modeling	6
1.5	Wall Boiling Model	6
1.6	Wall Function for Dispersed Boiling Flows	7
2	THE DEBORA DATABASE	8
2.1	Introduction	8
2.2	Simulating PWR water using R12	8
2.2.1	Conservation of the Phase Density Ratio	9
2.2.2	Conservation of the Weber Number	9
2.2.3	Conservation of the Boiling Number	10
2.2.4	Conservation of the Inlet Thermodynamic Quality	11
2.2.5	Same Geometry	11
2.2.6	Transposition ranges	11
2.3	Description of the Test Section	11
2.3.1	Geometrical Description	11
2.3.2	Measurement Instrumentation	12
2.4	Measurements Campaigns and Results	14
2.4.1	Cases Nomenclature and Test Series	14
2.4.2	Verification of Control Parameters Coherency	15
2.4.3	Qualitative Analysis of the Experimental Results	16
2.5	Further Verifications	21
2.5.1	Reconstruction of the Applied Heat Flux	21
2.5.2	Comparison with One Dimensional Correlations	23
3	NEPTUNE_CFD SIMULATIONS OF DEBORA CASES	24
3.0.1	Investigating the nucleation site density modeling N_{sit}	25
III	DEVELOPMENT OF A NEW WALL HEAT FLUX PARTITIONING MODEL	27
4	INTRODUCTION	28
4.1	First Approaches : Correlations	28
5	EXISTING HEAT FLUX PARTITIONING MODELS	29
5.1	Kurul & Podowski (1990)	29
5.2	Basu (2000)	29
5.2.1	Case 1 : Bubble sliding, $D_d < s$	31
5.2.2	Case 2 : Bubble coalescence without sliding, $D_d \geq s$	32
5.3	Gilman (2017)	33
5.4	Zhou (2020)	34
5.5	Closure Laws for Remaining Parameters	35
5.5.1	Nucleation Site Density : N_{sit}	35
5.5.2	Bubble Departure Frequency f , Growth Time t_g and Wait Time t_w	36
6	BOILING BUBBLE DYNAMICS	37
6.1	Introduction	38

6.1.1	Experimental Insights	38
6.1.2	Existing Approaches	40
6.2	Bubble Force Balance in Vertical Flow Boiling	44
6.2.1	Introduction	44
6.2.2	General Considerations	45
6.2.3	Buoyancy Force	45
6.2.4	Contact Pressure Force	46
6.2.5	Capillary Force	46
6.2.6	Drag and Lift Forces	47
6.2.7	Inertia Force	51
6.2.8	Force Balance Summary	54
6.2.9	Liquid Velocity	54
6.3	Bubble Growth	55
6.3.1	Introduction	55
6.3.2	Heat Diffusion in Uniformly Superheated Liquid	56
6.3.3	Microlayer Evaporation	57
6.3.4	Bubble Growth in Subcooled Flow Boiling	58
6.3.5	Analytic Approach of Bubble Growth in a Linear Thermal Boundary Layer	59
6.3.6	Comparison with DNS Results	61
6.3.7	Comparison with Experimental Measurements	62
6.3.8	Conclusions on Bubble Growth Modeling	63
6.4	Departure by Sliding	65
6.4.1	Non-Dimensional Analysis	65
6.4.2	Application to Experimental Data	67
6.4.3	Departure Diameter Prediction	69
6.4.4	Discussion and accounting for parameters uncertainties	70
6.5	Sliding phase	73
6.5.1	Modeling	73
6.5.2	Low Pressure Sliding	73
6.5.3	High Pressure Sliding	74
6.5.4	Comparison of Forces in Sliding Stage	75
6.6	Bubble Lift-Off	78
6.6.1	Introduction	78
6.6.2	Experimental Measurements of Lift-Off Diameter	80
6.6.3	Influence of the Flow Boiling Conditions	80
6.6.4	Predicting the Lift-Off with a Force Balance	81
6.6.5	A Simple Non-Dimensional Correlation	83
6.6.6	Conclusion on the Lift-Off	83
7	CLOSURE LAWS FOR THE HEAT FLUX PARTITIONING MODEL	84
7.1	Single-Phase Heat Transfer Coefficient	84
7.2	Single Bubble Quenching Area	86
7.3	Growth time	86
7.3.1	Estimation of the thermal boundary layer thickness δ	87
7.3.2	Estimation of t_g against experimental data	87
7.4	Bubble Wait Time	88
7.5	Nucleation Site Density	89
7.6	Considerations on bubble interaction and nucleation sites deactivation	93
7.6.1	Static suppression	93
7.6.2	Static coalescence	93
7.6.3	Sliding coalescence	94
8	ASSEMBLING A NEW HEAT FLUX PARTITIONING MODEL	96
8.1	General description of the model	96
8.1.1	Convective heat fluxes	96
8.1.2	Boiling heat flux	97
8.1.3	Quenching heat flux	97
8.1.4	Needed closure relationships	97

IV TOWARDS THE INDUSTRIAL GEOMETRY	98
9 PROMOTEUR	99
9.1 Boiling freon in a tube with mixing vanes : DEBORA-Promoteur experiments	99
9.1.1 Description of the experiment	99
9.1.2 Analysis of the Experimental Measurements	99
9.1.3 NEPTUNE_CFD simulations of DEBORA-Promoteur cases	100
9.2 Liquid water flow in a tube with mixing vanes : AGATE-PROMOTEUR experiment	100
9.2.1 Description of the experiment	100
9.2.2 NEPTUNE_CFD simulations of AGATE-Promoteur case	101
V CONCLUSION	103
VI APPENDIX	104
A DETAILS ON THE BUBBLE GROWTH CALCULATION	105
A.0.1 Case 1 : δ_b is constant	107
A.0.2 Case 2 : $\delta_b = \sqrt{\eta_l t}$	107
A.0.3 Case 3 : $\delta_b = CR$	108
B DETAILS ON THE BUBBLE FORCE BALANCE	109
B.1 Appendix Section Test	110
B.2 Another Appendix Section Test	110
BIBLIOGRAPHY	112

LIST OF FIGURES

Figure 2.1	Density ratio of pressurized R12 and water 9
Figure 2.2	Weber number for R12 and water at $G = 2000 \text{ kg/m}^2/\text{s}$ and $R = 0.1 \text{ mm}$ 10
Figure 2.3	Boiling number for R12 and water at $G = 2000 \text{ kg/m}^2/\text{s}$ 10
Figure 2.4	Sketch of the DEBORA test section. Adapted from [17]. 12
Figure 2.5	Example of Phase Indicator Function signal 13
Figure 2.6	Picture of the bi-optical probe with a zoom over the two optical fibers. Reproduced from [gueguen_phd]. 13
Figure 2.7	30G2P26W16 and 29G2P26W16 results 17
Figure 2.8	8G2P26W16 results 18
Figure 2.9	30G2P14W16 and 29G2P14W16 results 19
Figure 2.10	8G2P14W16 results 20
Figure 2.11	Interpolation profiles for cases Te66 (Table 2.5). 22
Figure 3.1	NCFD (lines) vs. Exp. (circles) - T_L and T_w - Cases C8G2P26W16Te44.9, Te49.6, Te66.6 and Te70.3 - Simulations using two meshes M1 (coarse) and M2 (fine). 24
Figure 3.2	NCFD (lines) vs. Exp. (circles) - α , d_G and $U_{G,z}$ - Cases C30G2P26W16Te66.6 and Te70.6 - Simulations using two meshes M1 (coarse) and M2 (fine). 25
Figure 3.3	N_{sit} correlations of Lemmert & Chawla (left) and Hibiki & Ishii (right) vs. exp. data from literature. Operation pressures are displayed. $\pm 50\%$ error bars are drawn in black. 25
Figure 3.4	NCFD results for α , T_L and T_w using Lemmert & Chawla and Hibiki & Ishii correlation. Cases 8G2P26W23Te66.6 and Te70.3, 30G2P26W23Te66.6 and 70.6. 26
Figure 5.1	Sketch of the heat transfers zones considered by Basu <i>et al.</i> . (Adapted from [Basu2005]). 30
Figure 5.2	Sliding bubble behavior considered by Basu <i>et al.</i> . (Adapted from [Basu2005]) 31
Figure 6.1	Visualization of bubble sliding at various pressures. 38
Figure 6.2	Visualization of bubble sliding thermal impact. 39
Figure 6.3	Sketch of a typical bubble lifetime in vertical flow boiling. Left depicts a typical side view of the heater with identification of departure, sliding and lift-off. Right depicts a top view of the heater, exhibiting the area that will undergo transient heat transfer. 39
Figure 6.4	Sketch of the forces applied to the bubble facing an upward flow \overline{U}_L and sliding at velocity \overline{U}_b 45
Figure 6.5	Physical situation considered by Shi <i>et al.</i> [55]. 47
Figure 6.6	Drag correction from Shi <i>et al.</i> [55]. 48
Figure 6.7	C_L computed using Shi <i>et al.</i> correlation. 50
Figure 6.8	Values of the computed added mass coefficients in Eq. 6.60 and 6.62. 53
Figure 6.9	Microlayer appearing beneath the bubble in DNS conducted by and adapted from Urbano <i>et al.</i> [65]. 57
Figure 6.10	Studied geometry 59
Figure 6.11	Comparison with DNS results of Urbano <i>et al.</i> [64] ($\delta = 3\text{mm}$ and $\theta = 50^\circ$). Lines : Model predictions - Markers : DNS 62
Figure 6.12	Comparison with experimental measurements of Maity [35]. 62
Figure 6.13	Comparison with experimental measurements of Kossolapov [28]. ΔT_w values are recalculated from analytical growth profiles fitted by the author. 64
Figure 6.14	Regime map regarding departure by sliding. Boundaries plotted for water at 1 bar and $D_d = 0.5\text{mm}$. ($K = 2$) 66
Figure 6.15	Regime map plotted for water at different pressures and bubble departure diameters. ($K = 2$) 66
Figure 6.16	Regime map for R12 as simulating fluid for PWR. $D_d = 0.05\text{mm}$ is chosen according to R12 measurements from Garnier <i>et al.</i> [17] who observed bubbles of $\sim 0.1\text{mm}$ diameter after lift-off. The same value is taken for water. ($K = 2$) 67
Figure 6.17	Regime maps for each water data sets from Table ?? 68

Figure 6.18	Predicted bubble departure diameters. $\pm 50\%$ error bars are indicated.	71
Figure 6.19	Initially assumed, real and reassessed bubble shape for Sugrue cases (picture adapted from [59]).	71
Figure 6.20	Proposed model performance while accounting for contact angle uncertainties . .	72
Figure 6.21	Bubble sliding velocity predictions on Maity cases	74
Figure 6.22	Bubble sliding length predictions on Kossolapov cases - $P = 20$ bar	75
Figure 6.23	Bubble sliding length predictions on Kossolapov cases - $P = 40$ bar	76
Figure 6.24	Amplitude of each force during sliding	76
Figure 6.25	Visualization of bubble lift-off in horizontal boiling conducted by and adapted from Maity [35]. The detachment the the bubble base from the surface is clear in the last frame.	78
Figure 6.26	Visualization of bubble lift-off in vertical boiling. The moment when bubble leaves the surface appears less clearly than for horizontal boiling.	79
Figure 6.27	Visualization of boiling surfaces in vertical boiling, where single bubble lift-off is not systematically observed.	79
Figure 6.28	Evolution of D_{lo}/L_c depending on the flow conditions. Gunther: ∇ ; Griffith: Pentagons - Treshchev: \star ; Tolubinsky: \triangle ; Ünal: \diamond ; Maity: $+$; Prodanovic: \square ; Situ: \circ ; Chu: \triangleright ; Ahmadi: \triangleright ; Okawa: \times	82
Figure 7.1	Predictive capability of wall temperature by single-phase heat transfer correlations. $\pm 3K$ error bars indicated.	84
Figure 7.2	Predictive capability of wall temperature by NCFD law and Gnielinski correlation including corrections. $\pm 3K$ error bars indicated.	85
Figure 7.3	Comparison of the proposed model and Kommajoyusla model against experimental data from Unal. Black lines represent the $\pm 50\%$ error bars.	88
Figure 7.4	HSV Visualization of bubble density at various pressures adapted from Kossolapov [28] (left to right: 1.01 bar, 3 bar, 19.8 bar, 75.8 bar).	90
Figure 7.5	Sketch of the link between bubble contact angle and wettability / cavity flooding	90
Figure 7.6	Predictions of the chosen models against the experimental data of Table 7.5 with $\pm 50\%$ error bars. The contact angles	92
Figure 8.1	Sketch of the considered HFP	96
Figure 9.1	Picture of the mixing device (left) and its fine meshing (right).	99
Figure 9.2	NCFD (lines) vs. Exp. (circles) - α profiles for two MV positions ($23.5D_h$ in blue, $10D_h$ in orange) - $T_{in} = 65^\circ\text{C}$ (left), $T_{in} = 69^\circ\text{C}$ (middle), $T_{in} = 75^\circ\text{C}$ (right) - Simulations using two meshes M1 (coarse) and M2 (fine) for $T_{in} = 69^\circ\text{C}$	100
Figure 9.3	NCFD vs. Exp. - Top & Middle : Radial velocity and turbulent RMS ($z = 30\text{mm}$ & $z = 440\text{mm}$) - Bottom : Axial velocity and turbulent RMS ($z = 440\text{mm}$).	101
Figure A.1	Studied geometry	105

LIST OF TABLES

Table 2.1	Water R12 scaling, $R = 0.01\text{mm}$ for We	11
Table 2.2	Test matrix of the DEBORA cases. \bigcirc : C800 - \bigtriangledown : C2900 - \triangle : C3000	15
Table 2.3	Recalculated control parameters for the 30G2P14W16 cases. ($T_{sat} = 58.07^\circ\text{C}$)	16
Table 2.4	Recalculated control parameters for the 30G2P26W16 cases. ($T_{sat} = 86.81^\circ\text{C}$)	16
Table 2.5	Similar conditions cases between the C3000 and C800 campaigns. Outlet quality calculated with Eq. 2.9.	22
Table 2.6	Heat flux recalculation results	23
Table 6.1	Summary of the presented correlations	43
Table 6.2	Summary of different force-balance mechanistic approaches.	55
Table 6.3	Bubble departure diameters data sets in vertical flow boiling	67
Table 6.4	Average relative error reached by the models.	73
Table 6.5	Bubble lift-off diameters data sets in vertical flow boiling	81
Table 7.1	Experimental data range of wall temperature measurements from the single-phase part of boiling curves.	84
Table 7.2	Average errors achieved by the considered models on each data sets.	86
Table 7.3	Bubble growth time data in vertical flow boiling	88
Table 7.4	Bubble wait time data in vertical flow boiling	89
Table 7.5	Nucleation Site Density data in flow boiling	91
Table B.1	Autem usu id	110

LISTINGS

Listing B.1 A floating example (`listings` manual) 111

NOMENCLATURE

Acronyms

BC	Boiling Crisis
CHF	Critical Heat Flux
DNS	Direct Numerical Simulations
HFP	Heat Flux Partitioning
PWR	Pressurized Water Reactor
RPE	Rayleigh-Plesset Equation
SMR	Small Modular Reactor

Greek symbols

η	Thermal diffusivity [m ² /s]
γ	Shear rate [s ⁻¹]
λ	Thermal conductivity [W/m/K]
μ	Dynamic viscosity [J.s/m ⁻³]
ν	Kinematic viscosity [m ² /s]
ϕ	Heat flux [J/m ² /s]
ρ	Density [kg/m ³]
σ	Surface tension [J/m ²]
$\theta, d\theta$	Contact angle and half-hysteresis [° or rad]
θ_i	Bubble inclination angle [° or rad]

Latin symbols

C	Force coefficient [-]
D	Bubble diameter [m]
D_h	Hydraulic diameter [m]
E	Kinetic energy [J]
F	Force [N]
G	Mass flux [kg/m ² /s]
g	Gravity acceleration [m ² /s]
h_{LV}	Latent heat of vaporization [J/kg]
K	Bubble growth constant [-]
$L_c = \sqrt{\frac{\sigma}{(\rho_L - \rho_V)g}}$	Capillary length [m]
l_{sl}	Bubble sliding length [m]
R	Bubble radius [m]

R_c	Bubble curvature radius [m]
r_w	Bubble foot radius [m]
T	Temperature [K]
U	Velocity [m/s]
U_τ	Wall friction velocity [m/s]
$U_{rel} = U_L - U_b$	Relative velocity [m/s]
V	Volume [m^3]

Non-dimensional numbers

$\text{Ca} = \frac{\mu_L U_L}{\sigma}$	Capillary number [-]
$\text{Eo} = \frac{(\rho_L - \rho_V)gR^2}{\sigma}$	Eotvos number [-]
$\text{Fr} = \frac{\rho_L U_L^2}{(\rho_L - \rho_V)gR}$	Froude number [-]
$\text{Ja} = \frac{\rho_L c_{P,L} T - T_{sat} }{\rho_V h_{LV}}$	Jakob number [-]
$\text{Pr} = \frac{\nu}{\eta}$	Prandtl number [-]
$\text{Re}_b = \frac{U_{rel} D_b}{\nu_L}$	Bubble Reynolds number [-]
$\text{Re}_{D_h} = \frac{G_L D_h}{\mu_L}$	Liquid bulk Reynolds number [-]
$\text{Sr} = \frac{2\gamma R}{ U_{rel} }$	Non-dimensional shear rate [-]
$y^+ = \frac{y U_\tau}{\nu_L}$	Non-dimensional wall distance [-]

Subscripts

AM	Added-Mass
b	Bubble
D	Drag
d	Departure or Downstream
L	Liquid or Lift
lo	Lift-off
sat	Saturation
u	upstream
V	Vapor
w	Wall

ACRONYMS

CFD	Computational Fluid Dynamics
CMFD	Computational Multi-Fluid Dynamics
NCFD	NEPTUNE_CFD
DNS	Direct Numerical Simulation

NSD Nucleation Site Density

NOMENCLATURE

$N_{sit,0}$ Nucleation Site Density computed by correlation [m⁻²]

Part I
INTRODUCTION

Part II

MODELING AND SIMULATION OF BOILING FLOWS USING CFD

NEPTUNE_CFD CODE

Contents

1.1	Introduction	3
1.2	Governing Equations for Turbulent Boiling Bubbly Flows	3
1.2.1	Mass Conservation :	4
1.2.2	Momentum Balance :	4
1.2.3	Energy Conservation :	4
1.3	Interfacial transfers closure laws	4
1.3.1	Heat and mass transfers :	4
1.3.2	Interfacial Forces :	5
1.4	Turbulence Modeling	6
1.5	Wall Boiling Model	6
1.6	Wall Function for Dispersed Boiling Flows	7

1.1 INTRODUCTION

The NEPTUNE_CFD project (started in 2001) is a research program coordinated by four entities : EDF, CEA, IRSN and Framatome. The initial goals of the project were related to nuclear safety by developing a thermal-hydraulics simulation tool to :

- Predict the Boiling Crisis in PWR cores ;
- Study the Loss Of Coolant Accident (LOCA) to predict fuel rod cladding temperature.

The code consists of a local three-dimensional modeling based on a two-fluid one pressure approach combined with mass, momentum and energy conservation equations for each phase[Guelfi2007].
is an eulerian multiphase CFD solver co-developed

The constitutive equations are solved using a pressure correction, and is based on a finite-volume discretization along with a collocated arrangement of the variables. Moreover, NEPTUNE_CFD allows the use of all type of meshes (hexahedra, tetrahedra, pyramids, etc.), even non-conforming ones, thanks to its face-based data structure. Finally, the code is well-suited for parallel computing, widening its computing capacity to very large meshes.

The simulations presented in this thesis have all been conducted using the NEPTUNE_CFD 7.0 modeling framework for dispersed bubbly flows. In the next sections, we will detail the constitutive equations and closures laws of the code for the simulation of boiling bubbly flows.

1.2 GOVERNING EQUATIONS FOR TURBULENT BOILING BUBBLY FLOWS

To simulate two-phase dispersed boiling flows, NEPTUNE_CFD solves the ensemble-averaged equations of mass conservation, momentum balance and energy conservation for each phase. As a reminder, the ensemble-averaging of a physical quantity F_k for any phase k in a multiphase flows is defined as:

1.2.1 Mass Conservation :

$$\frac{\partial \alpha_k \rho_k}{\partial t} + \bar{\nabla} \cdot (\alpha_k \rho_k \bar{U}_k) = \Gamma_k \quad (1.1)$$

Where α_k , ρ_k , \bar{U}_k are the time fraction, average density and velocity of phase k ; $\Gamma_k = \Gamma_{k,i} + \Gamma_{k,w}$ the interfacial mass transfer term per unit of volume and time splitted between bulk and wall contribution. Subscripts $k = L$ or G denotes the liquid or gas phase, i the interfacial quantities and w the wall contribution.

1.2.2 Momentum Balance :

$$\frac{\partial \alpha_k \rho_k \bar{U}_k}{\partial t} + \bar{\nabla} \cdot (\alpha_k \rho_k \bar{U}_k \otimes \bar{U}_k) = -\alpha_k \bar{\nabla} (P) + \bar{F}_{k,i} + \Gamma_k \bar{U}_{k,i} + \alpha_k \rho_k \bar{g} + \bar{\nabla} \cdot (\alpha_k (\bar{\tau}_{k,m} + \bar{\tau}_{k,T})) \quad (1.2)$$

Where P is the pressure, \bar{g} the gravity, $\bar{F}_{k,i}$ the interfacial forces accounting for momentum transfer between phases per unit of volume and time, $\bar{U}_{k,i}$ the interfacial velocity, $\bar{\tau}_{k,m}$ and $\bar{\tau}_{k,T}$ respectively the viscous and turbulent (or Reynolds) stress tensor. Subscript m and T respectively denote the molecular (or laminar) and turbulent terms.

1.2.3 Energy Conservation :

$$\begin{aligned} \frac{\partial \alpha_k \rho_k H_k}{\partial t} + \bar{\nabla} \cdot (\alpha_k \rho_k H_k \bar{U}_k) &= \frac{\partial \alpha_k P}{\partial t} + \Gamma_k H_{k,i} + \bar{F}_{k,i} \cdot \bar{U}_k + Q_{k,I} + \bar{\nabla} \cdot (\alpha_k (\bar{\tau}_k + \bar{\tau}_{k,T}) \cdot \bar{U}_k) \\ &\quad + \bar{\nabla} \cdot (\alpha_k (-(\lambda_{k,m} + \lambda_{k,T}) \bar{\nabla} (T_k))) + \alpha_k \rho_k \bar{g} \cdot \bar{U}_k + Q_{k,w} \end{aligned} \quad (1.3)$$

Where $H_k = e_k + \frac{U_k^2}{2} + \frac{P}{\rho_k} = h_k + \frac{U_k^2}{2}$ is the total enthalpy of phase k , $H_{k,i}$ the interfacial-averaged enthalpy, $Q_{k,i}$ the interfacial heat flux per unit of volume and time, $\lambda_{k,m}$ and $\lambda_{k,T}$ respectively being the laminar and turbulent thermal conductivity, T_k the temperature, $Q_{k,w}$ the heat flux from the wall to phase k per unit of volume and time.

However, this ensemble-average approach requires a given number of closure laws since this operation removes most of the information about smaller scales physics such as interfacial exchanges between phases or wall-fluid interaction. Terms for which this modeling effort is needed are colored in orange in equations 1.1, 1.2 and 1.3. The chosen expressions for those terms are detailed in subsections 1.3, 1.4 and 1.5.

1.3 INTERFACIAL TRANSFERS CLOSURE LAWS

The interfacial transfers of mass, momentum and energy are respectively noted in equations 1.1, 1.2 and 1.3 : Γ_k , $\bar{F}_{k,i}$ and $Q_{k,i}$.

1.3.1 Heat and mass transfers :

The mass transfer term, can be written as : $\Gamma_{L,i} + \Gamma_{G,i} = 0$, $\Gamma_{L,w} + \Gamma_{G,w} = 0$ with $\Gamma_{G,w} \geq 0$ in the case of boiling flows. This finally gives $\Gamma_L = -\Gamma_G$.

The interfacial heat flux $Q_{k,i}$ can be rewritten in terms of interfacial area concentration a_i : $Q_{k,i} = q''_{k,i} a_i$. Neglecting the mechanical contribution compared to the thermal terms, the energy jump condition can then be expressed as :

$$\sum_{k=L,G} \left(\Gamma_{k,i} h_{k,i} + q''_{k,i} a_i \right) = 0 \quad (1.4)$$

The estimation of $h_{k,i}$ is not straightforward since it can either be supposed to be the saturation enthalpy of phase k at the system pressure (H1) or $h_{k,i}$ can be identified to the phase-averaged enthalpy (H2). In NEPTUNE_CFD, the assumption H2 is chosen, thus giving the bulk condensation rate :

$$\Gamma_{L,i} = \frac{a_i (q''_{L,i} + q''_{G,i})}{h_{G,sat} - h_{L,sat}} \quad (1.5)$$

The interfacial heat flux densities $q''_{k,i}$ and interfacial area concentration a_i are expressed as $q''_{k,i} = C_{k,i} (T_{sat}(P) - T_k)$ and $a_i = 6\alpha_G/d_G$, d_G being the gas phase Sauter mean bubble diameter. The interfacial area is computed using the transport equation of RUYER & SEILER [Ruyer2009]. For subcooled liquid, the following heat transfer coefficient is used [Manon2000]:

$$C_{L,i} = \frac{Nu_L \lambda_L}{d_G} \text{ and } Nu_L = 2 + 0.6 Re^{1/2} Pr_L^{1/3} \quad (1.6)$$

Where Re is the bubble Reynolds number $Re = ||\bar{U}_G - \bar{U}_L|| d_G / \nu_L$ and Pr_L the liquid Prandtl number $Pr_L = \nu_L / \eta_L$ with ν_L and η_L respectively being the liquid kinematic viscosity and thermal diffusivity. On the other hand, if the liquid is overheated, the maximum of three heat transfer coefficients accounting for different heat transfer mechanisms is taken [Berne1983]:

$$C_{L,i} = \max(C_{L,i,1}; C_{L,i,2}; C_{L,i,3}) \quad (1.7)$$

With $C_{L,i,n} = \lambda_L Nu_{L,n} / d_G$ and :

$$Nu_1 = \sqrt{\frac{4}{\pi} Pe} ; Nu_2 = 2 ; Nu_3 = \frac{12}{\pi} Ja \quad (1.8)$$

where $Pe = ||\bar{U}_G - \bar{U}_L|| d_G / \eta_L$ is the Peclet number and $Ja = \rho_L c_{p,L} |T_{sat} - T_L| / (\rho_g h_{lg})$ the Jakob number, with h_{lg} the latent heat of vaporization. Those three Nusselt numbers respectively correspond to convection heat transfer, stationary conduction and transient conduction.

For the gas phase, a simple law that ensures that the vapor temperature remains close to the saturation temperature is used (which is expected for small bubbles, *e.g.* in a PWR) :

$$C_{G,i} a_i = \frac{\alpha_G \rho_v c_{p,G}}{t_c} \quad (1.9)$$

where $c_{p,G}$ is the gas heat capacity at constant pressure, and t_c a characteristic (relaxation) time given by the user (default value being $t_c = 0.01s$) .

1.3.2 Interfacial Forces :

The interfacial momentum transfer (excluding transfer associated to transfer of mass Γ_k) is assumed to be composed of 4 different forces being the, drag D , the added mass AM , the lift L and the turbulent dispersion TD :

$$\overline{F_{k,i}} = \overline{F_{k,D}} + \overline{F_{k,AM}} + \overline{F_{k,L}} + \overline{F_{k,TD}} \quad (1.10)$$

The turbulent dispersion force $\overline{F_{k,TD}}$ originates from the averaging operation conducted on the three other forces' expressions, detailed in equations 1.11, 1.12, 1.13 and 1.14.

$$\overline{F_{G,D}} = -\overline{F_{L,D}} = -\frac{1}{8} a_i \rho_L C_D ||\bar{U}_G - \bar{U}_L|| (\bar{U}_G - \bar{U}_L) \quad (1.11)$$

$$\begin{aligned} \overline{F_{G,AM}} = -\overline{F_{L,AM}} = -C_{AM} \frac{1+2\alpha_G}{1-\alpha_G} \alpha_G \rho_L \\ \times \left[\left(\frac{\partial \bar{U}_G}{\partial t} + \bar{\nabla}(\bar{U}_G) \cdot \bar{U}_G \right) - \left(\frac{\partial \bar{U}_L}{\partial t} + \bar{\nabla}(\bar{U}_L) \cdot \bar{U}_L \right) \right] \end{aligned} \quad (1.12)$$

$$\overline{F_{G,L}} = -\overline{F_{L,L}} = -C_L \alpha_G \rho_L (\bar{U}_G - \bar{U}_L) \wedge (\bar{\nabla} \wedge \bar{U}_L) \quad (1.13)$$

$$\overline{F_{G,TD}} = -\overline{F_{L,TD}} = -\frac{2}{3} \alpha_L \alpha_G C_{TD} \bar{\nabla}(\alpha_G) \quad (1.14)$$

with C_D , C_{AM} , C_L and C_{TD} the associated forces coefficients, respectively taken from ISHII [Ishii1967], ZUBER [Zuber1964], TOMIYAMA [Tomiyama2002] and the Generalized Turbulent Dispersion model (GTD) from LAVIEVILLE *et al.* [Lavieville2017].

1.4 TURBULENCE MODELING

For bubbly flow simulations, only liquid phase turbulence is taken into account. The prescribed model is the Reynolds Stress Model (RSM) $R_{ij} - \varepsilon$ SSG from SPEZIALE, SARKAR and GATSKI [Speziale1991] adapted to two-phase boiling flows by MIMOUNI *et al.* [Mimouni2011].

$$\frac{\partial R_{ij}}{\partial t} + U_k \frac{\partial R_{ij}}{\partial x_k} = -R_{ik} \frac{\partial U_j}{\partial x_k} \quad (1.15)$$

1.5 WALL BOILING MODEL

The modeling of the heterogeneous boiling phenomenon at the wall is based on a Heat Flux Partitioning (HFP) model, inspired by KURUL & PODOWSKI original work [Kurul1990] who divided the wall heat flux density ϕ_w in three terms :

- A single phase convective heat flux $\phi_{c,L}$ heating the liquid through the fraction of the wall area unaffected by the vapor bubbles
- A vaporization heat flux ϕ_e which accounts for the generation of vapor through heterogeneous nucleation
- A quenching heat flux ϕ_q to represent the thermal impact of bubbles departing from the wall and being replaced by cool liquid

A fourth flux is added to this HFP in NEPTUNE_CFD, following MIMOUNI *et al.* [Mimouni2016] who consider a convective heat flux heating the vapour $\phi_{c,G}$ when the wall area is covered by a dense accumulation of bubbles.

The model thus gives Equation 8.1 :

$$\phi_w = \phi_{c,L} + \phi_e + \phi_q + \phi_{c,G} \quad (1.16)$$

The convective heat fluxes are expressed as $\phi_{c,k} = A_k h_{k,log} (T_w - T_k)$ with $h_{k,log} = \rho_k c_p, k u^* / T_L^+$; where A_k the fraction of the wall area facing phase k , T_w the wall temperature and $h_{k,log}$ the wall logarithmic convective heat transfer coefficient to phase k based on the wall functions for friction velocity u^* and non-dimensional liquid temperature T_L^+ described in 1.6.

The vaporization heat flux is computed following $\phi_e = N_{sit} f \rho_G h_{lg} \pi d_d^2 / 6$ with :

- N_{sit} the nucleation site density modeled as [Lemmert1977] : $N_{sit} = [210 (T_w - T_{sat})]^{1.8}$
- f the bubble detachment frequency expressed as [Cole1960] : $f = \sqrt{\frac{4}{3} \frac{g |\rho_v - \rho_l|}{\rho_l d_d}}$
- d_d the bubble detachment diameter given by Unal correlation [Unal1976] corrected by Borée *et al.* [ref] (Equation 1.17)

$$d_d = 2.42 \times 10^{-5} P^{0.709} \frac{a}{\sqrt{b\varphi}} \text{ with } a = \frac{(T_w - T_{sat}) \lambda_w}{2\rho_G h_{lg} \sqrt{\pi \eta_w}} \text{ and } b = \begin{cases} \frac{T_{sat} - T_L}{2(1 - \rho_G / \rho_L)}, & \text{if } St \leq 0.0065 \\ \frac{1}{2(1 - \rho_G / \rho_L)} \frac{\phi_{c,L} + \phi_e + \phi_q}{0.0065 \rho_L c_{p,L} ||\bar{U}_L||}, & \text{if } St > 0.0065 \end{cases} \quad (1.17)$$

where λ_w and η_w are the wall thermal conductivity and diffusivity, $St = \frac{\phi_{c,L} + \phi_e + \phi_q}{\rho_L c_{p,L} ||\bar{U}_L|| (T_{sat} - T_L)}$ is the Stanton number and $\varphi = \max \left(1; \left(\frac{||\bar{U}_L||}{U_0} \right)^{0.47} \right)$ with $U_0 = 0.61 \text{ m/s}$

Finally, the quenching heat flux follows the approach of DEL VALLE & KENNING [DelValle1985] supposing that it follows a semi-infinite transient conduction regime : $\phi_q = A_G t_q f \frac{2\lambda_L (T_w - T_L)}{\sqrt{\pi \eta_L t_q}}$ where t_q is the quenching time, supposed to be equal to $1/f$.

1.6 WALL FUNCTION FOR DISPERSED BOILING FLOWS

In boiling flows, the formation of bubbles at the wall may disturb the liquid velocity profile in the boundary layer. To take this phenomena into account, MIMOUNI *et al.* [Mimouni2016] proposed a wall function for boiling flows which tends to the single-phase formulation when $\alpha_G \rightarrow 0$ and depends on the bubble diameter and density at the wall :

$$u^+ = \frac{1}{\kappa} \ln(y^+) + B - \Delta u^+ \text{ with } \Delta u^+ = \begin{cases} 0 & \text{if } k_r^+ \leq 11.3 \\ \frac{1}{\kappa} \ln(1 + C_{kr} k_r^+) & \text{if } k_r^+ > 11.3 \end{cases} \quad (1.18)$$

where $\kappa=0.41$ is the Von Karman constant, $B = 5.3$ the standard single-phase logarithmic law constant. Δu^+ represents the offset of u^+ due to the wall roughness induced by the presence of bubble. We have $C_{kr} = 0.5$ and $k_r = \frac{k_r \sqrt{u^* u_T}}{\nu_L}$ the "roughness Reynolds number" with $u_T = C_\mu^{1/4} \sqrt{k_L}$ defined from the $k - \varepsilon$ constant $C_\mu = 0.09$ and k_L the liquid turbulent kinetic energy. Finally, $k_r = \alpha_G d_G$. The non-dimensional wall liquid temperature T_L^+ is modeled according to LEDUC[Leduc1995]:

$$T_L^+ = \begin{cases} Pr_L y^+, & \text{if } y^+ \leq 13.2 \\ 8.67 Pr_{L,T} \left(\frac{Pr_L}{Pr_{L,T}} - 1 \right) \left(\frac{Pr_{L,T}}{Pr_L} \right)^{0.25} + \frac{Pr_{L,T}}{\kappa} \ln(Ey^+) & \text{if } y^+ > 13.2 \end{cases} \quad (1.19)$$

With $Pr_{L,T} = 0.9$ the turbulent liquid Prandtl number, and $E = 7.76$ a constant for smooth walls.

2

THE DEBORA DATABASE

Contents

2.1	Introduction	8
2.2	Simulating PWR water using R12	8
2.2.1	Conservation of the Phase Density Ratio	9
2.2.2	Conservation of the Weber Number	9
2.2.3	Conservation of the Boiling Number	10
2.2.4	Conservation of the Inlet Thermodynamic Quality	11
2.2.5	Same Geometry	11
2.2.6	Transposition ranges	11
2.3	Description of the Test Section	11
2.3.1	Geometrical Description	11
2.3.2	Measurement Instrumentation	12
2.4	Measurements Campaigns and Results	14
2.4.1	Cases Nomenclature and Test Series	14
2.4.2	Verification of Control Parameters Coherency	15
2.4.3	Qualitative Analysis of the Experimental Results	16
2.5	Further Verifications	21
2.5.1	Reconstruction of the Applied Heat Flux	21
2.5.2	Comparison with One Dimensional Correlations	23

2.1 INTRODUCTION

The validation of any existing modeling of multiphase flows must rely on extensive databases from experimental investigations in operating conditions that are representative of industrial configurations in PWR. This naturally lead to an important demand for measurements of local phase-related properties of vertical pressurized subcooled boiling flows.

To meet this need, CEA and EDF built a test facility called DEBORA in the 1990's. Its goal was to establish a consistent database of local measurements of the flow structure for vertical subcooled boiling freon Refrigerant 12 (R12) from the Onset of Nucleate Boiling to the Boiling Crisis.

In this chapter, we will describe the test section and analyze the available results from past measurements campaigns.

2.2 SIMULATING PWR WATER USING R12

The choice of using R12 as the working fluid in the DEBORA loop emerged from the interesting properties that boiling freon presents when compared to the highly pressurized water in PWR cores. Indeed, the conditions for which the Boiling Crisis must be studied for water in PWR are:

- Pressure P between 100 and 180 bar ;
- Inlet liquid mass flux G between 1000 and 5000 kg/m²/s ;
- Wall heat flux ϕ_w between 0.5 and 6 MW/m² ;

- Inlet thermodynamic flow quality $x_{eq,in}$ between -0.4 and 0.4.

In those ranges, sensors dedicated to local measurements are not suited to sustain such conditions.

The experimental strategy is then to "simulate" the aimed industrial conditions using a different fluid. It has to present thermophysical properties that allow to reproduce non-dimensional numbers of the industrial flow using less constraining operating conditions.

This explains the choice of R12 as it permits to transpose relevant parameters for PWR as detailed below.

2.2.1 Conservation of the Phase Density Ratio

Freon 12 can reach the same density ratio as water in PWR using limited pressurized conditions no larger than 30 bars. It is an important parameter to mimic the behavior of the boiling two-phase flow since it has a strong influence over the bubble size for example [25].

$$\left(\frac{\rho_{V,sat}}{\rho_{L,sat}} \right)_{P_1}^{water} = \left(\frac{\rho_{V,sat}}{\rho_{L,sat}} \right)_{P_2}^{R12} \quad (2.1)$$

with $P_2 < P_1$.

The evolution of the density ratio of water and R12 with pressure are shown on Figure 2.1.

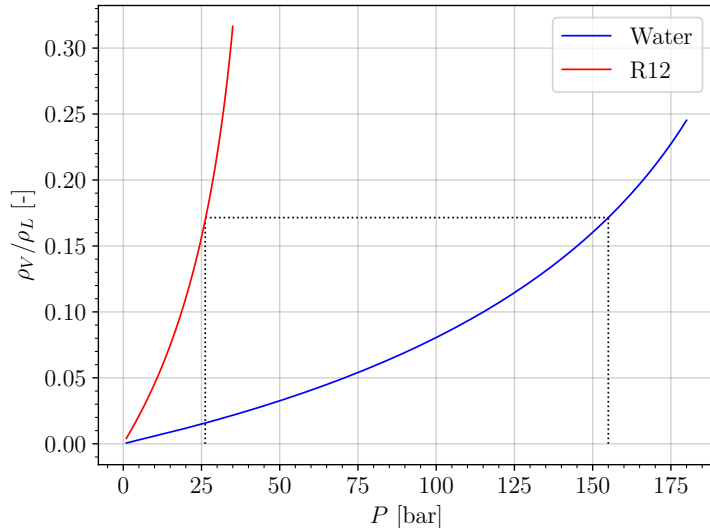


Figure 2.1: Density ratio of pressurized R12 and water

For instance, we can see that R12 at approximatively 26 bar ($T_{sat} \approx 86.8^\circ\text{C}$) has the same density ratio as water at 155 bar ($T_{sat} \approx 344.8^\circ\text{C}$).

Note : This tranposition criteria thus scales the operating pressure P of the experiment.

2.2.2 Conservation of the Weber Number

The Weber number is also similar to those encountered in PWR.

$$We = \frac{G^2 R}{\rho_L \sigma} \quad (2.2)$$

This number characterizes physical phenomena such as bubble break-up or deformation under the influence of the liquid inertia.

Similar to the phase density ratio, Figure 2.2 shows that Weber number equivalent to water at 155 bar can be reached with R12 around 23 bar.

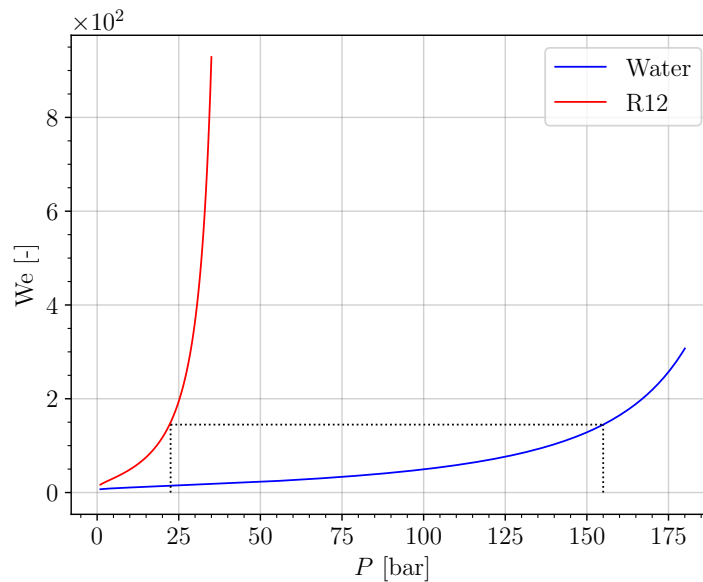


Figure 2.2: Weber number for R12 and water at $G = 2000 \text{ kg/m}^2/\text{s}$ and $R = 0.1 \text{ mm}$

Note : For a same value of R , this transposition scales the inlet liquid mass flux G .

2.2.3 Conservation of the Boiling Number

The boiling number is defined as:

$$\text{Bo} = \frac{\phi_w}{G h_{LV}} \quad (2.3)$$

It represents the comparison between the vapor mass flux ϕ_w/h_{LV} if all the heat flux contributes to phase change versus the inlet liquid mass flux. Thus, its value can be associated to the boiling and two-phase flow regime.

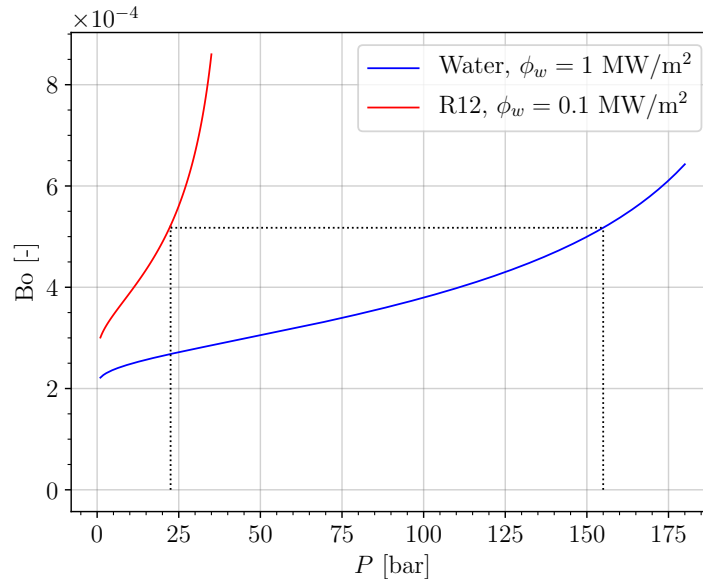


Figure 2.3: Boiling number for R12 and water at $G = 2000 \text{ kg/m}^2/\text{s}$

Figure 2.3 shows that Boiling number values similar to PWR can be reproduced using R12 with wall heat fluxes one order of magnitude lower and pressure around 23 bar.

Note : This transposition criteria scales the applied heat flux ϕ_w .

2.2.4 Conservation of the Inlet Thermodynamic Quality

Water in PWR being highly subcooled to avoid boiling, reproducing the inlet subcooling in the DEBORA experiment allows to mimic the early stages of boiling between the ONB and OSV. It allows to reproduce Boiling Crisis by Departure from Nucleate Boiling for low quality flows. This is achieved through the inlet thermodynamic quality:

$$x_{eq,in} = \frac{h_{L,in} - h_{L,sat}}{h_{LV}} \quad (2.4)$$

Note : This transposition is achieved by scaling the R12 inlet temperature.

2.2.5 Same Geometry

The last similarity achieved in the DEBORA experiment is related to the geometry. The heated length L_{ch} of the test section is similar to the height of a nuclear fuel assembly and the hydraulic diameter D_h is equal to that of a subchannel.

2.2.6 Transposition ranges

As a result of those conservation criteria, Table 2.1 sums up the transposition ranges for each parameters.

Fluid	Water	Freon R12
P [bar]	100 - 180	14 - 30
G [kg/m ² /s]	1000 - 5000	1000 - 5000
ϕ_w [MW/m ²]	0.5 - 6	0.05 - 0.65
$x_{eq,in}$ [-]	(-0.4) - (+0.4)	(-0.4) - (+0.4)
$\rho_{V,sat}/\rho_{L,sat}$ [-]	0.08 - 0.25	0.07 - 0.22
We [-]	49.5 - 307.1	69.1 - 365.8
$Bo \times 10^{-3}$ [-]	0.19 - 3.86	0.21 - 4.33

Table 2.1: Water R12 scaling, $R = 0.01\text{mm}$ for We

2.3 DESCRIPTION OF THE TEST SECTION

2.3.1 Geometrical Description

To apply the aforementioned transport criteria, four thermal-hydraulic control parameters are imposed in the test section:

- The outlet pressure P ;
- The inlet mass flow rate $G \times S_{in}$ with $S_{in} = \pi R^2 \approx 2.9 \times 10^{-4} \text{ m}^2$ the inlet area ;
- The inlet liquid temperature $T_{L,in}$;
- The electrical power transferred to the liquid $\phi_w \times S_{heat}$ with S_{heat} the heated area.

The test section is presented on Figure 2.4. It consists of an inconel tube with inner diameter $D_h = 19.2 \text{ mm}$, a 1 mm thickness and a heated length $L_{heat}=3.5 \text{ m}$. A detailed description of the whole experimental loop is given in Garnier *et al.* [17].

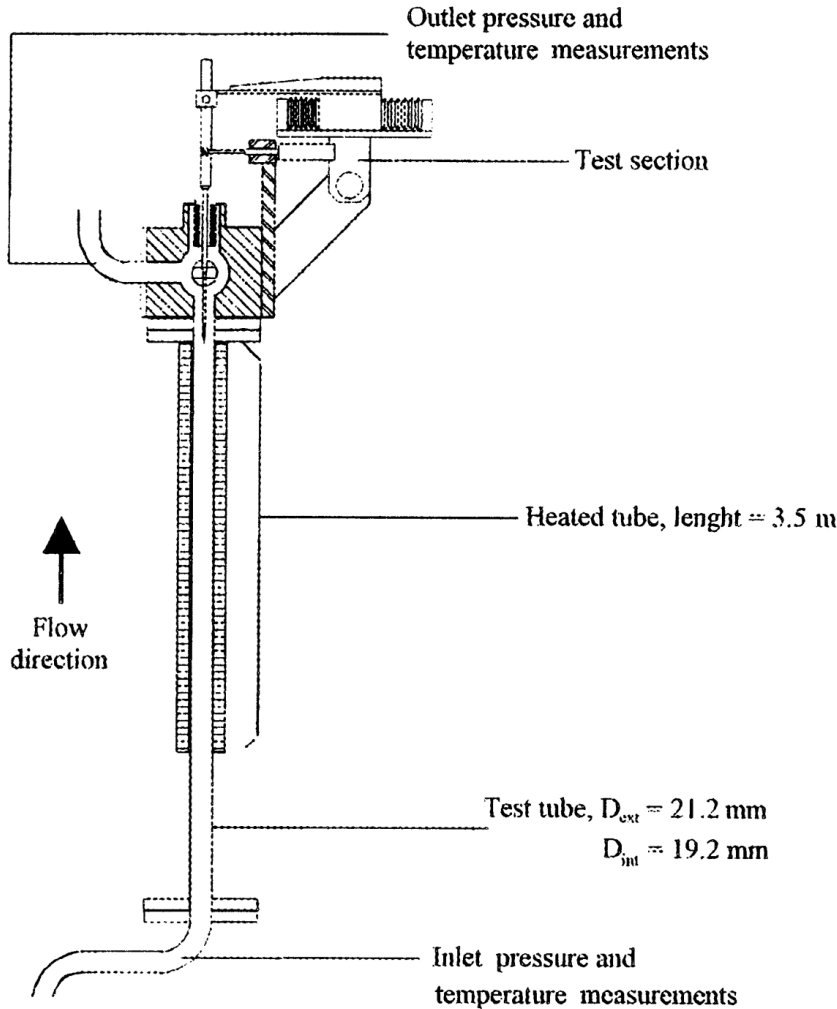


Figure 2.4: Sketch of the DEBORA test section. Adapted from [17].

2.3.2 Measurement Instrumentation

The control parameters are adjusted and measured using pressure, temperature, flow rate and power measurements. They are further detailed in Cubizolles [Cubizolles_1996].

The local measurements are conducted at the end of the heating length using a controllable probe that can cover the whole diameter of the test section with an accuracy of $10\mu\text{m}$. Only one diameter is covered since the chosen geometry induces an axisymmetry.

Three type of measurements have been conducted over different experimental campaigns.

2.3.2.1 Mono-Optical Probe Measurements

Optical probe measurement rely on the difference of optical refractive index between the liquid and vapor phase. Using an optical fiber in which light is emitted towards the probe tip allows to detect the actual phase flowing on the probe.

The resulting signal is called a Phase Indicator Function (PIF) which looks like to a square signal (Figure 2.5) that can be post-processed to identify the average time spent by the probe in each phase and then estimate their volume fraction *e.g.* the void fraction.

If the PIF is measured over a period T , the void fraction α at the measurement point x can be estimated by:

$$\alpha(x) = \nu(x) \bar{t_V} = \frac{1}{T} \sum t_V \quad (2.5)$$

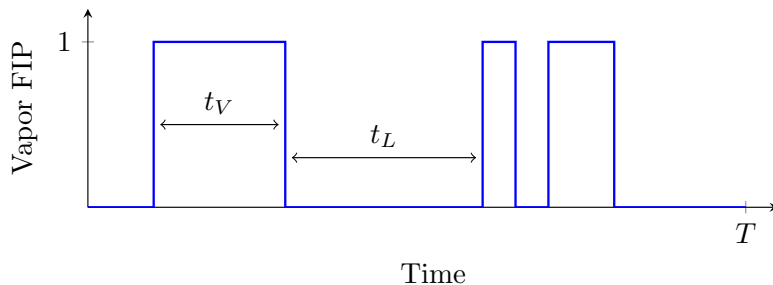


Figure 2.5: Example of Phase Indicator Function signal

where ν is called the interference frequency that represents the number of phase interface detection per second by the probe.

Remark : This measurement technique was performed in the **measurement campaign C2900** where void fraction profiles at the outlet were obtained for various flow conditions.

2.3.2.2 Bi-Optical Probe Measurements

Using the technology of the optical phase detection, adding a second optical probe permits to measure more parameters of the two-phase flow. Indeed, the use of two probes placed close to each other with a small shift in the flow direction (Figure 2.6) allows to estimate the velocity of the interface between the two probes by measuring the time difference between the two PIF.

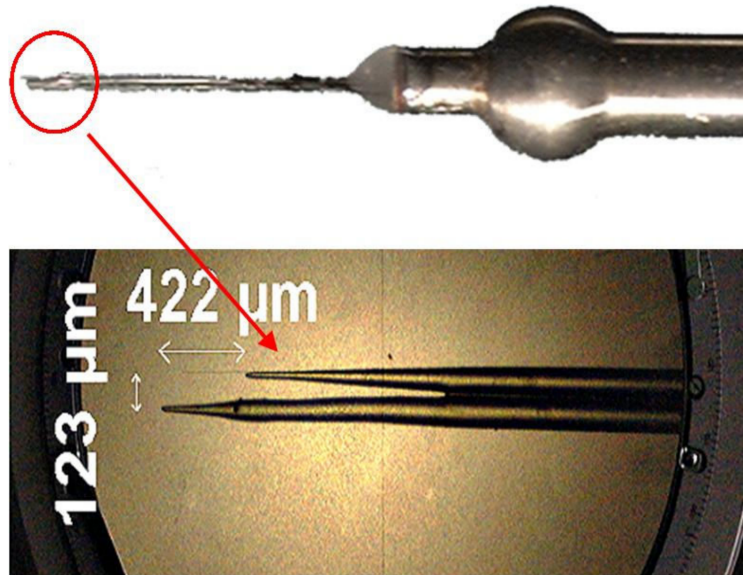


Figure 2.6: Picture of the bi-optical probe with a zoom over the two optical fibers. Reproduced from [gueguen_phd].

Considering the following assumptions:

- The flow is mainly one-directional in aligned with the probes ;
- The vapor phase is composed of spherical inclusions ;
- The velocity gradient and center density gradient are small along a bubble diameter length.

Then we can estimate:

- The vapor axial velocity $U_{V,z}$ that can be supposed equal to the measured interface velocity between the probes ;

- The interfacial area density a_i :

$$a_i = \frac{4\nu}{U_{V,z}} \quad (2.6)$$

- The bubble Sauter diameter:

$$D_V = \frac{6\alpha}{a_i} \quad (2.7)$$

Remark : This measurement technique was performed in the **measurement campaign C3000**.

2.3.2.3 Thermocouples Measurements

Thermal measurements are conducted using chromel-alumel thermocouples. The liquid temperature is measured along the outlet diameter at the end of the heating length. Wall temperature measurements are conducted with 4 thermocouples placed at different heights (1.465 m, 2.465 m, 2.965 m, 3.485 m) on the outside of the tube.

Remark : This measurement technique was performed in the **measurement campaign C800**.

2.4 MEASUREMENTS CAMPAIGNS AND RESULTS

2.4.1 Cases Nomenclature and Test Series

As mentioned before, three different campaigns have been performed:

- Campaign C2900 with solely void fraction measurements using mono-optical probe ;
- Campaign C3000 with void fraction, vapor velocity, bubble Sauter diameter and interfacial area density measurements using bi-optical probe ;
- Campaign C800 with liquid and wall temperature measurements using thermocouples.

Each measurement series is conducted under fixed outlet pressure, liquid mass flux and electrical power. Inlet temperature is then changed to cover different inlet quality. Experimental cases are named in the form **CccGgPppWwwTett** with **cc** the campaign number (29, 30 or 8), **g** the inlet mass velocity (G in $t/m^2/s$), **pp** the outlet pressure (P in bars), **ww** the total heat power applied (Φ_w in kW) and **tt** the inlet temperature ($T_{L,in}$ in K). For instance, the case named C30G2P26W16Te66 has been conducted with $P = 26.2$ bar, $G = 2049 \text{ kg/m}^2/\text{s}$, $\Phi_w = 15.6 \text{ kW} \equiv \phi_w = 73.89 \text{ kW/m}^2$ and $T_{L,in} = 66.59^\circ\text{C}$. If we want to obtain a full description of the two-phase flow from the DEBORA tests, we need to have measurements from campaigns C3000 and C800 (flow topology and thermal) with the same control parameters. Table 2.2 unfortunately shows that only very few test series between C3000 and C800 have common operating conditions, namely:

- Series 8G2P14W16 and 30G2P14W16 ;
- Series 8G2P26W16 and 30G2P26W16.

Other flow conditions have either been covered with thermal measurements or topology measurements but not both.

Remark : Cases from the campaign C2900 would only be relevant for void fraction profiles comparison. Estimations of the bubble diameter can not be achieved except if one assumes a velocity profile as suggested by Cubizolles [**cubizolles_phd**] and re-used by Guéguen [**gueguen_phd**] who supposes:

$$U_{V,z}(r) \approx U_{M,z}(r) = 1.22 \frac{G}{(\rho_M)_2} \left(\frac{R-r}{R} \right)^{1/7} \quad (2.8)$$

where $U_{M,z}$ is the mixture axial velocity, assuming a mechanical equilibrium between the phases.

For further studies, we will mainly focus on the G2P26W16 and G2P14W16 test series. Although we will mainly rely on the results from the C3000 campaign (where vapor velocity was actually measured) for flow topology qualification, we will evaluate the assumption of Eq. 2.8 with the C2900 measurements.

P	G	W16	W17	W23	W24	W25	W27	W29	W30	W31	W33	W34	W36	W38	W39	W40	W42	W44								
14	2	○ ▽ △	△		○																					
	4				○			▽	▽		▽	▽	▽	▽	▽	▽	▽									
	5																									
26	2	○ ▽ △		▽ △		▽	▽ △	▽		▽ △	▽		▽ △	▽	▽	▽ △	▽	▽ △								
	3				○																					
	5	○																								
<table border="1" style="margin-left: auto; margin-right: auto;"> <tr> <td>P</td><td>G</td><td>W12</td><td>W14</td></tr> <tr> <td>30</td><td>1</td><td>▽</td><td>▽</td></tr> </table>																			P	G	W12	W14	30	1	▽	▽
P	G	W12	W14																							
30	1	▽	▽																							

Table 2.2: Test matrix of the DEBORA cases. ○: C800 - ▽: C2900 - △: C3000

2.4.2 Verification of Control Parameters Coherency

For each case, the total heat input Φ_w is given along with the inlet mass flux G , inlet liquid temperature $T_{L,in}$ and outlet quality $x_{eq,out}$. To verify the consistency of those values, we can recalculate the outlet quality:

$$x_{eq,out,calc} = \frac{h_{M,out,calc} - h_{L,sat}}{h_{LV}} \quad (2.9)$$

with $h_{M,out,calc}$ the recalculated outlet mixture enthalpy :

$$h_{M,out,calc} = h_{in} + \frac{\Phi_w}{GS_{in}} = h_{in} + \frac{4\phi_w L_{heat}}{GD_h} \quad (2.10)$$

with h_{in} the inlet enthalpy calculated from the fluid properties using the inlet liquid temperature.

The difference between the given and recalculated outlet quality can also be converted to input power error by recalculating the heat needed to reach the given $x_{eq,out}$:

$$\Phi_{w,calc} = \frac{G\pi R^2}{\underbrace{[x_{eq,out}h_{LV} + h_{L,sat}] - h_{L,in}}_{h_{M,out}}} \quad (2.11)$$

Moreover, for a given set of experiments at the same P , G and Φ_w changing the inlet quality can be associated to moving the measurement diameter along the axial direction following the relationship:

$$x_{eq}(z) = x_{eq,in} + \frac{4\phi_w z}{GD_h h_{LV}} \quad (2.12)$$

Thus, taking the maximum inlet quality case $x_{eq,in,max}$ as a reference ($z = 3.5$ m), we can estimate the corresponding measurement height z_{eq} of each other cases if the inlet quality was $x_{eq,in,max}$.

We calculated the equivalent heights and outlet quality / power input errors for two series of the C3000 campaigns. Results are displayed on Tables 2.3 and 2.4.

As we can see, the given values of outlet quality for the 30G2P14W16 tests are coherent with the one-dimensional enthalpy balance with errors mostly less than 0.1% on the recalculated quality and less than 100 W on the recalculated power input. This naturally leads to an equivalent height very close to 3.5 m for the hottest case.

However, a more significant error is observed on the 30G2P26W16 cases where errors up to 0.75% on the outlet quality and close to 0.4 kW on the power input are found. Those values are significant especially

$T_{L,in}$ [K]	$x_{eq,in,calc}$ [-]	$x_{eq,out,calc}$ [-]	$x_{eq,out}$ [-]	z_{eq} [m]	$x_{eq,out}$ error [-]	Φ_w error [kW]
22.39	-0.317	-0.0821	-0.0832	1.075	0.114 %	-0.078
26.8	-0.28	-0.0422	-0.0431	1.653	0.089 %	-0.061
28.76	-0.263	-0.0267	-0.0273	1.896	0.056 %	-0.038
30.08	-0.252	-0.0152	-0.0157	2.065	0.05 %	-0.034
31.39	-0.241	-0.004	-0.0043	2.234	0.035 %	-0.023
38.95	-0.175	0.0674	0.0681	3.229	-0.072 %	0.049
39.96	-0.166	0.077	0.0776	3.357	-0.063 %	0.042
41.16	-0.155	0.0875	0.0882	3.509	-0.064 %	0.043

Table 2.3: Recalculated control parameters for the 30G2P14W16 cases. ($T_{sat} = 58.07^\circ\text{C}$)

$T_{L,in}$ [K]	$x_{eq,in,calc}$ [-]	$x_{eq,out,calc}$ [-]	$x_{eq,out}$ [-]	z_{eq} [m]	$x_{eq,out}$ error [-]	Φ_w error [kW]
58.57	-0.395	-0.0893	-0.0819	1.792	-0.747 %	0.381
60.54	-0.370	-0.0650	-0.0578	2.072	-0.722 %	0.369
62.54	-0.344	-0.0392	-0.0318	2.369	-0.741 %	0.378
64.6	-0.318	-0.0123	-0.0050	2.674	-0.736 %	0.376
66.59	-0.292	0.0140	0.0213	2.973	-0.728 %	0.371
68.57	-0.266	0.0402	0.0473	3.271	-0.716 %	0.365
70.59	-0.239	0.0670	0.0743	3.583	-0.723 %	0.369

Table 2.4: Recalculated control parameters for the 30G2P26W16 cases. ($T_{sat} = 86.81^\circ\text{C}$)

for cases close to saturation where uncondensed vapor will start to appear in the bulk. Moreover, this results in an equivalent height 8.3 cm longer than the actually 3.5m heated length.

Since the inlet temperature, mass flux and power input are controlled parameters for each test, it is likely that the error may come from the given value of outlet quality $x_{eq,out}$ which is calculated and not imposed.

Note : Similar quality / input power errors were obtained on corresponding C29 and C8 campaigns:

- Negligible errors on for 29G2P14W16 and 8G2P14W16 cases ;
- Roughly 0.7 % outlet quality error and 0.3 to 0.4 kW power error for 29G2P26W16 and 8G2P26W16 cases.

2.4.3 Qualitative Analysis of the Experimental Results

On Figures 2.7, 2.8, 2.9 and 2.10 we respectively plot the experimental measurements of cases 29/30G2P26W16, 8G2P26W16, 29/30G2P14W16 and 8G2P14W16. The colorbar representing the oulet quality of each test is based on the computed value of $x_{eq,out}$ (Eq. 2.9).

2.4.3.1 G2P26W16 cases

Void fraction profiles obtained in for C2900 (single optical probe) and C3000 (bi-optical probe) cases are compared to verify the consistency of the measurements (Figure 2.7a). The two campaigns are in good agreement with each other, displaying a void fraction profile monotonously increasing with the outlet quality. The estimation of the vapor velocity by Eq. 2.8 for the C29 results is acceptable but presents an growing underestimation as the outlet title increases (Figure 2.7b). This results in bubble diameter underestimation close to the wall and consequently interfacial area overestimation.

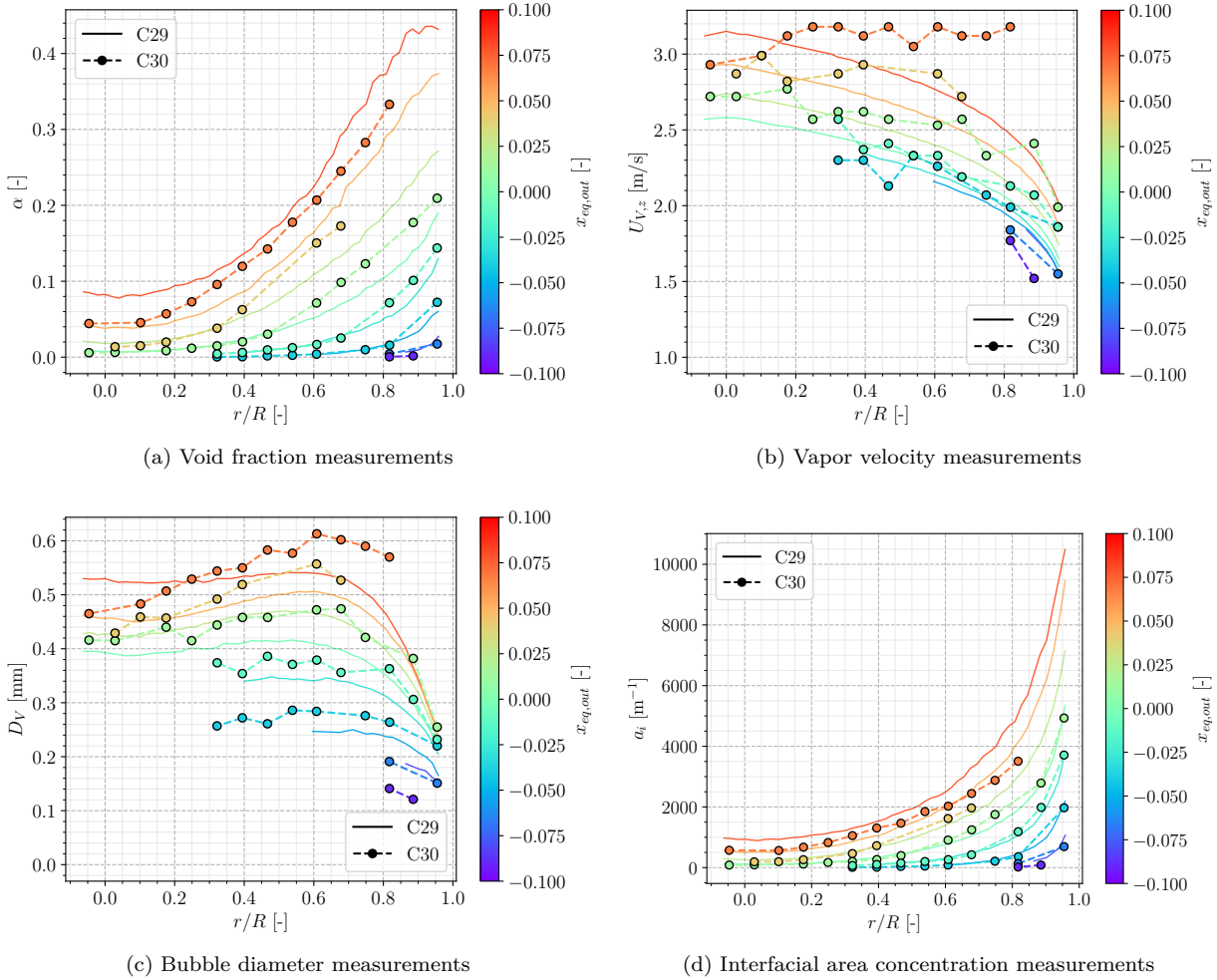


Figure 2.7: 30G2P26W16 and 29G2P26W16 results

We observe that the void fraction naturally increases with the outlet quality and that we reach net vapor generation with $\alpha(R = 0) > 0$ when $x_{eq,out} > 0$. Otherwise, vapor is not detected over the whole measurement section. Each case has its maximum void fraction near the wall with values up to approximately 40% when the outlet quality approaches 0.1.

The bubble diameter displays different behaviors (Figure 2.7c):

- It grows from the wall and reaches a maximum around $r/R \approx 0.6$, indicating bubble coalescence ;
- It stays nearly constant for negative outlet quality cases ;
- It decreases from $r/R = 0.6$ to $r/R = 0$ for saturated cases , indicating either bubble break-up or bulk condensation.

Remark : It seems that bubble diameter very close to the wall do not vary much between different cases, indicating that bubbles leave the wall at a nearly constant diameter over the different explored liquid temperatures ($D_V \approx 0.2$ mm).

Vapor velocity also increases with the outlet quality, with a nearly flat profile reached for saturated cases. The increase in vapor velocity may result of the larger bubble diameters which enhance the effect of buoyancy, acting as an accelerating term increasing the drift velocity.

Remark : Eq. 2.8 fails to predict this flattening of the vapor velocity on C2900 cases, which may indicate a change in the flow structure that can not be detected when assuming liquid-vapor mechanical equilibrium.

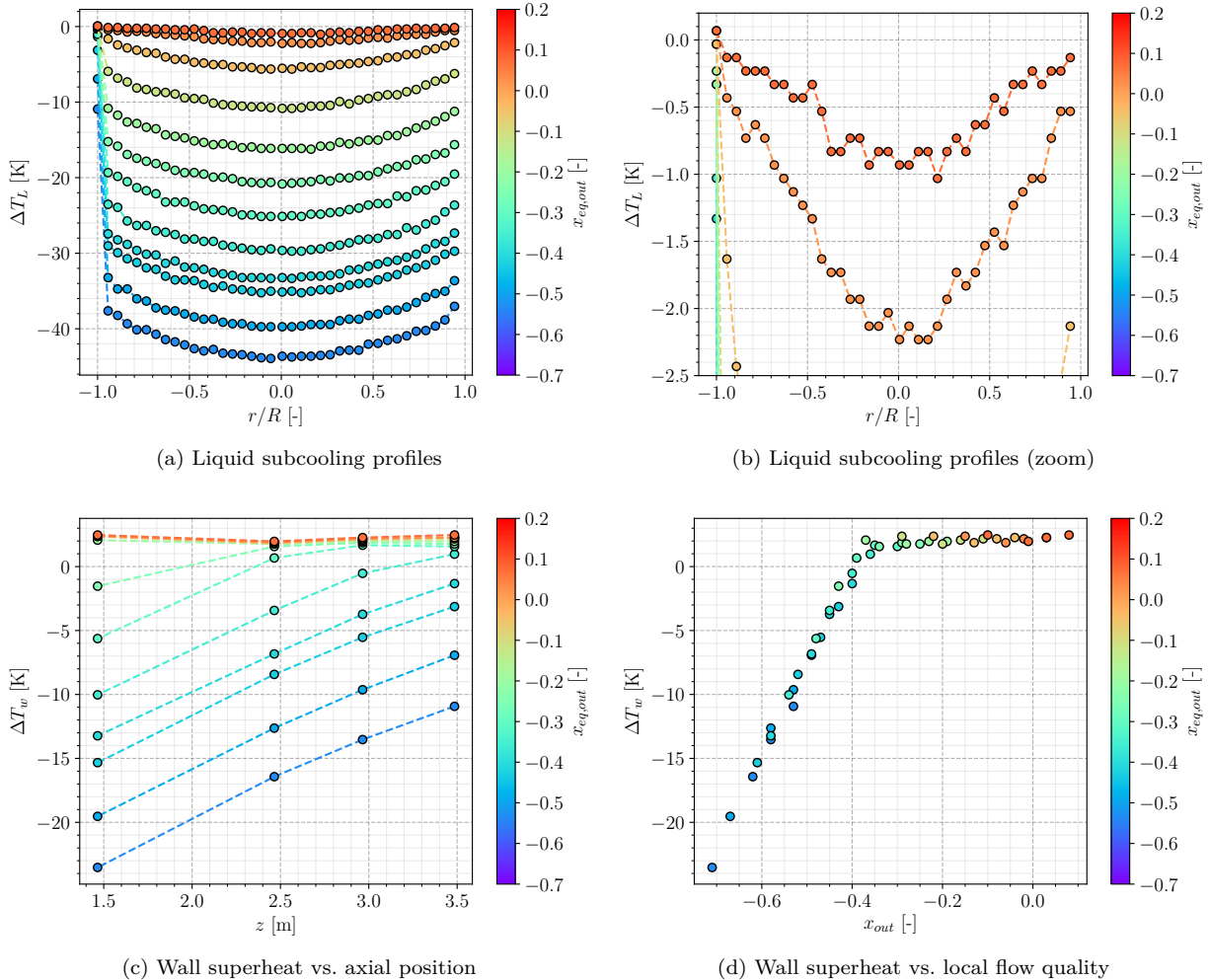


Figure 2.8: 8G2P26W16 results

Regarding the liquid temperature measurements (Figures 2.8a and 2.8b), we see that temperature profiles linearly rise with the inlet quality while presenting an unmodified parabolic shape. The only change appears when reaching significant superheated conditions ($x_{eq,out} \sim 0.1$) where the liquid temperature profile flattens over the test section.

Moreover, we observe that measurements very close to the wall present a very large temperature gradient even for low quality cases (temperature jump of nearly 30 degrees for coldest cases). This jump reduces as flow quality increases and reduces even more for boiling cases, indicating the well-known rise of the global heat transfer coefficient in boiling regime vs. single-phase convection regime.

We can also note that for the hottest case, the liquid becomes superheated near the wall ($\Delta T_L (\pm 1) \approx 0.1^\circ\text{C}$). The bulk is still slightly subcooled with $\Delta T_L (0) = -1^\circ\text{C}$

Remark : The liquid being subcooled in the bulk for superheated cases hints that the decrease in bubble diameter observed in Figure 2.7c for $r/R < 0.6$ may be associated to condensation.

Wall temperature measurements (Figures 2.8c) display linear growth for subcooled cases which is in agreement with traditional liquid convection problems. When reaching boiling, the wall superheat stabilizes at $\Delta T_w \approx 2^\circ\text{C}$. Rearranging the different wall temperature measurements versus the local flow quality (Figure 2.8d) presents a coherent overlapping between cases with different inlet subcooling. This further

validates the transposition of inlet quality into variation into an evolution of the measurement probe's axial position.

2.4.3.2 G2P14W16 cases

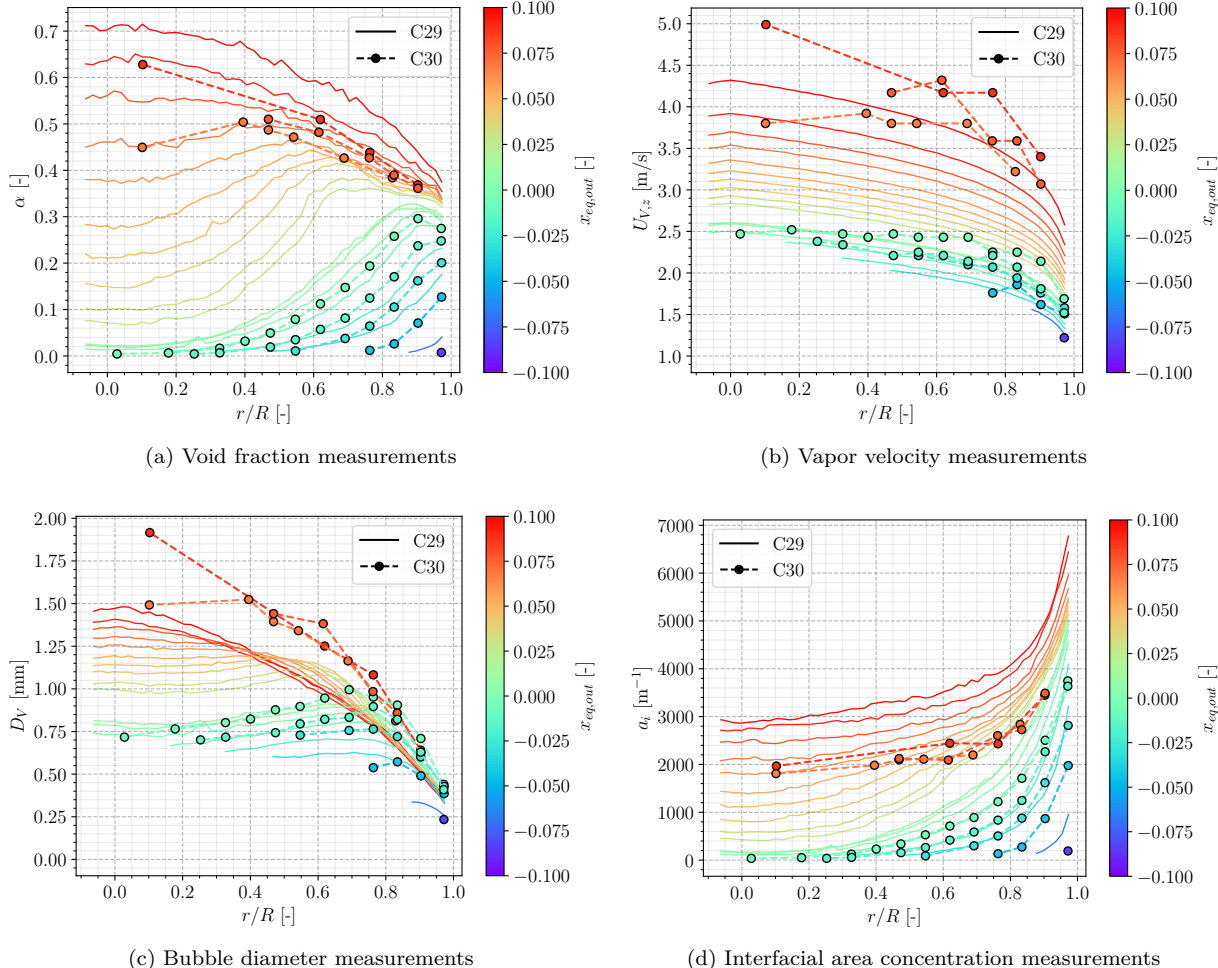


Figure 2.9: 30G2P14W16 and 29G2P14W16 results

Similar to the G2P26W16 cases, we observe the consistency of the void fraction measurements between the C2900 and C300 campaigns (Figure 2.9a). Although the vapor velocity estimation using Eq. 2.8 for C2900 cases also produces acceptable results for subcooled cases, the discrepancy when saturation is reached is even more observed here (Figure 2.9b). The overestimation when $x_{eq,out} > 0$ is larger than for the G2P26W16 cases, with nearly 1 m/s error on hottest cases.

This logically yields larger underestimations of the bubble diameter and associated overestimations of the interfacial area concentration.

The void fraction profiles (Figure 2.9a) present a particular evolution with a moving α peak that shifts from the wall to the bulk as the outlet quality increases. This may indicate a particular bubble dynamics regime inducing transverse bubble migration and accumulation far from the wall. Bulk void fraction can reach values as high as 70% with a flattening profile when $x_{eq,out} \rightarrow 0.1$.

Remark : It seems that saturated cases tend to reach a fixed value of near-wall void fraction between 35% and 40%.

Similar to previous observations, the bubble diameter grows when moving to the bulk, also presenting a peak value around $0.8 > r/R > 0.6$ for subcooled cases (Figure 2.9c). The saturated cases however

present much larger increase in bubble diameter when reaching the bulk flow, with D_V close to 2 mm for the hottest case. This definitely indicates predominant coalescence effects.

Remark : $D_V \approx 2$ mm is observed at a point where $\alpha > 60\%$ which shows that even at such high void fraction values, the flow is still in a bubbly regime with small vapor inclusions ($D_V \approx 0.1D_h$).

The vapor velocity also increases with the outlet quality (Figure 2.9b), but reaches much larger value compared to the G2P26W16 cases. This may be due to the larger bubble size and local void fractions associated to the imposed mass flow rate.

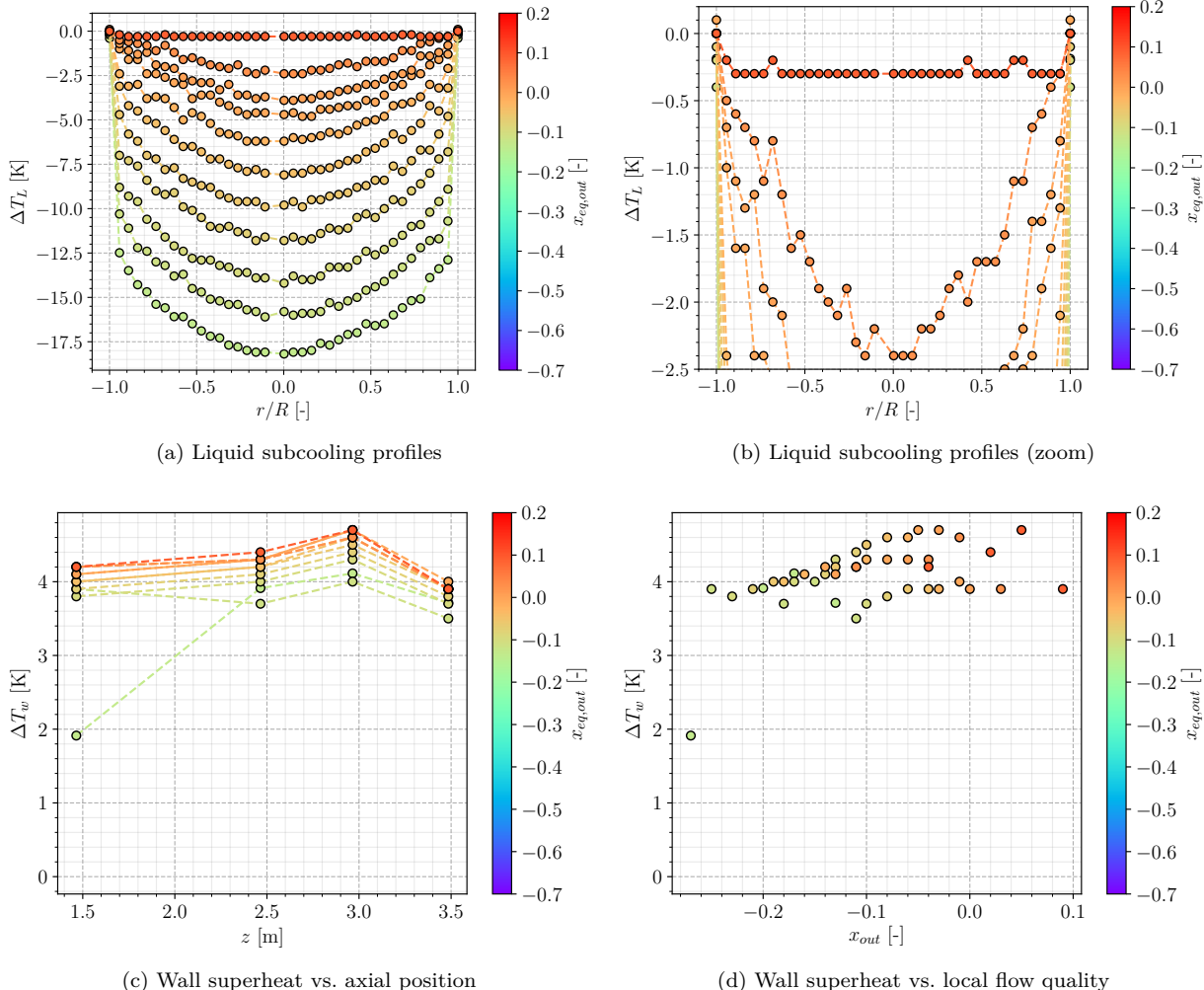


Figure 2.10: 8G2P14W16 results

The liquid temperature profiles (Figure 2.10a) are behaving in a very similar way to the G2P26W16 cases (Figure 2.8a): stable parabolic profile, linear shift with inlet quality and flattening when reaching superheated conditions ($x_{eq,out} \sim 0.1$).

We also have the huge temperature jump when approaching the wall which reduces when reaching boiling regimes. The measurements also detect superheated liquid near the wall for the hottest cases ($\Delta T_L \approx 0.1^\circ$). The case with the greatest outlet quality presents a surprisingly flat liquid temperature profile with measurements being nearly constant ($\Delta T_L = -0.3^\circ\text{C}$) over the whole measurement section.

Remark : Such a constant temperature profile could be interpreted as a limit of the liquid temperature in this regime. Since it corresponds to flow conditions where void fraction is large ($\alpha > 60\%$) and bubbles do not condense (Figure 2.9c), any extra heat input may only contribute to phase change and leave the liquid phase thermally unchanged.

Unfortunately, the 8G2P15W16 campaign did not cover as large quality range as the 8G2P26W16 campaign. We thus do not have access to many single-phase flow wall temperature measurements (Figure 2.10c). Only one point for $x_{eq,out} \approx -0.1$ seem to be in the single-phase convection region. All the other measurements are close to each other and correspond to boiling regimes where we observe a wall superheat stabilization around $\Delta T_w = 4^\circ\text{C}$.

The comparison of wall temperature with local flow quality (Figure 2.10d) is not as interesting as the G2P26W16 cases but still display a welcomed overlapping of the measurements over the different inlet temperatures.

2.5 FURTHER VERIFICATIONS

2.5.1 Reconstruction of the Applied Heat Flux

To further quantify the coherency of the DEBORA database, we want to reconstruct the wall heat flux injected in the flow from the experimental measurements of void fraction, vapor velocity and liquid temperature measurements.

2.5.1.1 Methodology

To do so, we will estimate the total enthalpy change between the inlet and outlet. The inlet liquid enthalpy $h_{L,in}$ is estimated using the inlet temperature and the outlet mixture enthalpy $h_{M,out}$ is computed as:

$$h_{M,out} = x_{m,out} h_{V,sat} + (1 - x_{m,out}) \langle h_{L,out} \rangle_2 \quad (2.13)$$

supposing that the vapor is at saturation temperature and where $x_{m,out}$ is the outlet mass quality.

Using the experimental values of α and $U_{V,z}$, we can compute the outlet mass quality $x_{m,out}$ as:

$$x_{m,out} = \frac{\rho_V \langle \alpha U_{V,z} \rangle_2}{G} \quad (2.14)$$

where:

$$\langle \alpha U_{V,z} \rangle_2 = \frac{1}{\pi R^2} \int_{\vartheta=0}^{2\pi} \int_{r=0}^R \alpha(r) U_{V,z}(r) r dr d\vartheta = \frac{2}{R^2} \int_{r=0}^R \alpha(r) U_{V,z}(r) r dr \quad (2.15)$$

for an axisymmetric profile such as the DEBORA measurements.

From the mass quality we can compute the mixture enthalpy as:

$$h_M = x_m h_{V,sat} + (1 - x_m) \frac{\langle \rho_L (1 - \alpha) U_{L,z} h_L \rangle_2}{\langle \rho_L (1 - \alpha) U_{L,z} \rangle_2} \quad (2.16)$$

Similarly, the average liquid enthalpy at the outlet is estimated as:

$$\langle h_L \rangle_2 = \frac{2}{R^2} \frac{1}{G_L} \int_{r=0}^R \rho_L(r) U_{L,z}(r) h_L(r) r dr \quad (2.17)$$

where h_L is estimated using the local temperature measurements and $U_{L,z}$ is estimated using the drift velocity of Ishii [ishii_drift]:

$$U_{L,z} = U_{V,z} - U_{rel} = U_{V,z} - \sqrt{2} \left(\frac{g \sigma (\rho_L - \rho_V)}{\rho_L^2} \right)^{1/4} (1 - \langle \alpha \rangle_2)^{1.75} \quad (2.18)$$

Then, writing the one-dimensional energy balance of the flow permits to express the actually applied heat flux:

$$G \pi R^2 (h_{M,out} - h_{L,in}) = \Phi_w = \phi_w 2\pi R L_{heat} \Rightarrow \phi_w = \frac{(h_{M,out} - h_{L,in}) GR}{2 L_{heat}} \quad (2.19)$$

which can be compared to the given control parameter for the experiment.

2.5.1.2 Application

To apply the presented reconstruction of the heat flux, we either need:

- A pure single-phase case with an outlet liquid temperature profile (C800 case alone);
- A boiling two-phase case with void fraction and vapor velocity measurements (C3000 case) along with liquid temperature (C800 case).

This means that for boiling cases, we need to "merge" cases from the C3000 and C800 campaign conducted in very close operating conditions (P , G , $T_{L,in}$) and assume that the liquid temperature measurements of the C800 case are actually representative of the liquid temperature in the C3000 case and reciprocally for the void fraction and vapor velocity.

Such a constraint leaves us with very few boiling cases that can accommodate those conditions. They are summed up on Table 2.5.

Case Name	P [bar]	G [kg/m ² /s]	ϕ_w [kW/m ²]	$T_{L,in}$ [°C]	$x_{eq,in}$ [-]	$x_{eq,out}$ [-]
30G2P26W16Te66	26.2	2049.0	73.893	66.59	-0.2919	0.014
8G2P26W16Te66.6	26.2	1982.0	73.9	66.57	-0.2927	0.0237
30G2P26W16Te70	26.19	2051.2	73.893	70.59	-0.2386	0.067
8G2P26W16Te70.3	26.2	1983.0	73.9	70.31	-0.2428	0.0734

Table 2.5: Similar conditions cases between the C3000 and C800 campaigns. Outlet quality calculated with Eq. 2.9.

To actually compute the surface-averaged quantities, we need to interpolate the experimental profiles which is done using the python package `scipy`. Figure 2.11 presents typical interpolation profiles used in this sections.

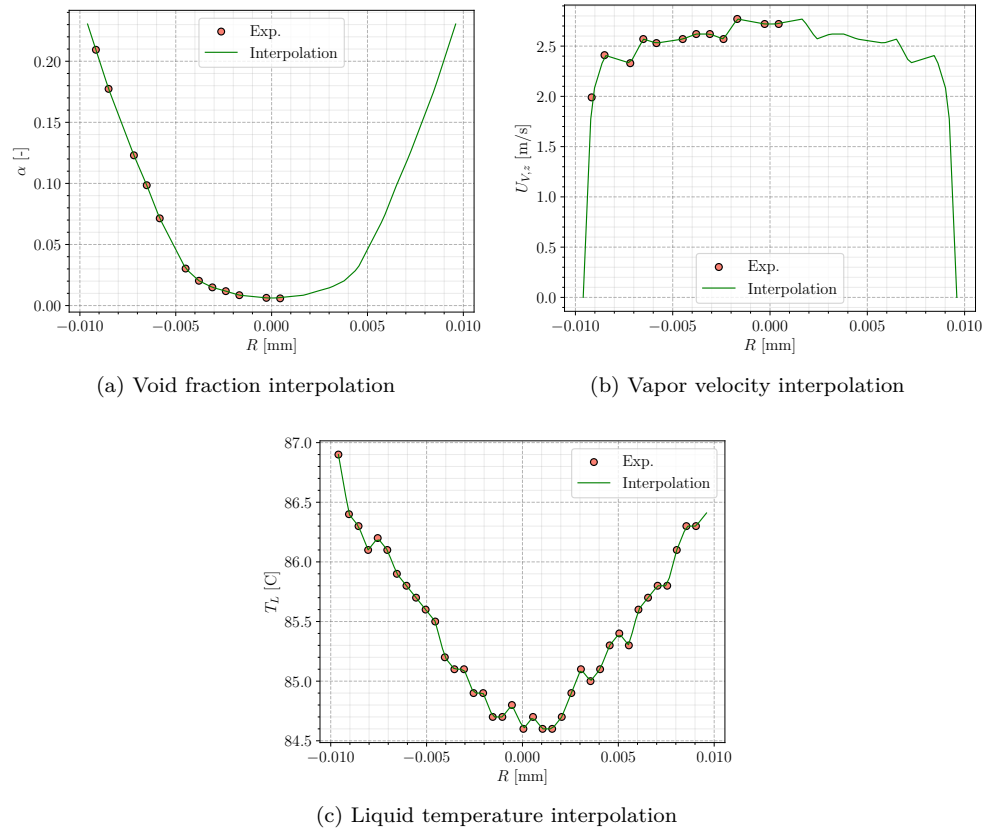


Figure 2.11: Interpolation profiles for cases Te66 (Table 2.5).

The results obtained for the heat flux recalculations are presented on Table 2.6.

Case name	x_m [-]	$\phi_{w,rec}$ [kW/m ²]	$\phi_{w,exp}$ [kW/m ²]	$\Delta\phi_w$ [%]
30G2P26W23Te66.6	0.0193	70.432	73.893	-4.68%
30G2P26W23Te70.6	0.0500%	68.041	73.893	-7.9%

Table 2.6: Heat flux recalculation results

We see that reconstructing the heat flux yields values significantly lower than the experimental values given in the database. This underestimation was also noted in a similar approach conducted by Guéguen [[gueguen_phd](#)] who found discrepancy of a few %.

In our case, these discrepancies can be partially explained by:

- The difference of inlet mass fluxes that are roughly 70 kg/m²/s lower for the C800 cases ;
- The difference of inlet liquid temperature for the Te70 cases with a C800 case 0.3°C lower than the C300 case.

Those small discrepancies lead to outlet qualities (computed with Eq. 2.9 using the given ϕ_w) that differ of approximately 1%. Even though boiling flows near saturation, such as those studied here, are very sensitive to the local quality and flow parameters, this would hardly suffice to explain differences in heat flux as much as 5%.

Remark : Unfortunately, our methodology do not rely on collocated measurements of all the variables of interest since the campaigns were conducted separately. The "correction" values presented in Table 2.6 can not be considered as accurate estimations but still point out that an uncertainty over the heat flux can be considered in further work.

2.5.2 Comparison with One Dimensional Correlations

3

NEPTUNE_CFD SIMULATIONS OF DEBORA CASES

In this work, we present the simulations of the following cases:

- C8G2P26W16Te44.9 and C8G2P26W16Te49.6 (single-phase flow)
- C8G2P26W16Te66.6 and C8G2P26W16Te70.3 (two-phase flow)
- C30G2P26W16Te66.6 and C30G2P26W16Te70.6 (two-phase flow)

The pressure of 26 bar is chosen to match the pressure of the mixing vanes cases (DEBORA-Promoteur, Section 9.1). Mesh sensitivity is performed over two meshes: a large mesh (M1) with 460 356 cells = 338 radial \times 1362 axial cells and a fine mesh (M2) with 3 157 952 cells = 1568 radial \times 2014 axial cells. On Figure 3.1, we present the results regarding liquid temperature at the outlet and wall temperature. The liquid temperature profile seems to be correctly reproduced by the simulations, though we see a slight overestimation close to the wall. Looking closer at boiling cases shows a difference of $\approx 0.5^\circ\text{C}$, which is close to the uncertainty of the measurements [Garnier2001]. Concerning the wall temperature, it appears that it is underestimated before the **Onset of Nucleate Boiling** (ONB) ($T_w < T_{sat}$) and overestimated after the ONB ($\approx +5^\circ\text{C}$). Post-ONB wall temperature is characterized by a stabilization of its value above the saturation temperature (here $T_{w,ONB} - T_{sat} \approx 2^\circ\text{C}$).

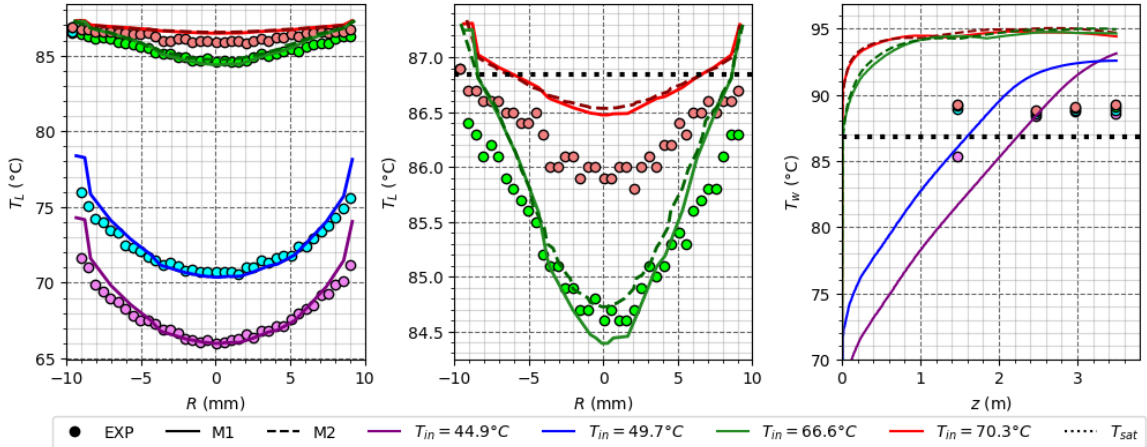


Figure 3.1: NCFD (lines) vs. Exp. (circles) - T_L and T_w - Cases C8G2P26W16Te44.9, Te49.6, Te66.6 and Te70.3
- Simulations using two meshes M1 (coarse) and M2 (fine).

On Figure 3.2, we compare the results of the simulations to the experiments regarding void fraction, bubble Sauter diameter and axial gas velocity. Void fraction profiles are quite correctly reproduced, though we observe a 10% higher peak at the wall for $T_{in} = 66.6^\circ\text{C}$. The order of magnitude of bubble diameter is correct ($\sim 0.1\text{mm}$) and NEPTUNE_CFD manages to detect coalescence (increase of bubble diameter when leaving the wall) and bulk condensation (decrease of bubble diameter when reaching the core of the flow), which is in qualitative agreement with the experiments. Quantitatively speaking, bubble diameter is globally underestimated. Finally, gas velocity profile is reasonably reproduced for $T_{in} = 66.6^\circ\text{C}$, but not for $T_{in} = 70.6^\circ\text{C}$. The latter experimental profile is flatter, which could be explained by a change of flow regime since uncondensed vapor is detected in the bulk.

Finally, the simulations reasonably agree with the experiments. The strongest discrepancies being mostly the wall temperature and bubble diameter. Potential ways of improving those results are investigated in next sub-section.

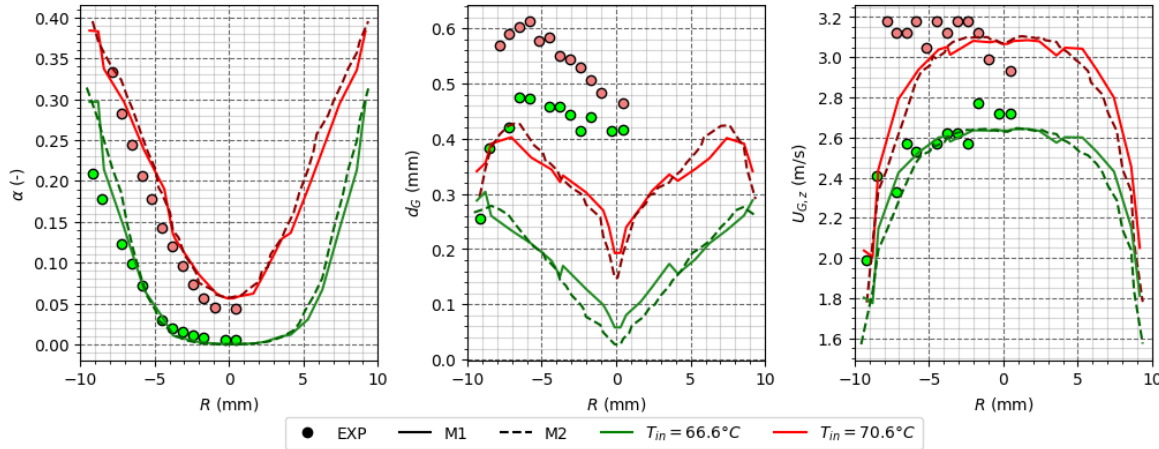


Figure 3.2: NCFD (lines) vs. Exp. (circles) - α , d_G and $U_{G,z}$ - Cases C30G2P26W16Te66.6 and Te70.6 - Simulations using two meshes M1 (coarse) and M2 (fine).

3.0.1 Investigating the nucleation site density modeling N_{sit}

In NEPTUNE_CFD, wall temperature is computed through the Heat Flux Partitioning model, which role is to find the appropriate T_w which balances Equation 8.1. However, some laws used to express parameters such as N_{sit} , f , or d_d are quite old and simple. For instance, the Lemmert & Chawla [Lemmert1977] expression of N_{sit} only depends on the wall superheat (Sub-section 1.5).

A comparison of the Lemmert & Chawla law [Lemmert1977] with the Hibiki & Ishii [Hibiki2003] law for N_{sit} against 4 data sets from the literature is presentend on Figure 3.3. The Hibiki & Ishii correlation depends simultaneously on wall superheat, pressure and contact angle. Experimental measurements of Borishanskii *et al.* [Borishanskii1961], Richenderfer *et al.* [Richenderfer2018], Kossolapov *et al.* [Kossolapov2020] and Zhou *et al.* [Zhou2020] are used to assess the two nucleation site density correlations.

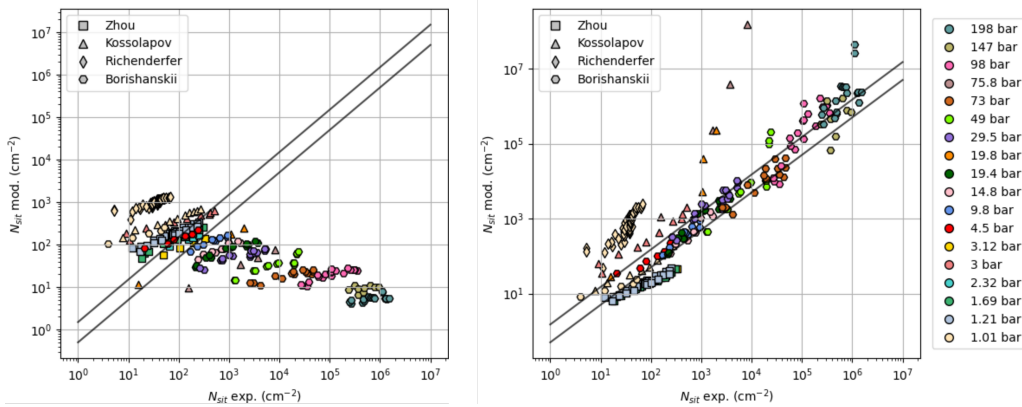


Figure 3.3: N_{sit} correlations of Lemmert & Chawla (left) and Hibiki & Ishii (right) vs. exp. data from literature. Operation pressures are displayed. $\pm 50\%$ error bars are drawn in black.

Figure 3.3 clearly shows that the Lemmert & Chawla law lack of pressure dependence fails to reproduce high pressure measurements contrary to the Hibiki & Ishii one. Even though Hibiki & Ishii correlation shows significant discrepancies with measurements of Kossolapov *et al.* and Richenderfer *et al.*, its prediction capability is greater in average than Lemmert & Chawla correlation.

To assess the influence of nucleation site density law on NEPTUNE_CFD computations, we compare results obtained with both correlations on Figure 3.4, which shows a remarkable impact of the modification of N_{sit} correlation. Using Hibiki & Ishii correlation reduces the error on T_w by approximately 2°C while α and T_L remain unchanged. This implies that the same heat flux partitioning is found with the two models, but that the pressure dependence of Hibiki & Ishii law helped to balance Equation 8.1 using a lower T_w , thus closer to experimental measurements.

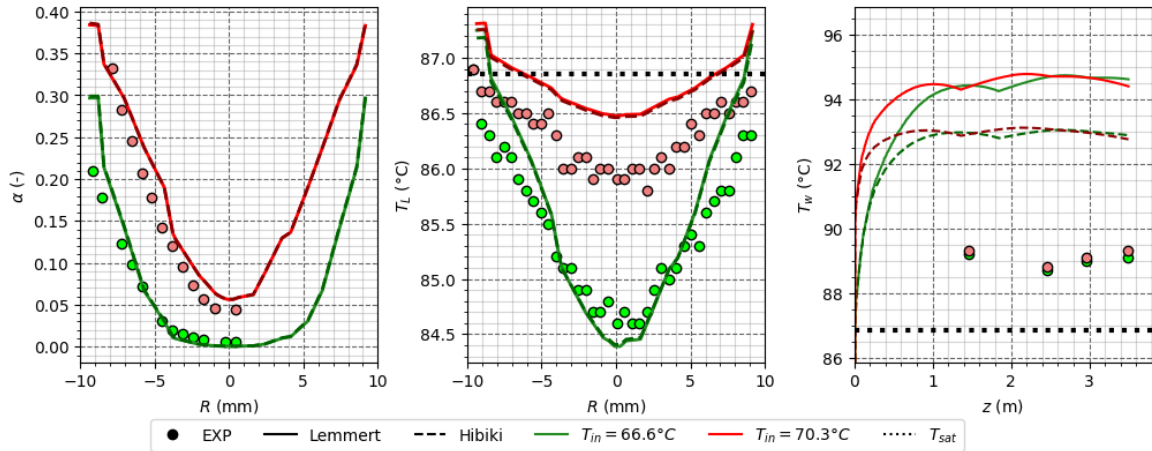


Figure 3.4: NCFD results for α , T_L and T_w using Lemmert & Chawla and Hibiki & Ishii correlation. Cases 8G2P26W23Te66.6 and Te70.3, 30G2P26W23Te66.6 and 70.6.

Such a result indicates that the HFP model could be improved through a systematic analysis of each parameter's impact and modeling (bubble departure diameter, detachment frequency, etc.). Assembling a more recent and consistent model could provide better results regarding wall temperature prediction. Models such as the one developed by Kommajosyula [Kommajosyula2020] could be interesting to apply for high-pressure flows.

Now that simple tube boiling flow has been assessed through the presented results, next section will focus on the simulation of boiling flow in a tube equipped with a mixing device.

Part III

DEVELOPMENT OF A NEW WALL HEAT FLUX PARTITIONING MODEL

4

INTRODUCTION

4.1 FIRST APPROACHES : CORRELATIONS

5

EXISTING HEAT FLUX PARTITIONING MODELS

5.1 KURUL & PODOWSKI (1990)

In their original work published in 1990, Kurul & Podowski [**kurul_1990**] proposed a complete closure for the wall heat flux partitioning. They considered the applied heat flux to be divided between three mechanisms:

- A liquid single-phase heat flux $\phi_{c,L}$;
- A boiling heat flux ϕ_e ;
- A quenching heat flux ϕ_q induced by bubbles leaving the surface.

The total wall heat flux being :

$$\phi_w = \phi_{c,L} + \phi_e + \phi_q \quad (5.1)$$

The convective heat flux is expressed as :

$$\phi_{c,l} = A_{c,L} \rho_L c_{p,L} U_{L,\delta} \text{St}_{L,\delta} (T_w - T_{L,\delta}) \quad (5.2)$$

with δ a location in the buffer layer.

Assuming bubbles are spherical and leave the surface at diameter D_{lo} , they write:

$$\phi_e = \frac{1}{6} \pi D_{lo}^3 \rho_V h_{LV} f N_{sit} \quad (5.3)$$

$$(5.4)$$

The quenching heat flux occurring over the wait time t_w between two nucleated bubbles is computed as:

$$\phi_q = t_w f A_q \frac{2\lambda_L (T_w - T_{L,\delta})}{\sqrt{\pi \eta_L t_w}} \quad (5.5)$$

This expression corresponds to the average heat flux for semi-infinite conduction over a time t_w , as expressed by Del Valle and Kenning [**DelValle**].

They also estimate the portion of the surface affected by the bubbles as:

$$A_q = \min(1 ; F_A \pi R_{lo}^2 N_{sit}) = 1 - A_{c,L} \quad (5.6)$$

where $F_A = 4$ accounts for the bubble influence area when leaving the surface.

Needed closure relationships : N_{sit} , f , t_w , D_{lo}

5.2 BASU (2000)

In 2005, Basu *et al.* [**Basu2005**, **Basu2005a**] proposed a new HFP model together with a series of experiments to further study the different needed closure relationships. This model was meant to account for finer descriptions of the multiple phenomena at stake in subcooled flow boiling. In particular, they account for bubble sliding and merging and thus distinguish bubble departure diameter D_d (leaving the nucleation site) and lift-off diameter D_{lo} (leaving the wall).

Their approach consist of separating the boiling flow in three regions (Figure 5.1):

- Pre-ONB zone, where only liquid forced convection occurs, yielding:

$$\phi_w = h_{c,L} (T_w - T_L) \quad (5.7)$$

- Zone between the ONB and the OSV, prior to observing a net amount of vapor with bubble lifting off the surface. The heat flux is then still totally transferred to the liquid, but the equivalent convective heat transfer coefficient is supposed enhanced by 30% due to the presence of bubbles on the wall:

$$\phi_w = \overline{h_{c,L}} (T_w - T_L) \approx 1.3 h_{c,L} (T_w - T_L) \quad (5.8)$$

Basu *et al.* define the ONB as:

$$T_{w,ONB} = T_{sat} + \frac{4\sigma T_{sat}}{D_c \rho_V h_{LV}} \quad (5.9)$$

$$D_c = \sqrt{\frac{8\sigma T_{sat} \lambda_L}{\rho_V h_{LV} \phi_w}} (1 - \exp(-\theta^3 - 0.5\theta)) \quad (5.10)$$

- Post-OSV zone, where bubbles now leave the surface towards the bulk flow. This is where the other parts of the HFP appear *i.e.* the boiling and quenching fluxes. The beginning of OSV is defined by Basu *et al.* as:

$$T_{L,OSV} = T_{sat} - 0.7 \exp \left(-0.065 \frac{D_d h_{c,L}}{\lambda_L} \right) \frac{\phi_w}{h_{c,L}} \quad (5.11)$$

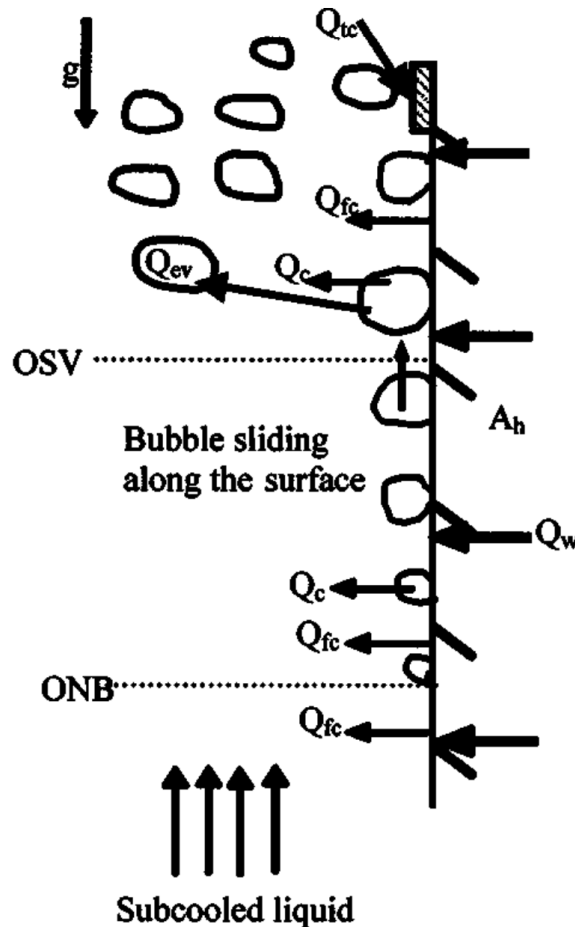


Figure 5.1: Sketch of the heat transfers zones considered by Basu *et al.*. (Adapted from [Basu2005])

The hypothesis of Basu *et al.* is that the heat flux is first transferred to the superheated liquid close to the wall (by convection and transient quenching), part of which contributing to the evaporation through

the liquid-vapor interface. The remaining heat is transferred to the bulk liquid (ϕ_L) either from the superheated liquid layer or bubble condensation. The whole heat transfer mechanism can thus be written as:

$$\phi_w = \phi_{c,L} + \phi_q = \phi_e + \phi_L \quad (5.12)$$

In order to estimate the quenching heat flux associated to bubble sliding and lift-off, Basu *et al.* consider two cases:

- 1) Bubble sliding from departure ($D = D_d$) to lift-off ($D = D_{lo}$) ;
- 2) Bubble coalescence with neighboring sites before departure.

Those two cases are distinguished using the average distance between nucleation sites s , which they suppose equal to $1/\sqrt{N_{sit}}$.

5.2.1 Case 1 : Bubble sliding, $D_d < s$

In this situation, the bubble will grow up to its departure diameter D_d and slide over a length $l_{sl,0}$ before lifting-off. If $l_{sl,0} < s$, the bubble will slide up to its lift-off diameter D_l and leave the wall without colliding with other bubbles. On the contrary, if $l_{sl,0} \geq s$ the sliding bubble will merge with bubbles growing on their nucleation site, inducing a sudden growth of the bubble diameter that can exceed D_{lo} and thus lift-off after sliding over a reduced length $l_{sl} < l_{sl,0}$. Those assumptions are summarized on Figure 5.2.

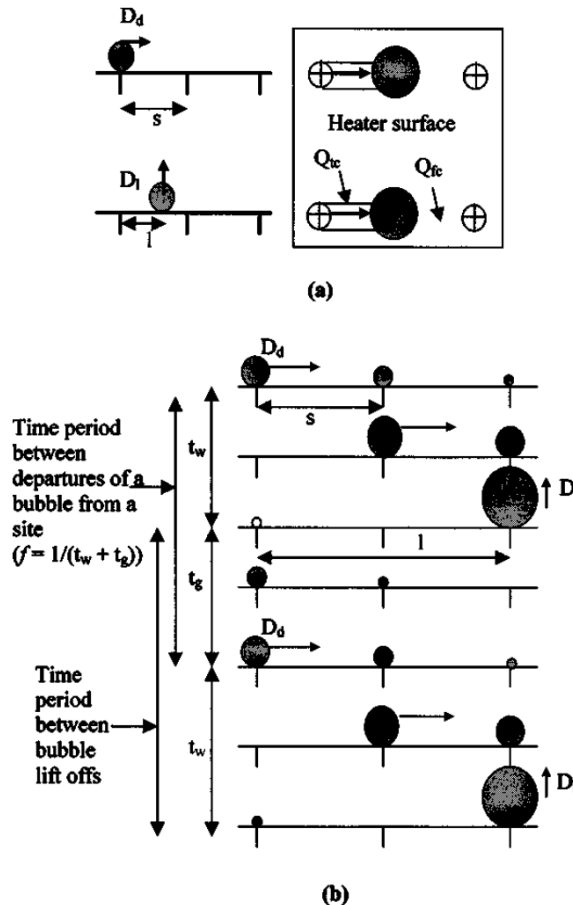


Figure 5.2: Sliding bubble behavior considered by Basu *et al.* (Adapted from [Basu2005])

If bubble coalescence occurs, the number of bubbles lifting-off the surface is lower than the actual number of nucleating sites. Basu *et al.* thus define a reduction factor:

$$R_f = \begin{cases} \frac{s}{l_{sl}} = \frac{1}{l\sqrt{N_{sit}}} & \text{if } l_{sl,0} \geq s \\ 1 & \text{if } l_{sl,0} < s \end{cases} \quad (5.13)$$

Regarding bubble sizes, they suppose that bubbles coalesced by a sliding bubble while growing have a diameter D_d *i.e.* they were close to departure (in reality, the coalesced bubble would have a diameter $D < D_d$). This results in a bubble of diameter $D = (D_{sl}^3 + D_d^3)^{1/3}$ which will lift-off if $D > D_{lo}$. Consequently, a sliding bubble can merge with numerous bubbles before lifting off. Noting N_{merg} the number of coalesced bubble and D_N the resulting bubble diameter, the sliding distance is:

$$l_{sl} = N_{merg}s + l_{D_N \rightarrow D_{lo}} \quad (5.14)$$

where $l_{D_N \rightarrow D_{lo}}$ is the remaining distance to slide if $D_N < D_{lo}$, being 0 if $D_N > D_{lo}$.

The surface swiped by the sliding bubble is then expressed as $A_{sl} = C\bar{D}l_{sl}$ with \bar{D} the average bubble diameter during sliding and C the ration between the bubble diameter and its foot, expressed correlating measurements from Maity [Maity2000] as :

$$C = 1 - \exp(2 - \theta^{0.6}) \quad (5.15)$$

After observing in their experiments that $D_d \approx 0.5D_{lo}$, Basu *et al.* choose:

$$\bar{D} = \frac{D_{lo} + D_d}{2} \approx 0.75D_{lo} \quad (5.16)$$

Noting $t^* = \left(\frac{\lambda_L}{h_{c,L}}\right)^2 \frac{1}{\pi\eta_L}$ the time at which transient conduction heat transfer becomes equal to forced liquid convection, the quenching heat flux is expressed as:

$$\phi_q = \frac{1}{t_w + t_g} \int_0^T \frac{\lambda_L}{\sqrt{\pi\eta_L t}} (T_w - T_L) A_{sl} R_f N_{sit} dt \quad (5.17)$$

where $T = t^*$ if $t^* < t_w + t_g$ (forced convection dominates at some point during a nucleation cycle) or $T = t_w + t_g$ if $t^* \geq t_w + t_g$ (transient conduction dominates over the whole nucleation cycle).

The liquid convective heat transfer is then:

$$\phi_{c,L} = \overline{h_{c,L}} (T_w - T_L) A_{c,L} + \overline{h_{c,L}} (T_w - T_L) A_{sl} R_f N_{sit} \left(1 - \min\left(1 ; \frac{t^*}{t_w + t_g}\right)\right) \quad (5.18)$$

with $A_{c,L} = 1 - A_{sl} R_f N_{sit}$.

And the boiling heat flux:

$$\phi_e = \rho_V h_{LV} \frac{\pi}{6} D_{lo}^3 R_f N_{sit} \frac{1}{t_w + t_g} \quad (5.19)$$

5.2.2 Case 2 : Bubble coalescence without sliding, $D_d \geq s$

Under higher wall superheats, the subsequent rise in the nucleation site density N_{sit} can lead to boiling regimes where bubbles coalesce with each other at early stages of their lifetime *i.e.* while still attached to their nucleation site. This situation is accounted for by Basu *et al.* in the case when $D_d \geq s$ by considering immediate lift-off of coalesced bubble at radius $D > D_{lo}$. In this case, the total number of bubbles leaving the surface is lower than N_{sit} and is thus reduced using:

$$R_f = \frac{s^3}{D_{lo}^3} \quad (5.20)$$

Under this massive coalescing regime, the entire surface will experience quenching due to bubble lift-off all over the heater. Depending on the values of t^* , we have:

$$\phi_q = \begin{cases} \frac{1}{t_w + t_g} \int_0^{t^*} \frac{\lambda_L}{\sqrt{\pi \eta_L t}} (T_w - T_L) dt & \text{if } t^* < t_w \\ \frac{1}{t_w + t_g} \left[\int_0^{t_w} \frac{\lambda_L}{\sqrt{\pi \eta_L t}} (T_w - T_L) dt + \int_0^T \frac{\lambda_L}{\sqrt{\pi \eta_L t}} (T_w - T_L) [1 - S_b N_{sit}] dt \right] & \text{if } t^* \geq t_w \end{cases} \quad (5.21)$$

$$\phi_{c,L} = \begin{cases} \overline{h_{c,L}} (T_w - T_L) \frac{t_w - t^*}{t_w + t_g} + \overline{h_{c,L}} (T_w - T_L) [1 - A_b N_{sit}] \frac{t_g}{t_w + t_g} & \text{if } t^* < t_w \\ \overline{h_{c,L}} (T_w - T_L) [1 - A_b N_{sit}] \frac{t_w + t_g - t^*}{t_w + t_g} & \text{if } t^* \geq t_w \end{cases} \quad (5.22)$$

with $A_b = \frac{\pi (Cs) 2}{4}$.

And the boiling heat flux still expressed as Eq. 5.19.

Needed closure relationships : N_{sit} , t_w , t_g , D_d , D_{lo} , $l_{sl,0}$, $h_{c,L}$.

5.3 GILMAN (2017)

A more recent HFP model dedicated to CFD simulations has been proposed by Gilman & Baglietto in 2017 [gilman2017]. Among the different advances proposed in their work, we can mention :

- A probabilistic law to account for static interaction between nucleation sites ;
- A force-balance approach to compute the bubble departure and lift-off diameters ;
- A generic law for the enhanced forced convection coefficient accounting for bubble presence ;
- The presence of a modified quenching term accounting for local wall superheat beneath a bubble dry spot.

The total heat flux is partitioned between the liquid forced convection $\phi_{c,L}$, the solid quenching $\phi_{q,s}$, the quenching due to bubble sliding $\phi_{q,sl}$ and the evaporation flux ϕ_e . Yielding:

$$\phi_w = \phi_{c,L} + \phi_{q,s} + \phi_{q,sl} + \phi_e \quad (5.23)$$

The convective term is computed in a way similar to Basu *et al.* [Basu2005] in Eq. 5.18:

$$\phi_{c,L} = \phi_{c1,L} + \phi_{c2,L} \quad (5.24)$$

$$= h_{c,L} (1 - A_{sl} N_{sit,a}^*) (T_w - T_L) + \overline{h_{c,L}} A_{sl} N_{sit,a}^* \left(1 - \frac{t^*}{t_w + t_g} \right) (T_w - T_L) \quad (5.25)$$

where $N_{sit,a}^*$ is the active nucleation site density that will generate sliding bubbles, that can differ from the empirical value of available sites N_{sit} usually computed by a correlation.

The active nucleation site density is actually smaller than N_{sit} since Gilman considers an static interaction between the available sites *i.e.* the fact that a bubble laying on a site may be blocking nucleation from sites laying beneath its foot. Following a Complete Spatial Randomness (CSR) approach, they express the probability to find a site under a growing bubble of radius R_d as:

$$\mathcal{P} = 1 - e^{-N_b \pi R_d^2} \quad (5.26)$$

where $N_b = \frac{t_g}{t_w + t_g} N_{sit}$ is the density of bubbles covering the heater.

The number of active sites is then computed as:

$$N_{sit,a} = (1 - \mathcal{P}) N_{sit} \quad (5.27)$$

$$= \exp \left(-\frac{t_g}{t_w + t_g} N_{sit} \pi R_d^2 \right) N_{sit} \quad (5.28)$$

This value is then reduced by Gilman to obtain $N_{sit,a}^*$ using a reduction factor representing sliding bubble coalescence (similar to Basu in Eq. 5.13):

$$N_{sit,a}^* = R_f N_{sit,a} = \frac{s}{l_{sl,0} + s} N_{sit,a} \quad (5.29)$$

The sliding quenching term is also computed in a similar way to Basu as:

$$\phi_{q,sl} = \frac{2\lambda_L (T_w - T_L)}{\sqrt{\pi\eta_L t^*}} A_{sl} N_{sit,a}^* \quad (5.30)$$

$$A_{sl} = \overline{D} l_{sl} = \frac{D_d + D_{lo}}{2} (N_{merg}s + l_{D_N \rightarrow D_{lo}}) \quad (5.31)$$

Regarding the boiling heat flux, Gilman splits it in two contributions respectively associated with the inception of nucleation and liquid microlayer evaporation :

$$\phi_e = \phi_{e,init} + \phi_{e,ML} \quad (5.32)$$

$$= \frac{4}{3}\pi R_d^3 \rho_V h_{LV} \frac{1}{t_w + t_g} N_{sit,a} + V_{ML} \rho_L h_{LV} \frac{1}{t_w + t_g} N_{sit,a} \quad (5.33)$$

$$\text{with } V_{ML} = \frac{2}{3}\pi \left(\frac{R_d}{2}\right)^3 \delta_{max} \quad (5.34)$$

where $\delta_{max} = 2 \mu\text{m}$ based on experiments from Gerardi [Gerardi].

Finally, the solid quenching term is written as:

$$\phi_{q,s} = \rho_w c_{p,w} V_q \delta T_q \frac{1}{t_g + t_w} N_{sit,a} \quad (5.35)$$

$$V_q = \frac{2}{3}\pi r_w^2 \quad (5.36)$$

with $\Delta T_q = 2 K$ as suggested by Gerardi *et al.* [Gerardi_eta].

Needed closure relationships : N_{sit} , t_w , t_g , D_d , D_{lo} , $l_{sl,0}$, $h_{c,L}$, $\overline{h_{c,L}}$.

5.4 ZHOU (2020)

The last HFP model we will look through in this Chapter was proposed by Zhou *et al.* [zhou]. It is one of the most recent available in the literature and was built along with associated experiments for validation. In particular they compute separate heat flux contributions for static (*st*) or sliding bubbles (*sl*), yielding a total heat flux:

$$\phi_w = \phi_{c,L} + (\phi_{e,st} + \phi_{e,sl}) + (\phi_{e,sl} + \phi_{q,sl}) \quad (5.37)$$

An interesting aspect of Zhou *et al.* work is the presence of a condensation term in the evaporation heat fluxes, written as:

$$\phi_{e,st} = \rho_V h_{LV} \frac{4}{3}\pi R_d^3 N_{sit,a} f + h_{cond} (T_{sat} - T_L) A_{cond} N_{sit,a} f (t_g - t_s) \quad (5.38)$$

$$\phi_{e,sl} = \frac{\pi}{6} \rho_V h_{LV} (D_{lo}^3 - D_d^3) f N_{sit}^* + h_{cond} (T_{sat} - T_L) A_{cond} N_{sit}^* t_{sl} f \quad (5.39)$$

$$A_{cond} = \pi D_d \max(R_d (1 + \cos(\theta)) - y_{sat}; 0) \quad (5.40)$$

where y_{sat} is the wall distance where the liquid is at saturation temperature, t_s the moment when $D_b = y_{sat}$ and N_{sit}^* the number of sliding bubbles.

The condensation heat transfer coefficient is computed using the correlation from Ranz & Marshall:

$$h_{cond} = \frac{\lambda_L}{D_d} (2 + 0.6 \text{Re}_b^{0.5}) \text{Pr}_L^{0.3} \quad (5.41)$$

Following similar approaches to HFP models from Basu or Gilman, the quenching heat flux for static bubbles is expressed as:

$$\phi_{q,st} = \begin{cases} t_w f \frac{2\lambda_L (T_w - T_L)}{\sqrt{\pi\eta_L t_w}} A_b N_{sit} & \text{if } t^* \geq t_w \\ t^* f \frac{2\lambda_L (T_w - T_L)}{\sqrt{\pi\eta_L t^*}} A_b N_{sit} + h_{c,L} (T_w - T_L) A_b N_{sit}^* f(t_w - t^*) & \text{if } t^* < t_w \end{cases} \quad (5.42)$$

with $A_b = \underbrace{K_b}_{=2} \pi R_d^2$.

And for the sliding bubbles:

$$\phi_{q,sl} = \begin{cases} \frac{2\lambda_L (T_w - T_L)}{\sqrt{\pi\eta_L (t_g + t_w)}} A_{sl} N_{sit}^* & \text{if } t^* \geq t_g + t_w \\ t^* f \frac{2\lambda_L (T_w - T_L)}{\sqrt{\pi\eta_L t^*}} A_{sl} N_{sit}^* + h_{c,L} (T_w - T_L) A_{sl} N_{sit}^* f(t_g + t_w - t^*) & \text{if } t^* < t_w \end{cases} \quad (5.43)$$

with $A_{sl} = \underbrace{K_{sl}}_{=2} \frac{D_d + D_{lo}}{2} l_{sl}$ and $l_{sl} = \min \left(l_{sl,0} ; \frac{1}{\sqrt{t_g f N_{sit}}} \right)$.

Finally, the forced liquid convective heat flux is computed:

$$\phi_{c,L} = h_{c,L} (1 - A_b N_{sit} - A_{sl} N_{sit}^*) (T_w - T_L) \quad (5.44)$$

Needed closure relationships : N_{sit} , t_w , t_g , D_d , D_{lo} , $l_{sl,0}$, $h_{c,L}$.

5.5 CLOSURE LAWS FOR REMAINING PARAMETERS

In each of the 4 presented HFP models, there is a number of parameters that still need to be computed in order for the model to be fully expressed. Those parameters are often the nucleation site density, bubble diameters, etc. To do so, closure relationships are used and differ from one model to another. Here we want to sum up the different choices of the authors to point the variety of possibilities that exist.

5.5.1 Nucleation Site Density : N_{sit}

The value of the nucleation site density is a very sensitive parameter that controls the intensity of the boiling heat transfer. Unfortunately, its value can vary over a very large range of value depending on the operating conditions and heater material and is thus expressed using experimental correlations.

In their work, Kurul & Podowski used the law of Lemmert and Chawla [**Lemmert**]:

$$N_{sit} = [210 (T_w - T_{sat})]^{1.8} \quad (5.45)$$

Later, Basu [**Basu**] correlated her own experimental results to obtain:

$$N_{sit} = \begin{cases} 0.34 [1 - \cos(\theta)] \Delta T_w^2 & \text{if } \Delta T_{w,ONB} < \Delta T_w < 15 K \\ 3.4 \times 10^{-5} [1 - \cos(\theta)] \Delta T_w^{5.3} & \text{if } \Delta T_w > 15 K \end{cases} \quad (5.46)$$

Finally, Zhou *et al.* followed a approach similar to Basu *et al.* by correlating their own experimental data:

$$N_{sit} = N_0 (1 - \cos(\theta)) [\exp(f(P) \Delta T_w) - 1] f(P) = 0.218 \ln \left(\frac{P}{P_0} \right) + 0.1907 \quad (5.47)$$

with $N_0 = 55\ 395.26\ m^{-2}$ and $P_0 = 1.01\ bar$.

5.5.2 Bubble Departure Frequency f , Growth Time t_g and Wait Time t_w

Historically, Kurul & Podowski modeled the BDF according to Cole [Cole] which derived an expression using photographic observations of bubble nucleation, further verified by Ceumern & Lindenstjerna for pool boiling of water at pressures up to 8 bar. :

$$f = \sqrt{\frac{4}{3} \frac{g(\rho_L - \rho_V)}{\rho_L D_d}} \quad (5.48)$$

Then, assuming that the growth time of the bubble before departure is small compared to the wait time before a new bubble nucleates ($t_{g,d} \ll t_w$) gives :

$$t_w \approx \frac{1}{f} \quad (5.49)$$

Although the assumption of a negligible growth time is true in different cases, notably when bubble departure diameter is small *i.e.* they leave their nucleation site nearly instantly, this is not generally true and the value of the ratio $\frac{t_{g,d}}{t_w}$ can vary by decades depending on the thermal-hydraulics conditions.

Thus, later models considered separate modeling of the growth and wait time in order to compute the BDF as :

$$f = \frac{1}{t_{g,d} + t_w} \quad (5.50)$$

In this scope, Basu *et al.* [Basu] correlated their own experimental results to obtain :

$$t_g = \frac{D_d^2}{45 e^{-0.02} \text{Ja}_L \eta L \text{Ja}_w} \quad (5.51)$$

$$t_w = 139.1 \Delta T_w^{-4.1} \quad (5.52)$$

Gilman & Baglietto [Gilman] chose use the growth law of Zuber [Zuber1961] and the total BDF of Cole (Eq. 5.48) to close the relation 5.50.

$$t_{g,d} = \frac{\pi R_d^2}{4b^2 \text{Ja}_w \eta L}, \quad b = 1.56 \quad (5.53)$$

6

BOILING BUBBLE DYNAMICS

Contents

6.1	Introduction	38
6.1.1	Experimental Insights	38
6.1.2	Existing Approaches	40
6.2	Bubble Force Balance in Vertical Flow Boiling	44
6.2.1	Introduction	44
6.2.2	General Considerations	45
6.2.3	Buoyancy Force	45
6.2.4	Contact Pressure Force	46
6.2.5	Capillary Force	46
6.2.6	Drag and Lift Forces	47
6.2.7	Inertia Force	51
6.2.8	Force Balance Summary	54
6.2.9	Liquid Velocity	54
6.3	Bubble Growth	55
6.3.1	Introduction	55
6.3.2	Heat Diffusion in Uniformly Superheated Liquid	56
6.3.3	Microlayer Evaporation	57
6.3.4	Bubble Growth in Subcooled Flow Boiling	58
6.3.5	Analytic Approach of Bubble Growth in a Linear Thermal Boundary Layer .	59
6.3.6	Comparison with DNS Results	61
6.3.7	Comparison with Experimental Measurements	62
6.3.8	Conclusions on Bubble Growth Modeling	63
6.4	Departure by Sliding	65
6.4.1	Non-Dimensional Analysis	65
6.4.2	Application to Experimental Data	67
6.4.3	Departure Diameter Prediction	69
6.4.4	Discussion and accounting for parameters uncertainties	70
6.5	Sliding phase	73
6.5.1	Modeling	73
6.5.2	Low Pressure Sliding	73
6.5.3	High Pressure Sliding	74
6.5.4	Comparison of Forces in Sliding Stage	75
6.6	Bubble Lift-Off	78
6.6.1	Introduction	78
6.6.2	Experimental Measurements of Lift-Off Diameter	80
6.6.3	Influence of the Flow Boiling Conditions	80
6.6.4	Predicting the Lift-Off with a Force Balance	81
6.6.5	A Simple Non-Dimensional Correlation	83
6.6.6	Conclusion on the Lift-Off	83

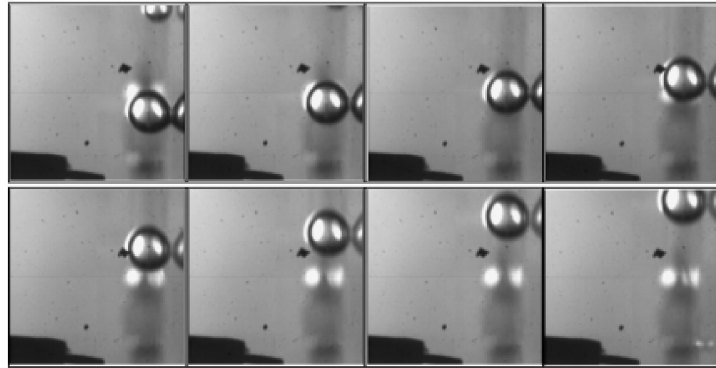
6.1 INTRODUCTION

Boiling bubble parameters are playing an important role in the Heat Flux Partitioning models. For instance, the evaporation heat flux ϕ_e is directly proportional to the bubble lift-off radius R_{lo} ?? while the quenching heat flux ϕ_q depends on the wall area visited by a bubble $A_{q,1b}$ (Eq. ??) which depends on the bubble sliding length l_{sl} , departure radius R_d and lift-off radius R_{lo} .

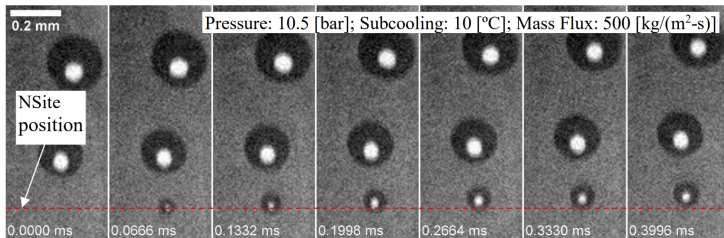
6.1.1 Experimental Insights

Consequently, many experimental investigations have been conducted to further understand the behavior of nucleated bubbles on a wall while facing a liquid flow. In the case of vertical flow boiling, a typical bubble life cycle can be described as follows:

- Beginning of nucleation, growth while attached to the nucleation site ;
- Detachment occurring at radius R_d , from which the bubble will start to slide and accelerate along the wall ;
- Lift-off from the wall at radius R_{lo} after sliding over a length l_{sl} .



(a) Bubble sliding visualized and adapted from Maity [35] at atmospheric pressure.



(b) Bubble sliding visualized and adapted from Kossolapov [28] at higher pressure.

Figure 6.1: Visualization of bubble sliding at various pressures.

This behavior has been supported by many experimental observations who clearly observed three stages (departure, sliding, lift-off) both at low pressure (Maity [35], Situ [56], Thorncroft [61], Prodanovic [45], Chen [4], Ren [49], etc.) and high pressure (March [36], Kossolapov [28]). Altogether, those works cover various flow conditions and operating fluids which insist on the generality of this bubble behavior in vertical flow boiling. Examples from the literature of visualizations of bubble sliding at atmospheric and high pressure are reproduced on Figure 6.1.

The bubble sliding process has also been thermally studied to quantify its impact over the wall heat transfer. Estrada-Perez *et al.* [14] observed the significant thermal impact of sliding bubbles footprints. Kossolapov [28] also investigated the sliding of boiling bubbles and measured the magnitude of the transient heat transfer induced by the disruption of the liquid thermal boundary layer in the bubble's wake. Typical experimental observations from those works are reproduced on Figure 6.2.

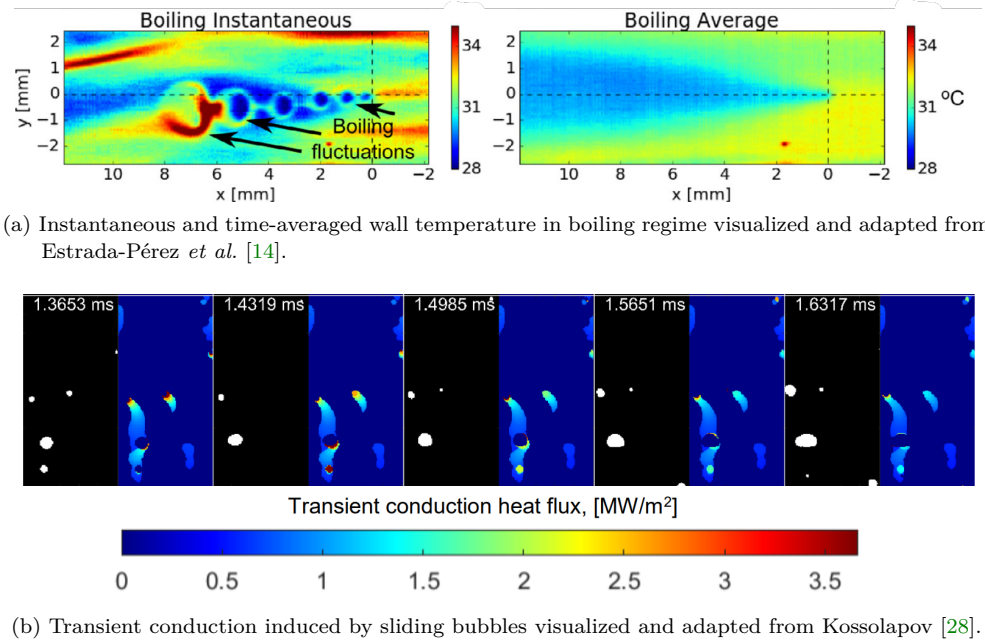


Figure 6.2: Visualization of bubble sliding thermal impact.

Those experimental observations highlight the significant magnitude of the transient heat transfer triggered by bubble movement on the wall that can represent up to 40% of the total wall heat flux [28]. All the aforementioned observations are summed-up on Figure ??.

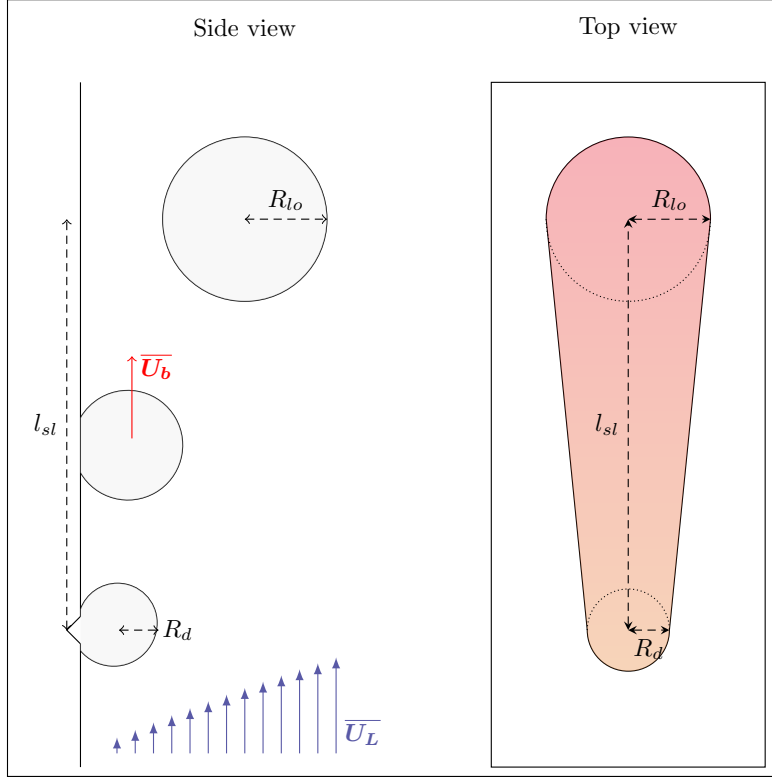


Figure 6.3: Sketch of a typical bubble lifetime in vertical flow boiling. Left depicts a typical side view of the heater with identification of departure, sliding and lift-off. Right depicts a top view of the heater, exhibiting the area that will undergo transient heat transfer.

Predicting the HFP in vertical flow boiling thus requires a descriptions of single bubble dynamics that includes accurate estimations of bubble departure and lift-off radii R_d and R_{lo} as well as bubble sliding velocity \bar{U}_b to predict the sliding length l_{sl} .

6.1.2 Existing Approaches

6.1.2.1 Departure / Lift-Off Diameters

Historically, first approaches to estimate the bubble diameter consisted of experimental-based correlations for pool boiling of horizontal surfaces through photographic studies. In those cases, departure from the nucleation site coincides with the bubble lift-off. Among the mainly used in HFP models and CFD, we can mention the law of Tolubinsky & Kostanchuk (1970)[63] which depends only on the local liquid subcooling:

$$D_{lo} = D_0 e^{-\Delta T_L/45}, \quad D_0 = 15\text{mm} \quad (6.1)$$

On the other hand, authors such as Cole & Rohsenow (1968) proposed relationships including the influence of pressure through the capillary length $L_c = \sqrt{\frac{\sigma}{g(\rho_L - \rho_V)}}$:

$$D_{lo} = CL_c \left(\frac{\rho_L c_{p,L} T_{sat}}{\rho_V h_{LV}} \right)^{5/4} \quad (6.2)$$

$C = 1.5 \times 10^{-4}$ for water and 4.65×10^{-4} otherwise.

This equations provides a good trend for the evolution of bubble departure diameter with pressure as shown by Kossolapov [28].

Later, Ünal (1976)[77] derived a correlation based on semi-analytical approach of the heat transfer mechanisms around a bubble to estimate its maximum diameter, including simultaneous influences of pressure, heater material, liquid velocity and subcooling:

$$D_{lo} = 2.42 \times 10^{-5} P^{0.709} \frac{a}{\sqrt{b\varphi}} \quad (6.3)$$

$$a = \frac{\Delta T_w \lambda_w}{2\rho_V h_{LV} \sqrt{\pi \eta_w}}$$

$$b = \frac{\Delta T_L}{2(1 - \rho_V/\rho_L)}$$

$$\varphi = \max \left(1 ; \left(\frac{U_L}{U_0} \right)^{0.47} \right), \quad U_0 = 0.61 \text{ m/s}$$

Ünal validated his law against several measurements from the literature covering pressures from 1 to 177 bars, liquid velocities from 0.08 to 9.15 m/s, subcoolings from 3 to 86K and heat fluxes from 0.47 to 10.64 MW/m².

Remark : The law of Ünal is used in the HFP model of Kurul & Podowski. It as also implemented in NEPTUNE_CFD and includes a correction of Borée *et al.* (Eq. ?? to avoid divergence in bubble diameter when reaching saturated conditions.

More recently, the several developments around HFP models has lead many researchers to propose dedicated correlations for bubble departure or lift-off diameter. For instance, Basu *et al.* fitted expressions for D_d and D_{lo} on their own measurements:

$$\frac{D_d}{L_c} = 1.3 \sin(\theta_s)^{0.4} \left[0.13 e^{-1.75 \times 10^{-4} Re_{L,D_h}} + 0.005 \right] Ja_w^{0.45} e^{-0.0065 Ja_L} \quad (6.4)$$

$$\frac{D_{lo}}{L_c} = 1.3 \sin(\theta_s)^{0.4} \left[0.2 e^{-1.28 \times 10^{-4} Re_{L,D_h}} + 0.005 \right] Ja_w^{0.45} e^{-0.0065 Ja_L} \quad (6.5)$$

They were validated for $14 \leq Ja_w \leq 56$, $1 \leq Ja_L \leq 138$, $0 \leq Re_{L,D_h} \leq 7980$ and $30^\circ \leq \theta_s \leq 90^\circ$.

Remark : Basu *et al.* use these own-developed laws in their HFP formulation to estimate bubble diameters.

Similarly, Kommajosyula gathered several bubble departure and lift-off diameter measurements from the literature and proposed the following reduced correlation:

$$D_d = 18.9 \times 10^{-6} \left(\frac{\rho_L - \rho_V}{\rho_V} \right)^{0.27} \text{Ja}_w^{0.75} (1 + \text{Ja}_L)^{-0.3} U_{L,bulk}^{-0.26} \quad (6.6)$$

$$D_{lo} = 1.2 D_d \quad (6.7)$$

Remark : Although this law (used in Kommajosyula's HFP model) present coherent trends with flow conditions, the raw presence of $U_{L,bulk}$ in the expression is questionable because:

- The relationship is not dimensionless and the constant 18.9×10^{-6} must be in $\text{m}^{1.26} \cdot \text{s}^{-0.26}$;
- The negative exponent will yield diverging values when reaching pool boiling conditions, which is physically inconsistent.

The same type of approach is conducted by Zhou *et al.* [74] by correlating low pressure measurements:

$$\frac{D_d}{L_o} = 10^{2.4086} \left(\frac{\rho_V}{\rho_L} \right)^{-0.6613} \text{Ja}_w^*^{0.1557} \text{Ja}_L^*^{-0.01592} \text{Re}_{L_o}^{-0.6647} \text{Pr}_L^{-1.8477} \sin(\theta_s)^{0.4} \quad (6.8)$$

$$\frac{D_{lo}}{L_c} = 10^{-1.1990} \left(\frac{\rho_V}{\rho_L} \right)^{-0.9785} \text{Ja}_w^*^{0.1435} \text{Ja}_L^*^{-0.0119} \text{Re}_{L_c}^{-0.5129} \text{Pr}_L^{-1.8784} \quad (6.9)$$

with the Reynolds numbers based on $L_o = \frac{\rho_L \nu_L^2}{\sigma}$ and L_c the capillary length, and $\text{Ja}^* = \frac{\rho_L c_{p,L}}{h_{LV}}$ reduced Jakob numbers that do not include the density ratio.

6.1.2.2 Sliding Length and Velocity

Regarding bubble sliding phase, one of the most used correlations to predict bubble diameter evolution has been developed by Maity [35]. Based on atmospheric pressure visualization of boiling single bubbles in water, it predicts the resulting sliding diameter D_{sl} provided a sliding time t_{sl} and initial diameter D_{in} through:

$$\frac{(D_{sl}^2 - D_{in}^2)}{t_{sl} \eta_L \text{Ja}_w} = \frac{1}{15 (0.015 + 0.023 \text{Re}_b^{0.5}) (0.04 + 0.023 \text{Ja}_L^{0.5})} \quad (6.10)$$

where $\text{Re}_b = \frac{U_L D_b}{\nu_L}$

Remark : This correlation is used in Basu *et al.* and Gilman & Baglietto HFP model.

Using Maity measurements of bubble sliding velocity, Basu *et al.* proposed an estimation of the sliding distance for a single bubble $l_{sl,0}$:

$$l_{sl,0} = \int_0^{t_{sl}} U_b \, dt = \int_0^{t_{sl}} C_U \sqrt{t} \, dt = \frac{2}{3} C_U t_{sl}^{3/2} \quad (6.11)$$

$$C_U = 3.2 U_L + 1 \quad (6.12)$$

where C_U represents a correlated acceleration coefficient.

Remark : Basu *et al.* also use this correlation in their model to estimate the bubble sliding length. The estimation of the bubble sliding velocity through an explicit correlation since it varies over the bubble lifetime. Therefore, some authors simply suppose that $U_b = U_L$ such as Gilman & Baglietto.

Other assumptions regarding the sliding length relies on the value of the bubble density on the heater N_{bub} . By supposing that bubbles usually lift-off after coalescing with an other, thus traveling the average distance between two bubbles:

$$l_{sl} = \frac{1}{\sqrt{N_{bub}}} \quad (6.13)$$

Remark : This modeling choice is made by Kommajosyula. Zhou *et al.* choose the minimum value between the $l_{sl,0}$ of Basu (Eq. 6.11) and this average distance between bubbles.

6.1.2.3 Conclusion on Correlations

Albeit proposing coherent trend with the flow boiling conditions along with good estimations of the desired parameters on given experimental datasets, explicit correlations inherently include a limited range of application. Moreover, the constant increase of the number of works proposing data-fitted laws makes the selection of a proper relationship a complicated matter due to their potential lack of generality.

To try to overcome this drawback and come up with more generalized models, researchers have explored an alternative approach by developing Mechanistic Models based on a force-balance to precisely depict the external efforts experienced by the growing bubble. The goal is to compute the sum of the forces applied to the bubble over its growing time and to detect departure and lift-off events using associated criteria such as a change in the force balance sign. This will be the subject of the next section.

As a summary, we gather the presented correlations on Table 6.1.

Bubble Departure Diameter	
Author (Year)	Correlation
Basu <i>et al.</i> (2005)	$\frac{D_d}{L_c} = 1.3 \sin(\theta_s)^{0.4} \left[0.13 e^{-1.75 \times 10^{-4} \text{Re}_{L,D_h}} + 0.005 \right] \text{Ja}_w^{0.45} e^{-0.0065 \text{Ja}_L}$ $L_c = \sqrt{\frac{\sigma}{g(\rho_L - \rho_V)}}$
Kommajosyula (2020)	$D_d = 18.9 \times 10^{-6} \left(\frac{\rho_L - \rho_V}{\rho_V} \right)^{0.27} \text{Ja}_w^{0.75} (1 + \text{Ja}_L)^{-0.3} U_{L,bulk}^{-0.26}$
Zhou (2021)	$\frac{D_d}{L_o} = 10^{2.4086} \left(\frac{\rho_V}{\rho_L} \right)^{-0.6613} \text{Ja}_w^{*0.1557} \text{Ja}_L^{*-0.01592} \text{Re}_{L_o}^{-0.6647} \text{Pr}_L^{-1.8477} \sin(\theta_s)^{0.4}$ $L_o = \frac{\rho_L \nu_L^2}{\sigma}$
Bubble Lift-Off Diameter	
Author (Year)	Correlation
Tolubinsky & Kostanchuk (1970)	$D_{lo} = D_0 e^{-\Delta T_L / 45}, D_0 = 15 \text{mm}$
Cole & Rohsenow (1968)	$D_{lo} = CL_c \left(\frac{\rho_L c_{p,L} T_{sat}}{\rho_V h_{LV}} \right)^{5/4}$ $C = 1.5 \times 10^{-4} \text{ (water)} \text{ or } 4.65 \times 10^{-4} \text{ (other)}, L_c = \sqrt{\frac{\sigma}{g(\rho_L - \rho_V)}}$
Ünal (1976)	$D_{lo} = 2.42 \times 10^{-5} P^{0.709} \frac{a}{\sqrt{b\varphi}}, a = \frac{\Delta T_w \lambda_w}{2\rho_V h_{LV} \sqrt{\pi \eta_w}}$ $b = \frac{\Delta T_L}{2(1 - \rho_V/\rho_L)}, \varphi = \max \left(1 ; \left(\frac{U_L}{U_0} \right)^{0.47} \right), U_0 = 0.61 \text{ m/s}$
Basu <i>et al.</i> (2005)	$\frac{D_{lo}}{L_c} = 1.3 \sin(\theta_s)^{0.4} \left[0.2 e^{-1.28 \times 10^{-4} \text{Re}_{L,D_h}} + 0.005 \right] \text{Ja}_w^{0.45} e^{-0.0065 \text{Ja}_L}$ $L_c = \sqrt{\frac{\sigma}{g(\rho_L - \rho_V)}}$
Kommajosyula (2020)	$D_{lo} = 1.2 D_d$
Zhou (2021)	$\frac{D_{lo}}{L_c} = 10^{-1.1990} \left(\frac{\rho_V}{\rho_L} \right)^{-0.9785} \text{Ja}_w^{*0.1435} \text{Ja}_L^{*-0.0119} \text{Re}_{L_c}^{-0.5129} \text{Pr}_L^{-1.8784}$ $L_c = \sqrt{\frac{\sigma}{g(\rho_L - \rho_V)}}$
Sliding Length, Diameter and Velocity	
Author (Year)	Correlation
Maity (2000)	$\frac{(D_{sl}^2 - D_{in}^2)}{t_{sl} \eta_L \text{Ja}_w} = \left[15 \left(0.015 + 0.023 \text{Re}_b^{0.5} \right) \left(0.04 + 0.023 \text{Ja}_L^{0.5} \right) \right]^{-1}$ $\text{Re}_b = \frac{U_L D_b}{\nu_L}$
Basu <i>et al.</i> (2005)	$l_{sl,0} = \frac{2}{3} C_U t_{sl}^{3/2}, C_U = 3.2 U_L + 1$
Bubble Density Average Distance	$l_{sl} = \frac{1}{\sqrt{N_{bub}}}$

Table 6.1: Summary of the presented correlations

6.2 BUBBLE FORCE BALANCE IN VERTICAL FLOW BOILING

6.2.1 Introduction

The derivation of the force balance over a growing bubble on a wall in a liquid flow is a very complicated problem that many researchers have tried to tackle over the past decades. Many theoretical and numerical approaches have been conducted to estimate the forces at stake in bubble dynamics and sometimes compared to experimental visualization of bubbles in movement.

Among the first propositions of the whole force-balance closure, the work of Klausner *et al.* in 1993 [24] is probably among the most referred to. They proposed a tentatively complete force-balance for a growing bubble in a boiling flow and supposed that departure from the nucleation site is reached when the force balance becomes positive either in the direction of the flow or perpendicular to the wall. They validated their approach against measurements for horizontal flow boiling of refrigerant R113.

In the same framework, many subsequent works were published such as:

- Van Helden *et al.* [66] (1995) who assessed forces coefficients using injected air bubbles in a vertical flow ;
- Thorncroft *et al.* [61, 62] (1998, 2001) who conducted experiments on horizontal and vertical flow boiling of R113 while proposing more general formulations of the force balance that were used to predict bubble diameter measurements ;
- Duhar & Colin [13] (2006) who validated a force balance on bubbles created by air injection in a shear flow. They extended their work with boiling N-pentane experiments and studied the growth and detachment of single bubbles [11] ;
- Van Der Geld (2009) [18] used potential flow theory to analytically derive the force balance for deforming bubbles near a plane ;
- Sugrue *et al.* (2014) [59] conducted measurements on boiling bubble for water at atmospheric pressure and various surface orientations. Their measurements were then used to validate a force-balance approach predicting bubble departure by sliding [58] ;
- Mazzocco *et al.* (2018) [37] gathered several measurements of bubble departure and lift-off diameters and proposed a reassessed force-balance approach including new drag coefficient and growth law to achieve predictions with a reasonable accuracy over the database ;
- Ren *et al.* (2020) [49] measured bubble departure diameter for vertical flow boiling of water up to 5 bars which they used to validate a force-balance model.

While not exhaustive, this list aims to show that force-balance modeling has become an increasingly interesting approach for authors. It is though not exempted of limitations because each force requires a proper modeling which needs sometimes to go through empirical choices as we will later discuss. This drawback is particularly noted by Bucci *et al.* [2] who points out that traditional force balances are not equal to zero when the bubble is immobile. On the other hand, they show that this is not due to the absence of unknown forces in the balance but rather associated to the computation of well-known forces such as capillary forces. Moreover, Duhar & Colin [13] managed to reach a zero total balance for their air-injected bubbles, and emphasized the interest of force modeling to deeper understand the physical phenomena behind bubble dynamics.

Each of the previously listed models proposed different upgrades and modifications to the force balance over the bubble. Unfortunately, they were all validated using low pressure experiments due to the lack of pressurized measurements in the literature. In addition, the mentioned common use of empirical parameters makes it difficult to reach a general validation of those models as we will see.

In this section, we aim to propose an update of the bubble force balance for vertical flow boiling with a reduced empiricism and to cover the whole bubble lifetime (departure, sliding, lift-off) while achieving a larger generality by including pressurized measurements up to 40 bar conducted by Kossolapov [28].

6.2.2 General Considerations

When trying to derive the force balance over a bubble, the first step consists of splitting the whole effort experienced by the bubble between different contributions depending on their nature. In our case, we focus on a bubble growing on a vertical wall and facing an upward flow as depicted in Figure 6.4.

Static forces :

- The buoyancy force $\overline{F_B}$, including Archimedes force and the weight of the bubble ;
- The capillary or surface tension force $\overline{F_C}$;
- The contact pressure force $\overline{F_{CP}}$.

Hydrodynamic forces :

- The drag and lift forces $\overline{F_D}$ and $\overline{F_L}$;
- The inertia force $\overline{F_I}$, including added-mass and Tchen force.

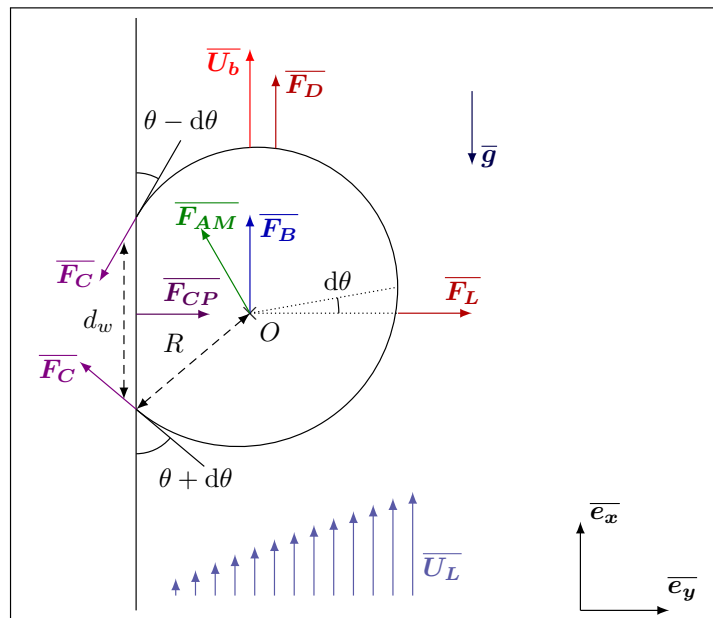


Figure 6.4: Sketch of the forces applied to the bubble facing an upward flow $\overline{U_L}$ and sliding at velocity $\overline{U_b}$

Regarding the bubble shape, we consider a quasi-spherical bubble of radius R with a circular contact area with the wall of radius r_w . It has a static contact angle θ and is tilted under the influence of the flow by an inclination angle $d\theta$ (half the total angle hysteresis). The resulting downstream and upstream contact angles are therefore $\theta_d = \theta - d\theta$ and $\theta_u = \theta + d\theta$. If the bubble has a shape close to a truncated sphere, we can approximate the bubble foot radius as:

$$r_w \approx R \sin \left(\frac{\theta_u + \theta_d}{2} \right) = R \sin (\theta) \quad (6.14)$$

Some authors rather take $r_w \approx \frac{1}{2}R (\sin (\theta_u) + \sin (\theta_d)) = R \sin (\theta) \cos (d\theta)$, however this expression tends to zero when reaching $d\theta \rightarrow 90^\circ$ which is undesirable regarding the expression of forces such as Contact Pressure and Surface Tension.

We suppose $V_b \approx \frac{4}{3}\pi R^3$ for the bubble volume.

6.2.3 Buoyancy Force

The buoyancy force results from both the weight of the bubble and the integration of the hydrostatic liquid pressure over its surface which naturally yields:

$$\overline{F_B} = \rho_V V_b \bar{g} + \left(\iint_{S_b} \rho_L g z \, d^2 S \right) \bar{e}_x = V_b (\rho_V - \rho_L) \bar{g} = \frac{4}{3}\pi R^3 (\rho_L - \rho_V) g \bar{e}_x \quad (6.15)$$

6.2.4 Contact Pressure Force

The contact pressure force arises due to the pressure difference between the center of the bubble and the surrounding liquid. Combined with the Archimedes force, it can be expressed versus the difference of liquid and vapor pressure at the bubble foot using Laplace's equation $\Delta P = 2\sigma/R_c$ as:

$$\overline{F_{CP}} \approx \frac{2\sigma}{R_c} \pi r_w^2 \overline{e_y} \approx \pi R \sigma 2 \sin(\theta)^2 \overline{e_y} \quad (6.16)$$

Here, R_c is the curvature radius of the bubble which is often assumed to be equal to $5R$ [24, 37, 58] without other explanation than avoiding an overestimation of the contact pressure force. To avoid this arbitrary choice, following the hypothesis of a nearly spherical bubble shape gives $R_c = R$.

6.2.5 Capillary Force

The capillary force acts at the triple contact line at the bubble's foot and is an important adhesive force maintaining the bubble attached to the wall. Its derivation can be done by integration of the effort exerted over the triple contact line. Noting Φ the polar angle around the bubble foot, we have :

$$\overline{F_C} = 2 \int_0^\pi \sigma r_w \bar{\tau}(\Phi) d\Phi \quad (6.17)$$

where $\bar{\tau}$ is the unit vector tangent to the interface.

To compute the resulting components parallel and tangent to the wall, Klausner *et al.* [24] account for a contact angle difference between the upstream (receding) contact angle θ_u and downstream (advancing) contact angle θ_d . If the local contact angle is noted γ , then:

$$\bar{\tau}(\Phi) = \cos(\gamma) \cos(\Phi) \overline{e_x} + \sin(\gamma) \overline{e_y} \quad (6.18)$$

Then representing the evolution of the local contact angle γ from θ_u to θ_d using a polynomial expression of degree 3:

$$\gamma(\Phi) = \theta_d + (\theta_u - \theta_d) \left[3 \left(\frac{\Phi}{\pi} \right)^2 - 2 \left(\frac{\Phi}{\pi} \right)^3 \right], \quad 0 \leq \Phi \leq \pi \quad (6.19)$$

which verifies symmetry conditions:

$$\gamma'(0) = \theta_d, \quad \gamma(\pi) = \theta_u, \quad \gamma'(0) = \gamma'(\pi) = 0 \quad (6.20)$$

To obtain analytic expression, Klausner *et al.* also consider a first order linear interpolation:

$$\gamma(\Phi) = \theta_d + (\theta_u - \theta_d) \frac{\Phi}{\pi} \quad (6.21)$$

This yields:

$$\overline{F_C} = -2r_w \sigma \frac{\pi(\theta_u - \theta_d)}{\pi^2 - (\theta_u - \theta_d)^2} (\sin(\theta_u) + \sin(\theta_d)) \overline{e_x} - 2r_w \sigma \frac{\pi}{\theta_u - \theta_d} (\cos(\theta_d) - \cos(\theta_u)) \overline{e_y} \quad (6.22)$$

By comparing the analytic expression of Eq. 6.22 with the values obtained by numerical integration of Eq. 6.19, Klausner *et al.* introduce a correction factor of 1.25 over the x component, finally giving :

$$\overline{F_C} = -2.5r_w \sigma \frac{\pi(\theta_u - \theta_d)}{\pi^2 - (\theta_u - \theta_d)^2} (\sin(\theta_u) + \sin(\theta_d)) \overline{e_x} - 2r_w \sigma \frac{\pi}{\theta_u - \theta_d} (\cos(\theta_d) - \cos(\theta_u)) \overline{e_y} \quad (6.23)$$

$$= -\pi R \sigma \underbrace{\left[2.5 \frac{r_w}{R} \frac{d\theta}{(\frac{\pi}{2})^2 - d\theta^2} \sin(\theta) \cos(d\theta) \right]}_{f_{C,x}} \overline{e_x} - \pi R \sigma \underbrace{\left[2 \frac{r_w}{R} \sin(\theta) \frac{\sin(d\theta)}{d\theta} \right]}_{f_{C,y}} \overline{e_y} \quad (6.24)$$

Remark : We can see that $f_{C,x} \rightarrow 0$ and $f_{C,y} \rightarrow 2 \frac{r_w}{R} \sin(\theta)$ when $d\theta \rightarrow 0$. In that case, $\overline{F_C} = -\overline{F_{CP}}$.

6.2.6 Drag and Lift Forces

The external liquid flow over the bubble induces the well-known drag and lift forces, acting respectively in the flow direction and perpendicular to the flow. They are usually expressed using associated coefficients C_D and C_L defined by:

$$\overline{F_D} = \frac{1}{2} C_D \rho_L S_p \left| \overline{U_L} - \overline{U_b} \right| (\overline{U_L} - \overline{U_b}) \quad (6.25)$$

$$\overline{F_L} = \frac{1}{2} C_L \rho_L S_p \left| \overline{U_L} - \overline{U_b} \right|^2 \overline{e_y} \quad (6.26)$$

with $S_p = \pi R^2$ the projected area of the bubble in the direction of the flow.

6.2.6.1 Drag Coefficient

Derivations of analytic expressions for the drag coefficient in an infinite fluid medium exist for more than a century, starting with Hadamard-Rybinski (1911) [21]:

$$C_D = \frac{16}{\text{Re}_b}, \text{ if } \text{Re}_b < 1 \quad (6.27)$$

where $\text{Re}_b = \frac{|U_{rel}| D_B}{\nu_L}$ is the bubble Reynolds number and U_{rel} the relative velocity between the bubble and the surrounding fluid.

For $\text{Re}_b \gg 1$, Levich (1962) [33] found for a potential flow:

$$C_D = \frac{48}{\text{Re}_b} \quad (6.28)$$

For intermediate values of Re_b , traditional approaches rely on expressions of the drag force for a bubble in an infinite medium based on numerical correlations as proposed by Mei & Klausner [40], used in many different mechanistic approaches [4, 49, 58, 62, 72]:

$$C_{D,U} = \frac{16}{\text{Re}_b} \left[1 + \left(\frac{8}{\text{Re}_b} + \frac{1}{2} \left(1 + \frac{3.315}{\sqrt{\text{Re}_b}} \right) \right)^{-1} \right] \quad (6.29)$$

Results from DNS conducted by Legendre *et al.* [31] proposed expressions of the drag and lift forces for a hemispherical bubble on a wall facing a viscous shear flow. Earlier, Legendre & Magnaudet [31] analytically derived coefficients to transpose drag and lift expressions for a particle to the case of a bubble. This was applied by Mazzocco *et al.* [37] to the Drag for a solid particle near a wall in a shear flow proposed by Zeng *et al.* [73].

In this work, we propose to rely on the recent work of Shi *et al.* [55] who conducted DNS of a shear flow over a spherical bubble of constant radius close to a wall for bubble Reynolds number between 10^{-1} and 10^3 and non-dimensional shear rates between -0.5 and 0.5. A sketch of the situation simulated by Shi *et al.* is depicted on Figure 6.5.

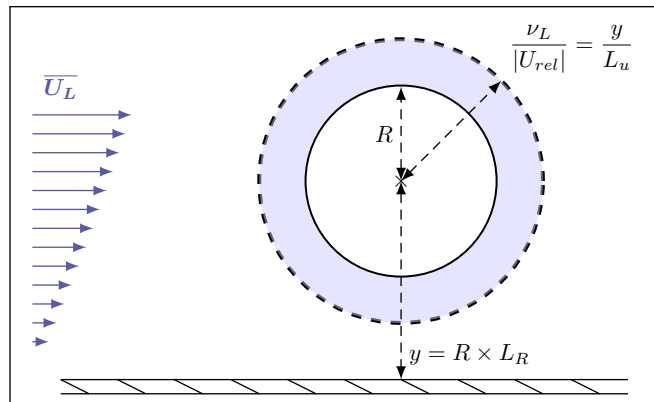


Figure 6.5: Physical situation considered by Shi *et al.* [55].

They computed the resulting drag and lift coefficients for each simulations and proposed correlations fitting their numerical results. The total Drag coefficient is expressed as a correction of the Drag coefficient for a bubble in an unbounded uniform flow $C_{D,U}$. The total drag is given by:

$$C_D = (1 + \Delta C_D) C_{D,U} \quad (6.30)$$

where ΔC_D accounts for both the effect of the shear flow and the wall vicinity.

To cover the whole range of bubble Reynolds numbers, correlations at low and high Re_b are smoothly connected using an exponential term.

$$\Delta C_D = \Delta C_{D,Re_b=O(1)} + \left(1 - e^{-0.07Re_b}\right) \Delta C_{D,Re_b \gg 1} \quad (6.31)$$

Each of those corrections is computed depending on Re_b , the non-dimensional shear rate $Sr = \frac{2\gamma R}{|U_{rel}|}$ where $\gamma = \frac{\partial U_{L,x}}{\partial y}$, the non dimensional wall distance $L_R = \frac{y}{R}$ ($L_R = 1$ being a spherical bubble laying on a wall) and non-dimensional viscous (or Stokes) length $L_u = \frac{y}{\nu_L / |U_{rel}|}$.

$$\begin{aligned} \Delta C_{D,Re_b=O(1)} &= \frac{1 + \tanh(0.012Re_b^{0.8}) + \tanh(0.07Re_b^{0.8})^2}{1 + 0.16L_u(L_u + 4)} \\ &\times \left[\left(\frac{3}{8}L_R^{-1} + \frac{3}{64}L_R^{-4} \right) \left(1 - \frac{3}{8}L_R^{-1} - \frac{3}{64}L_R^{-4} \right)^{-1} - \frac{1}{16} \left(L_R^{-2} + \frac{3}{8}L_R^{-3} \right) Sr \right] \end{aligned} \quad (6.32)$$

$$\Delta C_{D,Re_b \gg 1} = 0.47L_R^{-4} + 0.0055L_R^{-6}Re_b^{3/4} + 0.002|Sr|^{1.9}Re_b + 0.05L_R^{-7/2}SrRe_b^{1/3} \quad (6.33)$$

Figure 6.6 shows the evolution of the drag correction ΔC_D against the bubble Reynolds number for different distances to the wall L_R and two values of Sr . We can see that as the distance between the wall and the bubble increases the drag correction logically approaches zero and that increasing the shear rate Sr increases ΔC_D for higher values of Re_b .

Shi *et al.* [55] conducted DNS for wall distances down to $L_R = 1.5$. However, Scheiff *et al.* [52] compared the values obtained for $L_R = 1$ with measured drag coefficients of bubbles sliding on a wall and observed a good agreement, which legitimates the use of this new drag correlation by extending its application to the case of a bubble laying on a wall and using the uniform drag coefficient of Eq. 6.29.

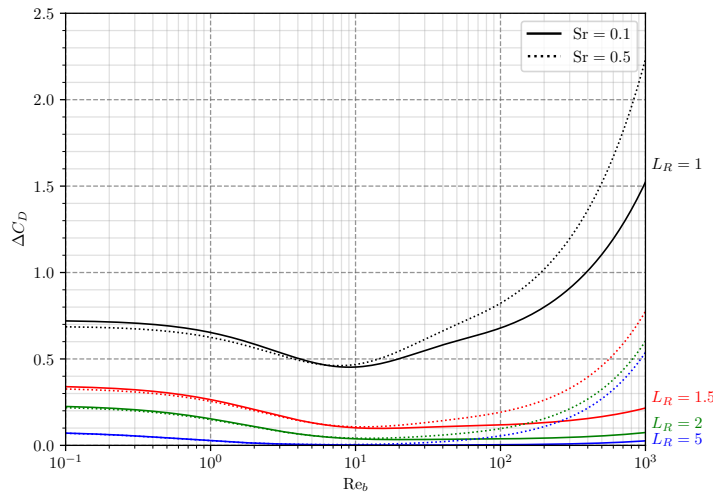


Figure 6.6: Drag correction from Shi *et al.* [55].

Remark : In PWR conditions, a static bubble of radius 0.01 mm on a wall with a bulk liquid velocity of 5 m/s leads to a non-dimensional shear rate $Sr \approx 0.7$ with $Re_b \approx 500$. In this case, the drag correction can reach 180% compared to the unbounded uniform flow formulation.

6.2.6.2 Lift Coefficient

In 1987, Auton *et al.* [1] analytically derived the lift force for an inviscid fluid in unstationary motion in a weak velocity gradient and found $C_L = 0.5$, with the lift force defined as:

$$\overline{F_L} = -\rho_L C_L V_b (\overline{U_L} - \overline{U_b}) \wedge \overline{\omega} \quad (6.34)$$

where $\overline{\omega}$ is the flow vorticity.

This result was enriched by Legendre & Magnaudet (1998) [31] who used numerical results to propose a dependency of C_L on the bubble Reynolds number for a sphere in an infinite medium facing a weakly sheared flows as:

$$C_L = (C_{L,\text{Re}_b \sim 1}^2 + C_{L,\text{Re}_b \gg 1}^2)^{1/2} \quad (6.35)$$

$$= \left(\left[\frac{6}{\pi^2} \frac{2.255 (\text{Re}_b \omega^*)^{-1/2}}{\left(1 + 0.2 \frac{\text{Re}_b}{\omega^*} \right)^{3/2}} \right]^2 + \left[\frac{1}{2} \frac{1 + 16 \text{Re}_b^{-1}}{1 + 29 \text{Re}_b^{-1}} \right]^2 \right)^{1/2} \quad (6.36)$$

where $\omega^* = \frac{2R |\overline{\omega}|}{|U_{\text{rel}}|}$ is the non-dimensional vorticity of the flow.

Remark : In the case of a steady linear shear flow near a wall, the vorticity is $\overline{\omega} = \nabla \wedge \overline{U_L} = -\gamma \overline{e_y}$.

In that case, the non-dimensional vorticity becomes the non-dimensional shear rate : $\omega^* = \frac{2R\gamma}{|U_{\text{rel}}|} = \text{Sr}$.

Later, Mei & Klausner (1994) [39] derived the lift force induced by the shear for a spherical bubble in an unbounded flow for low Reynolds numbers, based on the expression of Saffmann [51]. By interpolating this result with the solution of Auton [1], they obtained a formulation for a large range of Re_b :

$$C_L = 2.74 \sqrt{\text{Sr}} \times \left[\text{Re}_b^{-2} + (0.24 \sqrt{\text{Sr}})^4 \right]^{1/4} \quad (6.37)$$

This expression is actually used in many mechanistic force balance [4, 24, 49, 58].

In his force-balance approach, Mazzocco *et al.* [37] used a constant lift coefficient by using the upper bound for the lift of a solid particle touching a wall in a Stokes flow, multiplied by $\frac{4}{9}$ to transpose this value to the bubble case as suggested by Legendre & Magnaudet [31]. This resulted in:

$$C_L = 2.61 \quad (6.38)$$

In accordance with the computation of the drag coefficient, our model will rely on the expression of the lift coefficient proposed by Shi *et al.* [55]. Their formulation includes extra parameters compared to the drag coefficient :

- The non-dimensional Saffman length $L_\omega = \frac{y}{\sqrt{\nu_L/\omega}}$;
- The Stokes (or Oseen) length to Saffman length ratio $\varepsilon = \frac{\nu_L / |U_{\text{rel}}|}{\sqrt{\nu_L/\omega}}$, which quantifies the origin of inertial effects being either shear ($\varepsilon > 1$) or the relative slip of the bubble ($\varepsilon < 1$).

The resulting formulation of C_L corresponds to the superpositions of two contributions respectively associated to the uniform flow and the shear rate, both coupled with the wall presence.

$$C_L^W = C_{Lu}^W + C_{L\omega}^W \quad (6.39)$$

The lift associated to the uniform flow near a wall is computed as follows:

$$C_{Lu}^W = e^{-0.22 \varepsilon^{0.8} L_\omega^{2.5}} \frac{[1 + \tanh(0.012 \text{Re}_b^{0.8}) + \tanh(0.07 \text{Re}_b^{0.8})]^2}{1 + 0.13 L_u (L_u + 0.53)} \\ \times \left(\frac{L_R}{3}\right)^{-2.0} \tanh(0.01 \text{Re}_b) C_{Lu}^{\text{W-in}} \\ + \left(1 - e^{-0.22 \text{Re}_b^{0.6}}\right) [C_{Lu, \text{Re}_b \rightarrow \infty}^W + 15 \tanh(0.01 \text{Re}_b) \text{Re}_b^{-1} L_R^{-4}] \quad (6.40)$$

Where:

$$C_{Lu}^{\text{W-in}} = \frac{1}{2} \left(1 + \frac{1}{8} L_R^{-1} - \frac{33}{64} L_R^{-2}\right) \quad (6.41)$$

$$C_{Lu, \text{Re}_b \rightarrow \infty}^W = -\frac{3}{8} L_R^{-4} \left[1 + \frac{1}{8} L_R^{-3} + \frac{1}{6} L_R^{-5}\right] + O(L_R^{-10}) \quad (6.42)$$

The lift associated to the vorticity near a wall is computed as follows:

$$C_{L\omega}^W = \left[1 - \exp\left(-\frac{11}{96} \pi^2 \frac{L_\omega}{J_L(\varepsilon)} \left(1 + \frac{9}{8} L_R^{-1} - \frac{1271}{3520} L_R^{-2}\right)\right)\right] C_{L\omega, \text{Re}_b \ll 1}^U \quad (6.43)$$

$$+ \left(1 - e^{-0.3 \text{Re}_b}\right) \left[1 + 0.23 L_R^{-7/2} \left(1 + 13 \text{Re}_b^{-1/2}\right)\right] C_{L\omega, \text{Re}_b \gg 1}^U \quad (6.44)$$

Where:

$$J_L(\varepsilon) = 2.254 (1 + 0.2\varepsilon^{-2})^{-3/2} \quad (6.45)$$

$$C_{L\omega, \text{Re}_b \ll 1}^U = \frac{8}{\pi^2} \frac{\text{Sr}}{|\text{Sr}|} \varepsilon J_L(\varepsilon) \quad (6.46)$$

$$C_{L\omega, \text{Re}_b \gg 1}^U = \frac{2}{3} \text{Sr} (1 - 0.07 |\text{Sr}|) \frac{1 + 16 \text{Re}_b^{-1}}{1 + 29 \text{Re}_b^{-1}} \quad (6.47)$$

On Figure 6.7, we plot the values of C_L obtained by the formulation of Shi *et al.* different values of the non-dimensional wall distance L_R (extending down to $L_R = 1$) and non-dimensional shear rate Sr.

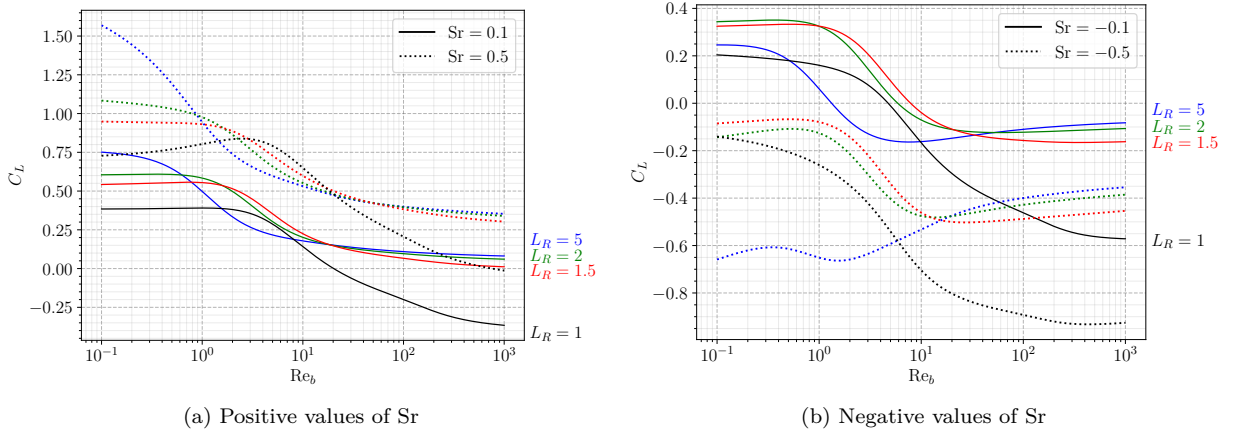


Figure 6.7: C_L computed using Shi *et al.* correlation.

We can see that the magnitude of the lift coefficient globally increases with the wall distance when $\text{Sr} > 0$ and that negative lift values are easily reached when $\text{Sr} < 0$. This means that correlations for unbounded medium may overestimate the lift experienced by the bubble compared to the situation with a wall.

The extension to the case $L_R = 1$ may be more questionable compared to the drag since the bubble touching the wall will stop any flow in between, leading to inertial and shear regimes that would be significantly different due to the redirection of the liquid at the bubble's foot towards the bulk. In particular, we can see that the values reached for $L_R = 1$ on Figure 6.7 are not following the general trend of simulated L_R :

- Negative values of C_L are reached with positive Sr at high Re_b while getting close to the wall seemed to tend to a value of $C_L \geq 0$ at high Re_b ;
- Magnitude of C_L with negative Sr are not coherent with the observed trend down to $L_R = 1.5$.

This observation suggest that we should include the effect of the wall using the lift of Shi *et al.* by limiting its use to $L_R = 1.5$ contrary to the drag which extension to $L_R = 1.0$ was coherent and validated.

Remark : In PWR conditions, taking $Sr \approx 0.7$ with $Re_b \approx 500$ for the static bubble on a wall leads to $C_L \approx 0.45$ both with Mei & Klausner (Eq. 6.37) and Shi *et al.* (Eq. 6.39). For a bubble that would slide at 90% of the local liquid velocity, this gives $Sr \approx 7$ and $Re_b \approx 50$ yielding $C_{L,Mei} \approx 4$ and $C_{L,Shi} \approx 2.8$.

6.2.7 Inertia Force

The Inertia force originates from various effects (bubble growth, freestream and bubble acceleration, etc.) and includes both added mass and Tchen forces and is expressed as presented in Magnaudet & Eames (2000) [34]:

$$\overline{F_I} = \underbrace{\rho_L V_b \left(\frac{\partial \overline{U_L}}{\partial t} + \overline{\nabla}(\overline{U_L}) \cdot \overline{U_L} \right)}_{\text{Liquid inertia or Tchen force}} + \underbrace{\frac{d}{dt} (\rho_L C_{AM} V_b (\overline{U_L} - \overline{U_b}))}_{\text{Added Mass force } \overline{F_{AM}}} \quad (6.48)$$

Since we consider a steady and quasi-parallel liquid flow, we respectively have:

$$\frac{\partial \overline{U_L}}{\partial t} = 0 \text{ and } \overline{\nabla}(\overline{U_L}) cdot \overline{U_L} = 0 \quad (6.49)$$

Thus only remains the added mass force to express in the considered force balance. In the next subsections, we detail former approaches to tackle the added mass derivation and propose a more rigorous to re-evaluate the added mass coefficients.

6.2.7.1 Former Approaches

In previous mechanistic models, the derivation of the added mass force was conducted with different approaches. In particular, some authors chose to rely on the Rayleigh-Plesset Equation (RPE) for a growing hemispherical bubble in a quiescent flow to obtain the reaction force from the liquid, oriented perpendicularly to the wall:

$$\overline{F_{AM,RPE}} = -\rho_L \pi R^2 \left[R \ddot{R} + \frac{3}{2} \dot{R}^2 \right] \overline{e_y} \quad (6.50)$$

Then, assuming a bubble inclination angle θ_i , this force was projected along the x axis to obtain an Added Mass force parallel to the wall that hinders departure. The inclination angle value is often empirical and used for data fitting [7, 37, 49, 72].

$$\overline{F_{AM,RPE}} = -\rho_L \pi R^2 \left[R \ddot{R} + \frac{3}{2} \dot{R}^2 \right] (\sin(\theta_i) \overline{e_x} + \cos(\theta_i) \overline{e_y}) \quad (6.51)$$

This approach is questionable on different aspects. First, the RPE assumes a moving boundary in a quiescent unbounded liquid, which is physically far from the real situation of a bubble growing on a wall in a boiling flow. Moreover, the subsequent projection along the different directions regarding an unknown angle is hardly reasonable if θ_i is chosen arbitrarily. Values of θ_i selected by different authors are mentioned in Table 6.2.

On the other hand, some authors [19, 24, 62] considered two distinct contributions:

- Hemispherical bubble growth in a stagnant liquid, leading to Eq. 6.51 including the inclination angle θ_i ;

- Spherical bubble growth in an uniform unbounded and inviscid liquid flow, which yields a detaching Added Mass term due to the interaction of bubble growth with the external flow:

$$\overline{F_{AM,U}} = \frac{3}{2} \rho_L V_b \frac{\dot{R}}{R} U_L \overline{e_x} \quad (6.52)$$

This last term is usually called a "bulk growth force". By including the effect of the liquid flow, this approach can be considered as closer to the reality. However, it relies on two separate derivations associated to different physical considerations.

6.2.7.2 Proposed Approach

To tackle the added mass derivation in a proper way, we propose to follow the approach of Lamb [29] (also presented by Milne Thomson [42] or Van Winjaarden [67]). By solving the potential flow around a bubble and its image, we can obtain the total liquid kinetic energy E_L that corresponds to a situation where a bubble is at a given distance from a wall (represented by the line normal to the line of centers of the bubbles).

Then we can use Lagrange equation to compute the resulting forces along a given coordinate q :

$$F_{AM,q} = -\frac{\partial}{\partial t} \left(\frac{\partial E_L}{\partial \dot{q}} \right) + \frac{\partial E_L}{\partial q} \quad (6.53)$$

$$(6.54)$$

This method was also used by Duhar [13] who developed an asymptotic expression of E_L to compute the addd mass coefficient when the bubble approaches the wall. Here, we express the liquid kinetic energy by relying on the work of Van Der Geld [18] who derived E_L in the case of a full or truncated spherical bubble laying on a wall and facing an uniform flow parallel to the wall of velocity U_L (Eq. 6.55). If the bubble slides at a velocity $U_b = \dot{x}$, it sees a liquid velocity $U_{rel} = U_L - \dot{x}$.

$$E_L = \frac{\rho_L V_b}{2} \left(\alpha \dot{y}^2 + \text{tr}(\beta) \dot{R}^2 + \psi \dot{R} \dot{y} + \alpha_2 (U_L - \dot{x})^2 \right) \quad (6.55)$$

where (x, y) are the coordinates of the bubble's center and α , $\text{tr}(\beta)$, ψ , α_2 are polynomials of $R/y = 1/L_R$ derived by Van Der Geld for $1 < R/y < 2$ i. e. $0.5 < L_R < 1$, corresponding to contact angles $0^\circ < \theta < 60^\circ$.

For each polynomial expression (α is used as an example), we note n its degree and write:

$$\alpha = \sum_{k=0}^n \alpha_k \left(\frac{R}{y} \right)^k \text{ and } \tilde{\alpha} = \sum_{k=0}^n k \alpha_k \left(\frac{R}{y} \right)^k \quad (6.56)$$

This allows to express the following derivatives:

$$\frac{\partial \alpha}{\partial y} = -\frac{1}{y} \tilde{\alpha} \text{ and } \frac{\partial \alpha}{\partial t} = \left(\frac{\dot{R}}{R} - \frac{\dot{y}}{y} \right) \tilde{\alpha} \quad (6.57)$$

Noticing that the derivatives of the polynomials along x will be 0 and injecting E_L in Eq. 6.53 and ?? allows to express the added mass force in x and y directions. If we express it using geometrical ratios $\frac{R}{y} = \frac{1}{F_1}$, $\frac{\dot{y}}{\dot{R}} = F_2$ and $\frac{\dot{y}}{\dot{R}} = F_3$, we can obtain:

$$F_{AM,x} = \rho_L V_b \left[\left(3\alpha_2 + \left(1 - \frac{F_2}{F_1} \right) \tilde{\alpha}_2 \right) \frac{\dot{R}}{R} U_{rel} - \alpha_2 \frac{\partial U_b}{\partial t} \right] \quad (6.58)$$

$$\begin{aligned} F_{AM,y} = -\rho_L V_b & \left[\left(3F_2\alpha + \frac{3}{2}\psi + \left(1 - \frac{F_2}{F_1} \right) F_2 \tilde{\alpha} + \left(1 - \frac{F_2}{F_1} \right) \frac{\tilde{\psi}}{2} + \frac{F_2}{F_1} \frac{\tilde{\alpha}}{2} + \frac{1}{F_1} \frac{\text{tr}(\tilde{\beta})}{2} + \frac{F_2}{F_1} \frac{\tilde{\psi}}{2} \right) \frac{\dot{R}^2}{R} \right. \\ & \left. + \left(F_3\alpha + \frac{\psi}{2} \right) \ddot{R} + \frac{1}{F_1} \frac{\tilde{\alpha}_2}{2} \frac{U_{rel}^2}{R} \right] \end{aligned} \quad (6.59)$$

In the case of a truncated sphere, $F_1 = \frac{y}{R} = \cos(\theta) = L_R$. If we suppose that the bubble keeps a nearly constant contact angle during its lifetime, we can further write $F_1 = F_2 = F_3 = \cos(\theta) = L_R$, which simplifies the forces in:

$$F_{AM,x} = \rho_L V_b \left[3\alpha_2 \frac{\dot{R}}{R} U_{rel} - \underbrace{\alpha_2}_{C_{AM,x}} \frac{\partial U_b}{\partial t} \right] \quad (6.60)$$

$$F_{AM,y} = \rho_L V_b \left[- \left(3 \underbrace{\left(L_R \alpha + \frac{\psi}{2} \right)}_{C_{AM,y1}} + \underbrace{\frac{\tilde{\alpha}}{2} + \frac{1}{L_R} \text{tr}(\tilde{\beta}) + \frac{\tilde{\psi}}{2}}_{C_{AM,y2}} \right) \frac{\dot{R}^2}{R} \right. \quad (6.61)$$

$$\left. - \underbrace{\left(L_R \alpha + \frac{\psi}{2} \right)}_{C_{AM,y1}} \ddot{R} + \underbrace{\frac{-1}{L_R} \frac{\alpha_2}{2} \frac{U_{rel}^2}{R}}_{C_{AM,y3}} \right] \quad (6.62)$$

On Figure 6.8, we plot the values of the added mass coefficients against the values of L_R .

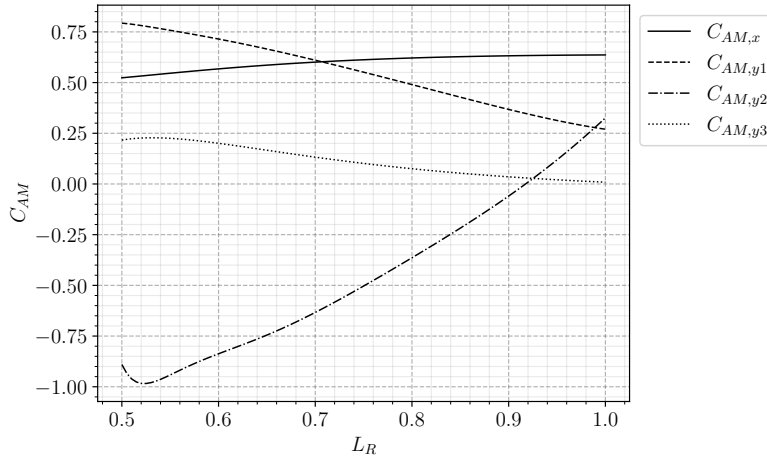


Figure 6.8: Values of the computed added mass coefficients in Eq. 6.60 and 6.62.

For the case of a spherical bubble laying on a wall ($L_R = 1$), we finally have:

$$F_{AM,x} = \rho_L V_b \left[3C_{AM,x} \frac{\dot{R}}{R} U_{rel} - C_{AM,x} \frac{\partial U_b}{\partial t} \right] \quad (6.63)$$

with $C_{AM,x} \approx 0.636$.

$$F_{AM,y} = \rho_L V_b \left[- (3C_{AM,y1} + C_{AM,y2}) \frac{\dot{R}^2}{R} - C_{AM,y1} \ddot{R} + C_{AM,y3} \frac{U_{rel}^2}{R} \right] \quad (6.64)$$

with $C_{AM,y1} \approx 0.27$, $C_{AM,y2} \approx 0.326$ and $C_{AM,y3} \approx 8.77 \times 10^{-3}$.

Parallel to the wall, the coupled term $\frac{\dot{R}}{R} U_{rel}$ in Eq. 6.63 promotes detachment and sliding of the bubble if $U_{rel} > 0$ e. g. if the bubble is attached to its nucleation site. This contradicts the aforementioned approach where solely projecting the RPE on both axes lead to an Added-Mass term related to bubble growth that only hinders the departure by sliding. Moreover, Eq. 6.64 exhibits a term induced by the relative velocity that acts as a lift force, which seems to rarely appear in other approaches.

Remark : The derived values of the added mass coefficients are only valid for $0.5 < L_R < 1$ as previously mentioned. When the bubble leaves the wall, added mass calculations of Duhar [12] would be more appropriate.

Those theoretical results highlight the importance of conducting a rigorous approach when possible to deriving those transient aspects of the force balance. Otherwise, some terms may be missing and lead to contradictory physical conclusions.

In the spirit of avoiding to introduce extra empirical terms, we keep the Added Mass force as presented in Eq. 6.63 and 6.64 and consider no projection along the inclination angle.

6.2.8 Force Balance Summary

Writing Newton's second law, we have the total force balance over the bubble in both directions:

$$\rho_V \frac{\partial V_b U_{b,x}}{\partial t} = -\pi R \sigma f_{C,x}(\theta, d\theta) + V_b (\rho_L - \rho_V) g + \frac{1}{2} C_D \rho_L \pi R^2 |U_L - U_b| (U_L - U_b) \\ + \rho_L V_b \left[3C_{AM,x} \frac{\dot{R}}{R} (U_L - U_b) - C_{AM,x} \frac{\partial U_b}{\partial t} \right] \quad (6.65)$$

$$\rho_V \frac{\partial V_b U_{b,y}}{\partial t} = -\pi R \sigma f_{C,y}(\theta, d\theta) + 2\pi R \sigma \sin(\theta)^2 + \frac{1}{2} C_L \rho_L \pi R^2 (U_L - U_b)^2 \\ + \rho_L V_b \left[-(3C_{AM,y1} + C_{AM,y2}) \frac{\dot{R}^2}{R} - C_{AM,y1} \dot{R} + C_{AM,y3} \frac{(U_L - U_b)^2}{R} \right] \quad (6.66)$$

Those force balances will respectively be used later to study the departure by sliding (along x) and the lift-off from the wall (along y).

On Table 6.2, we sum up some of the mentioned mechanistic approaches and their models along with the proposed force balance.

6.2.9 Liquid Velocity

To compute the liquid velocity and shear rate at bubble center height, we use the wall law of Reichardt [48], which describes the velocity profile from the viscous sublayer to the logarithmic region.

$$U_L^+ = \frac{1}{\kappa} \ln(1 + \kappa y^+) + c \left(1 - e^{-y^+/\chi} + \frac{y^+}{\chi} e^{-y^+/3} \right) \quad (6.67)$$

$$U_L = U_L^+ U_\tau$$

with $\kappa = 0.41$, $\chi = 11$ and $c = 7.8$.

$$\frac{\partial U_L^+}{\partial y^+} = \frac{1}{1 + \kappa y^+} + \frac{c}{\chi} \left(e^{-y^+/\chi} + \left(1 - \frac{y^+}{3} \right) e^{-y^+/3} \right) \quad (6.68)$$

$$\frac{\partial U_L}{\partial y} = \gamma = \frac{U_\tau^2}{\nu_L} \frac{\partial U_L^+}{\partial y^+}$$

The friction velocity is computed using Mac Adams correlation [38].

$$U_\tau = \sqrt{\frac{\tau_w}{\nu_L}} \quad (6.69)$$

$$\tau_w = 0.018 \text{ Re}_{D_h}^{-0.182} \frac{G_L^2}{\rho_L} \quad (6.70)$$

	Klausner (1993) [24]	Thorncroft (2001) [62]	Sugrue (2016) [58]
Forces	$\bar{F}_B = \frac{4}{3}\pi R^3 (\rho_L - \rho_V) \bar{g}$	$\frac{4}{3}\pi R^3 (\rho_L - \rho_V) \bar{g}$	$\frac{4}{3}\pi R^3 (\rho_L - \rho_V) \bar{g}$
	$\bar{F}_C = \text{Eq. ??, } r_w = 0.045 \text{ mm}$	$\text{Eq. ??, } r_w = R \sin(\theta_d)$	$\text{Eq. ??, } r_w = 0.025R$
	$\bar{F}_{CP} = \text{Eq. 6.16, } R_c = 5R$	Neglected	$\text{Eq. 6.16, } R_c = 5R$
	$C_D = \frac{16}{\text{Re}_b} \left[1 + \frac{3}{2} \left(\left(\frac{12}{\text{Re}_b} \right)^n + 0.796^n \right)^{1/n} \right], n = 0.65$	$C_D = \frac{16}{\text{Re}_b} \left[1 + \left(\frac{8}{\text{Re}_b} + \frac{1}{2} \left(1 + \frac{3.315}{\sqrt{\text{Re}_b}} \right) \right)^{-1} \right]$	$C_D = \frac{16}{\text{Re}_b} \left[1 + \frac{3}{2} \left(\left(\frac{12}{\text{Re}_b} \right)^n + 0.796^n \right)^{1/n} \right], n = 0.65$
	$\bar{F}_L = C_L = 2.74\sqrt{\text{Sr}}$ $\times \left[\text{Re}_b^{-2} + \left(0.24\sqrt{\text{Sr}} \right)^4 \right]^{\frac{1}{4}}$	$C_L = 0.71\sqrt{\text{Sr}}$ $\times \left[\left(\frac{1.15J(\varepsilon)}{\sqrt{\text{Re}_b}} \right)^2 + \left(\frac{3\sqrt{2\text{Sr}}}{8} \right)^2 \right]^{\frac{1}{2}}$	$C_L = 2.74\sqrt{\text{Sr}}$ $\times \left[\text{Re}_b^{-2} + \left(0.24\sqrt{\text{Sr}} \right)^4 \right]^{\frac{1}{4}}$
	$\bar{F}_{AM} = \frac{3}{2}\rho_L V_b \frac{\dot{R}}{R} U_L \bar{e}_x - \rho_L \pi R^2 \left(\frac{3}{2}\dot{R}^2 + R\ddot{R} \right)$ $\times (\cos(\theta_i) \bar{e}_y + \sin(\theta_i) \bar{e}_x), \theta_i = 10^\circ$	$2\pi\rho_L R^2 \dot{R} U_L \bar{e}_x - \rho_L \pi R^2 \left(\frac{3}{2}\dot{R}^2 + R\ddot{R} \right)$ $\times (\cos(\theta_i) \bar{e}_y + \sin(\theta_i) \bar{e}_x), \theta_i = 45^\circ$	$-\rho_L \pi R^2 \left(\frac{3}{2}\dot{R}^2 + R\ddot{R} \right)$ $\times (\cos(\theta_i) \bar{e}_y + \sin(\theta_i) \bar{e}_x), \theta_i = 10^\circ$
	Mazzocco (2018) [37]	Ren (2020) [49]	Present model
Forces	$\bar{F}_B = \frac{4}{3}\pi R^3 (\rho_L - \rho_V) \bar{g}$	$\frac{4}{3}\pi R^3 (\rho_L - \rho_V) \bar{g}$	$\frac{4}{3}\pi R^3 (\rho_L - \rho_V) \bar{g}$
	$\bar{F}_C = \text{Eq. ??, } r_w = R/15$	$\text{Eq. ??, } r_w = 0.2R$	$\text{Eq. ??, } r_w = R \sin(\theta)$
	$\bar{F}_{CP} = \text{Eq. 6.16, } R_c = 5R$	$\text{Eq. 6.16, } R_c = 5R$	$\text{Eq. 6.16, } R_c = R$
	$C_D = 1.13 \frac{24}{\text{Re}_b} \left(1 + 0.104 \text{Re}_b^{0.753} \right)$	$C_D = \frac{16}{\text{Re}_b} \left[1 + \frac{3}{2} \left(\left(\frac{12}{\text{Re}_b} \right)^n + 0.796^n \right)^{1/n} \right], n = 0.65$	$C_D = C_{D,U} (1 + \Delta C_D)$ $C_{D,U} \text{ by Eq. 6.29, } \Delta C_D \text{ by Eq. 6.31}$
	$\bar{F}_L = C_L = 2.61$	$C_L = 2.74\sqrt{\text{Sr}}$ $\times \left[\text{Re}_b^{-2} + \left(0.24\sqrt{\text{Sr}} \right)^4 \right]^{\frac{1}{4}}$	$C_L \text{ by Shi et al. [55]}$
	$\bar{F}_{AM} = -\frac{1}{4}\pi\rho_L K^4 (\cos(\theta_i) \bar{e}_y + \sin(\theta_i) \bar{e}_x),$ $\sin(\theta_i) = 0.2, \cos(\theta_i) = 1$	$-\rho_L \pi R^2 \left(\frac{3}{2}\dot{R}^2 + R\ddot{R} \right)$ $\times (\cos(\theta_i) \bar{e}_y + \sin(\theta_i) \bar{e}_x), \theta_i = 15^\circ$	$\frac{F_{AM,x}}{\rho_L V_b} = C_{AM,x} \left[3 \frac{\dot{R}}{R} U_{rel} - \frac{\partial U_b}{\partial t} \right],$ $C_{AM,x} = 0.636, F_{AM,y} \text{ by Eq. 6.64.}$

Table 6.2: Summary of different force-balance mechanistic approaches.

6.3 BUBBLE GROWTH

6.3.1 Introduction

In order to properly represent the bubble dynamics, it is mandatory to model the evolution of the bubble radius over time *i.e.* the bubble growth law. Since the bubble radius R and its derivatives \dot{R} and \ddot{R} appear in the force balance (notably in the expression of the added mass force 6.62), failing to predict the evolution of the bubble with time will definitely result in an erroneous force balance.

The problem of the bubble growth during its lifetime on the wall, including the sliding phase, is still an open question that aims to cover various types of heat transfer mechanisms. First, two growth regimes exist for a boiling bubble:

- Inertial growth, which occurs at the beginning of nucleation for low temperature difference between liquid and vapor. The evolution of the bubble size can be solved by the mass and momentum balances, through the solution of Rayleigh (1917) [47]. The form of the bubble growth is usually $R(t) = A \times t$ (Mikic & Rohsenow, [41]).
- Heat diffusion growth happening post the inertial phase. This type of bubble growth has been widely studied by different authors [41, 44, 54, 76] and is usually of the form $R(t) = B\sqrt{t}$, derivable using the energy balance around the bubble.

Those two regimes can be compared using the non-dimensional time t^+ defined as:

$$t^+ = \frac{A^2}{B^2} t \quad (6.71)$$

where

$$A = \sqrt{b \frac{h_{LV} \rho_V (T_L - T_V)}{\rho_L T_{sat}}} \text{ and } B = \sqrt{\frac{12}{\pi} \eta_L \text{Ja}} \quad (6.72)$$

with $b = \frac{2}{3}$ for a bubble in an infinite liquid medium and $b = \frac{\pi}{7}$ for a spherical bubble laying on a wall.

So that when $t^+ \ll 1$, $R(t) = At$ (inertial growth) and when $t^+ \gg 1$, $R(t) = B\sqrt{t}$ (heat diffusion growth). A general solution asymptotically covering the two regimes has been derived by Mikic & Rohsenow:

$$R^+ = \frac{2}{3} \left[(t^+ + 1)^{3/2} + t^{+3/2} - 1 \right], \quad R^+ = \frac{R}{B^2/A}, \quad t^+ = \frac{t}{B^2/A^2} \quad (6.73)$$

In most cases associated to wall nucleation and boiling flows, experimental observations showed that bubbles' lifetime is long enough to be mostly of heat conduction nature [28, 35, 75].

6.3.2 Heat Diffusion in Uniformly Superheated Liquid

The analytic derivation of a bubble growth law in a pure heat diffusion regime has been tackled by various authors, mostly for the case of a bubble in a uniformly superheated and quiescent liquid. An often referred solution is the work of Plesset & Zwick (1954) [44] who found an asymptotic solution for high values of Ja:

$$R(t) = \frac{2\sqrt{3}}{\sqrt{\pi}} \text{Ja} \sqrt{\eta_L t} \quad (6.74)$$

This result was generalized by Scriven (1959)[54] who derived:

$$R(t) = 2\mathcal{F}(\text{Ja}) \text{Ja} \sqrt{\eta_L t} \quad (6.75)$$

where \mathcal{F} is implicitly defined by assuming $\frac{\rho_L}{\rho_V} \gg 1$:

$$\mathcal{F}(\text{Ja}) = \frac{F}{2\text{Ja}^2}, \text{ and } \text{Ja} = F \exp\left(\frac{3}{2}F\right) \int_1^\infty \frac{1}{x^2} \exp\left(-\frac{F}{x} - \frac{F}{2}x^2\right) dx \quad (6.76)$$

which falls back to $\mathcal{F}(\text{Ja}) \rightarrow \frac{\sqrt{3}}{\sqrt{\pi}}$ when $\text{Ja} \gg 1$.

The general formulation of \mathcal{F} has been verified by Legendre *et al.* [30] with Direct Numerical Simulation of spherical bubble growth in a quiescent superheated liquid.

Usually, most authors are accepting $R(t) = K \text{Ja}_w \sqrt{\eta_L t}$ for the bubble growth. With K usually expressed as $K = \frac{2b}{\sqrt{\pi}}$ with b being used as an adjustable constant depending on the flow conditions and the fluid, or derived analytically as presented before ($b = \sqrt{3}$ [44], $b = \frac{\pi}{2}$ [15], $1 \leq b \leq \sqrt{3}$ [76], $b = 1.56$ [71], $b = 0.24$ [70], etc.).

When the bubble presents a relative velocity with the ambient liquid, the disturbance of the thermal boundary layer around the liquid-vapor interface will impact its growth. This phenomenon has been numerically studied by Legendre *et al.* [30] who found that the ratio between the growth rate \dot{R} and the relative velocity U_{rel} was controlling the growth regime as follows:

- If $\frac{\dot{R}}{U_{rel}} \gg 1$, the regime is close to the static heat diffusion and correspond to the Scriven formulation (Eq. 6.75);

- If $\frac{\dot{R}}{U_{rel}} \gg 1$, the relative velocity impacts the thermal boundary layer formation and leads to a growth matching the solution of Ruckenstein (1964) [50] where the Nusselt number is:

$$\text{Nu} = 2\sqrt{\frac{\text{Pe}(t)}{\pi}}, \quad \text{Pe}(t) = \text{Pr}_L \times \text{Re}_b(t) \quad (6.77)$$

In this case, the bubble growth is accelerated and $R \propto t^{2/3}$.

6.3.3 Microlayer Evaporation

In addition to the traditional heat diffusion from superheated liquid to the bubble through the liquid-vapor interface, bubble growth can also be enhanced by the evaporation of a so-called "microlayer". This term denotes a very thin layer of liquid (typically $\sim \mu\text{m}$ [28]) which is trapped between the heated wall and the bubble base, as shown on Figure 6.9. The existence of this microlayer has now been supported by both experimental visualizations [5, 6, 26, 28] and numerical investigations [3, 20, 65].

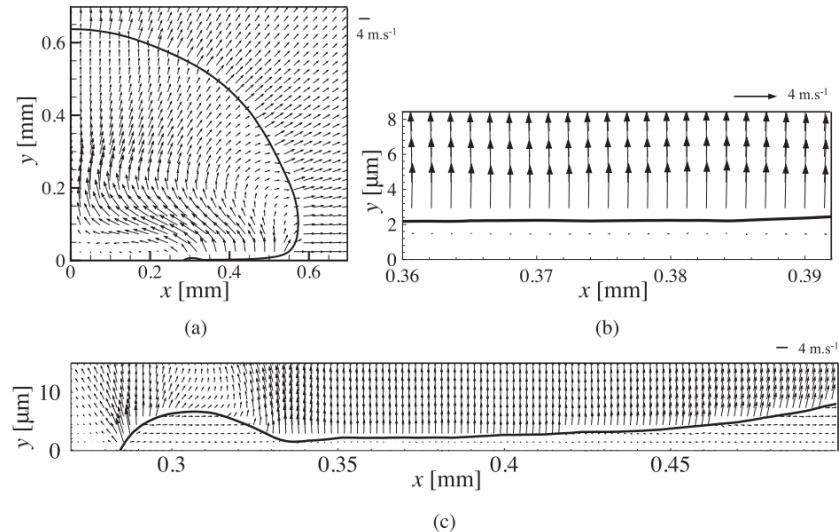


Figure 6.9: Microlayer appearing beneath the bubble in DNS conducted by and adapted from Urbano *et al.* [65].

Parallel to the heat diffusion approach, some authors computed the bubble growth by considering a pure microlayer evaporation regime. A well-known model of this type has been derived by Cooper & Lloyd in 1969 [8] and considers the wall thermal properties so that:

$$R(t) = 2.5 \frac{\text{Ja}}{\sqrt{\text{Pr}_L}} \sqrt{\eta_L t} \quad \text{if } \lambda_w \gg \lambda_L \quad (6.78)$$

$$R(t) = \frac{2}{\sqrt{\pi}} \sqrt{\frac{\lambda_w \rho_w c_{p,w}}{\lambda_L \rho_L c_{p,L}}} \quad \text{if } \lambda_w \ll \lambda_L \quad (6.79)$$

Remark : The parameter $\sqrt{\frac{\lambda_w \rho_w c_{p,w}}{\lambda_L \rho_L c_{p,L}}}$ that accounts for the wall properties is the same used in the correlation of Ünal for the maximum bubble diameter (Eq. 6.3).

The microlayer is also often taken into account for HFP modeling by enhancing the boiling heat flux through a computation of the microlayer volume [10, 27].

However, the presence of a liquid microlayer beneath the nucleated bubble is not assured for every boiling conditions. Indeed, experimental observations recently realized by Kossolapov [28] showed that the microlayer only existed for pressures below 3 bars when using water as working fluid. Moreover, Direct Numerical Simulations of Urbano *et al.* [65] where a full coupling between mass, momentum and

energy balance was achieved managed to detect whether if the bubble grows in a contact-line regime or if a microlayer appears. They proposed a criterion based on the capillary and Jakob numbers determining the formation of a microlayer :

$$\frac{\text{JaCa}}{(\theta - \theta_0)^3} > \frac{1}{A^3}, \quad \theta_0 = 5^\circ, \quad A = 313 \quad (6.80)$$

Remark : Computing the capillary number using $\dot{R} = \frac{K\text{Ja}}{2} \sqrt{\frac{\eta_L}{t}}$ as the interface velocity, we use Urbano *et al.* criterion to compute the time t_{max} after which the microlayer would cease to exist. Applying this to PWR conditions ($K = 1$, $\Delta T_w = 5K$) yields $t_{max} < 10^{-11}\text{s}$ for $6^\circ \leq \theta \leq 90^\circ$, meaning that there is no time during the bubble growth during which a microlayer could grow. This agrees with the observation that increasing pressure would lead to microlayer disappearance.

We will not further detail the study of the microlayer regime since its existence is very unlikely if not impossible in the pressurized conditions typical of a PWR.

6.3.4 Bubble Growth in Subcooled Flow Boiling

If we consider the full problem of bubble growth in subcooled flow boiling, the analytic expressions presented above may fall out of their validation range since extra physical phenomena will be at stake. This more generic type of growth lack of proper theoretical derivations due to the complexity of the considered system (turbulence, condensation, convection, etc.). That is why authors trying to represent such complex bubble growth often combine different heat transfer mechanisms such as:

- Evaporation due to conduction from the superheated liquid near the bubble base ;
- Evaporation of the liquid microlayer ;
- Condensation on top of the bubble when it reaches subcooled liquid ;
- Convective heat transfer due to relative velocity between the bubble and the liquid.

To our knowledge, such models always consider empirical or fitted parameters. For instance Yoo *et al.* [70] wrote for a sliding bubble:

$$\frac{\partial R}{\partial t} = \underbrace{\gamma \text{Pr}_L^{-0.5} \text{Ja}_w \sqrt{\frac{\eta_L}{t}} \frac{A_{ML}}{A_b}}_{\text{Microlayer}} + \underbrace{(1-f) \frac{b}{\sqrt{\pi}} \text{Ja}_w \sqrt{\frac{\eta_L}{t}}}_{\text{Superheated liquid}} - \underbrace{\frac{f \Delta T_L C}{1 - \rho_V / \rho_L} R}_{\text{Subcooled convection}} \quad (6.81)$$

where $\gamma = \sqrt{\frac{\lambda_w \rho_w c_{p,w}}{\lambda_L \rho_L c_{p,L}}}$, $\frac{A_{ML}}{A_b} = 1.22 \gamma^{-0.79} \exp(-0.204 \text{Ja}_w)$, $f = 0.5$, $b = 0.24$ and $C = 0.1$.

Their model was validated against low pressure sliding of boiling bubbles for different fluids (Water [35], FC87 [61], R113 [68]). They account for wall properties through the parameter γ in the microlayer term while assuming that 50% of the bubble faces subcooled liquid ($f = 0.5$) and condenses following the formulation of Levenspiel [32].

Zhou *et al.* [75] also proposed a similar modeling of the bubble growth, validated on their own measurements for boiling water at low pressure:

$$\begin{aligned} \frac{\partial R}{\partial t} = & \underbrace{\frac{1}{C} \text{Pr}_L^{-0.5} \text{Ja}_w \sqrt{\frac{\eta_L}{t}}}_{\text{Microlayer}} + \underbrace{\sqrt{\frac{3}{\pi}} \text{Ja}_T \sqrt{\frac{\eta_L}{t}} \min\left(\frac{y_{sat}}{2R}, 1\right)}_{\text{Superheated liquid}} \\ & - \underbrace{\frac{\eta_L}{2R} \text{Ja}_L (2 + 0.6 \text{Re}_b^{0.5} \text{Pr}_L^{0.3}) \max\left(\frac{H - y_{sat}}{2R}, 0\right)}_{\text{Subcooled convection}} \end{aligned} \quad (6.82)$$

where $C = 1.45$, Ja_T is the Jakob number taken at $\min(\bar{T} - T_{sat}, 0)$, \bar{T} the average liquid temperature around the bubble, $H = R(1 + \cos(\theta))$.

While they consider a constant coefficient for the microlayer evaporation, they propose a finer modeling of the condensation term by evaluating the height y_{sat} at which $T_L = T_{sat}$ using the turbulent wall law of Kader [22]. The condensation is modeled by the Ranz & Marshall correlation [46] that accounts for the relative velocity through the bubble Reynolds number.

Remark : As mentioned before, those model rely on numerous empirical parameters due to the variety of considered phenomena. In particular, microlayer evaporation is systematically considered which could be questioned regarding the observations made in Subsection 6.3.3.

Contrary to those models, Mazzocco *et al.* [37] propose to keep the radius as $K\text{Ja}_w\sqrt{\eta_L t}$ and to include subcooling and microlayer influence in the value of K :

$$K = \frac{1.243}{\sqrt{\text{Pr}_L}} + 1.945 * \chi, \quad \chi = 1 - B \frac{\Delta T_L}{\Delta T_w} \quad (6.83)$$

with $A = 0.05$ and $B = 1.55$ based on data-fitting.

Remark : This approach is interesting because it keeps the simple growth law in $t^{1/2}$ but the definition of χ is hardly general since it can lead to $K \leq 0$ for high values of $\frac{\Delta T_L}{\Delta T_w}$ which would be unphysical.

6.3.5 Analytic Approach of Bubble Growth in a Linear Thermal Boundary Layer

In this Subsection, we propose an analytic derivation of bubble growth for a truncated sphere laying on a wall in a boundary layer with a linear temperature profile. The considered geometrical and thermal definitions are depicted on Figure 6.10.

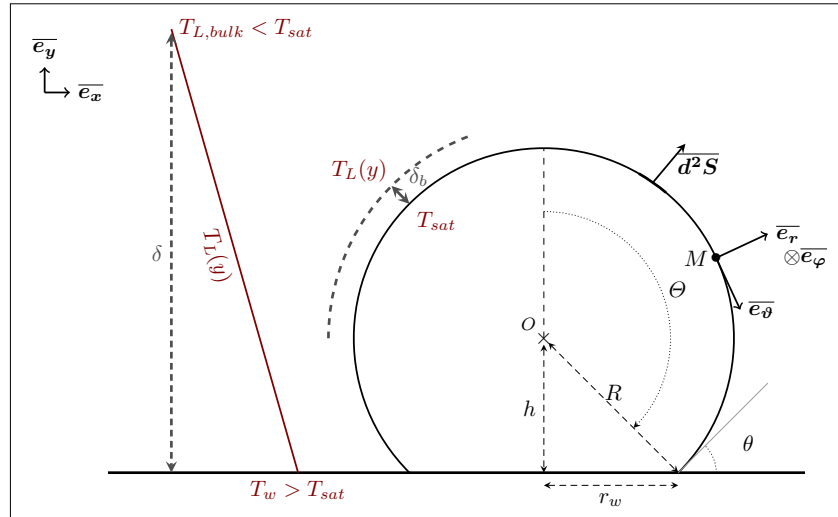


Figure 6.10: Studied geometry

We consider an established single-phase thermal boundary layer of thickness δ . When the bubble starts to grow, another boundary layer will of thickness δ_b grow between the liquid-vapor interface and the surrounding liquid which temperature depends on the wall distance y .

The liquid temperature is assumed to follow a linear profile:

$$T_L(y) = T_w + \frac{T_{L,bulk} - T_w}{\delta} y \quad (6.84)$$

Assuming that the vapor stays at a temperature close to T_{sat} , the radial component of the temperature gradient at the bubble's interface can be expressed as:

$$\bar{\nabla}(T) \cdot \bar{e_r} = \frac{\partial T}{\partial r}(R, \vartheta, \varphi) \approx \frac{T_L(y) - T_{sat}}{\delta_b} \quad (6.85)$$

Applying Fourier's law to the liquid close to the bubble to estimate the heat flux density vector $\bar{j_Q} = -\lambda_L \bar{\nabla}(T)$. Between t and $t + dt$ the heat exchanged through d^2S is:

$$d^2Q_b \approx -\frac{\lambda_L}{\delta_b} \left[\Delta T_w R^2 \sin(\vartheta) - \frac{\Delta T_w + \Delta T_L}{\delta} R^3 [\cos(\vartheta) - \cos(\Theta)] \sin(\theta) \right] d\vartheta d\varphi \quad (6.86)$$

Then assuming that δ_b is constant between t and $t + dt$, the total heat flux can be expressed by integrating over the bubble's surface:

$$Q_b = \frac{2\pi\lambda_L R^2}{\delta_b} (1 + \cos(\theta)) \left[\Delta T_w - \frac{R}{2\delta} (\Delta T_w + \Delta T_L) (1 + \cos(\theta)) \right] \quad (6.87)$$

Writing the mass balance by considering that the heat flux contributes solely to phase change:

$$\frac{\partial V_b}{\partial t} = \frac{Q_b}{\rho_V h_{LV}} \quad (6.88)$$

$$V_b = \frac{4}{3}\pi R^3 f_V, \quad f_V = \frac{1}{4}(2 - \cos(\theta))(1 + \cos(\theta))^2 \quad (6.89)$$

Writing this in terms of bubble radius:

$$\frac{\partial R}{\partial t} = \frac{\text{Ja}_w \eta_L}{2\delta_b f_V} (1 + \cos(\theta)) \left[1 - \frac{R}{2\delta} \left(1 + \frac{\text{Ja}_L}{\text{Ja}_w} \right) (1 + \cos(\theta)) \right] \quad (6.90)$$

Which reduces to the following differential equation:

$$\frac{\partial R}{\partial t} + aR = b \quad (6.91)$$

$$a = \frac{\text{Ja}_w \eta_L}{4\delta_b \delta f_V} \left(1 + \frac{\text{Ja}_L}{\text{Ja}_w} \right) (1 + \cos(\theta))^2 \quad \text{and} \quad b = \frac{\text{Ja}_w \eta_L}{2\delta_b f_V} (1 + \cos(\theta)) \quad (6.92)$$

Solutions of this differential equation depend on the hypothesis over δ and δ_b . If we assume that the bubble grows in a fully established liquid flow then δ can be considered as constant.

When the bubble will start to nucleate, the liquid-vapor interface will delimit a frontier through which a transient heat transfer between the vapor at constant temperature T_{sat} and liquid at $T_L(y)$ will occur. To estimate the associated local boundary layer thickness δ_b , we can rely on the solution of semi-infinite transient conduction as treated in Del Valle & Kenning [9] or Mikic & Rohsenow [41]:

$$\delta_b = \sqrt{\eta_L t} \quad (6.93)$$

The differential equation Eq. 6.91 becomes:

$$\frac{\partial R}{\partial t} + a(t)R = b(t) \quad (6.94)$$

$$a(t) = \frac{\text{Ja}_w \sqrt{\eta_L}}{4\delta f_V \sqrt{t}} \left(1 + \frac{\text{Ja}_L}{\text{Ja}_w} \right) (1 + \cos(\theta))^2 = K_a t^{-1/2} \quad (6.95)$$

$$b(t) = \frac{\text{Ja}_w \sqrt{\eta_L}}{2f_V \sqrt{t}} (1 + \cos(\theta)) = K_b t^{-1/2} \quad (6.96)$$

With the initial condition $R(t=0) = 0$, the solution to this differential equation is:

$$R(t) = R_\infty \left(1 - e^{-2K_a\sqrt{t}}\right) \quad (6.97)$$

$$R_\infty = \frac{K_b}{K_a} = \frac{2 \delta}{\left(1 + \frac{\text{Ja}_L}{\text{Ja}_w}\right)(1 + \cos(\theta))} \quad (6.98)$$

This type of bubble growth presents interesting properties. First, it degenerates to the uniformly superheated liquid solution when $t \rightarrow 0$:

$$R(t) \underset{t \rightarrow 0}{\sim} \frac{1 + \cos(\theta)}{f_V} \text{Ja}_w \sqrt{\eta_L t} \quad (6.99)$$

with a purely geometrical growth constant depending on the contact angle, equal to 2 for the spherical case.

Moreover, this growth law accounts for the liquid subcooling and thus presents an equilibrium radius R_∞ when $t \rightarrow \infty$, corresponding to the bubble size at which the vaporization from the superheated liquid is exactly compensated by the condensation at the bubble top.

To the best of our knowledge, this simple bubble growth law has never been proposed in the literature. However, this equation has some limitations :

- It requires the knowledge of the liquid thermal boundary layer thickness δ which estimation can be tricky ;
- This law can't be applied if $T_{L,bulk} > T_{sat}$.

Remark : It is worthy to note that this solution is derived solely using the energy balance at the liquid-vapor interface. No momentum balance was used when solving this physical problem, which can be considered as a limit of the approach.

6.3.6 Comparison with DNS Results

To assess the validity of Eq. 6.97, we will compare the radius time profile with DNS results by Urbano *et al.* [64] who simulated the same physical situation as depicted in Figure 6.10 for pool boiling. They also solved the heat conduction in the wall and studied the the growth dynamics depending on the values of ΔT_L and ΔT_w as well as the equilibrium diameter reached by the bubble.

In their analysis, Urbano *et al.* derived the same equilibrium radius as in Eq. 6.98 by equating the condensation and vaporization heat fluxes. By comparing with the equilibrium radius reached in their simulations, they found that a corrective factor $C = 1.15829$ was needed to correct Eq. 6.98. This difference could be explained by the heat conduction in the wall that is not accounted for in the theoretical approach.

DNS results obtained for three couples of subcooling ΔT_L and superheat ΔT_w are used for comparison. Results are displayed on Figure 6.11 with and without the corrective factor on R_∞ suggested by Urbano *et al.*

The analytical formulation of the bubble growth matches very well with the DNS results when the equilibrium radius is corrected. The different growth regime induced by the pairs $(\Delta T_L, \Delta T_w)$ are correctly captured by the model. DNS results present different equilibrium radius values when the subcooling and superheat changes, which can not be accounted for by the model.

Remark : Those results are encouraging and validate the modeling of δ_b with the semi-infinite conduction model (Eq. 6.93).

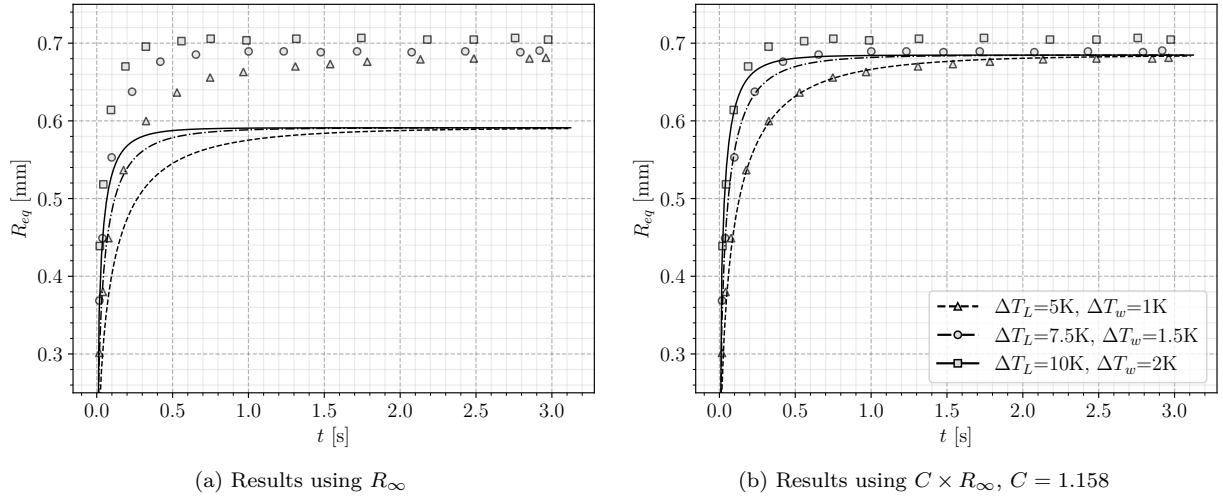


Figure 6.11: Comparison with DNS results of Urbano *et al.* [64] ($\delta = 3\text{mm}$ and $\theta = 50^\circ$).
Lines : Model predictions - Markers : DNS

6.3.7 Comparison with Experimental Measurements

6.3.7.1 Low Pressure Measurements

To further evaluate the proposed model, we compare the result with experimental measurements of bubble radius in vertical boiling of water at atmospheric pressure by Maity [35]. The choice of δ is adapted to each case and $\theta = 45^\circ$ is the average measured contact angle in the experiments.

In addition, we also plot the predictions by the heat diffusion solution $R = K J a_w \sqrt{\eta_L t}$ with $K = \frac{2b}{\sqrt{\pi}}$ and $1 \leq b \leq \sqrt{\pi}$. A solution with an optimized value of K is also represented. The models of Mazzocco and Yoo *et al.* are also compared. The results are presented on Figure 6.12.

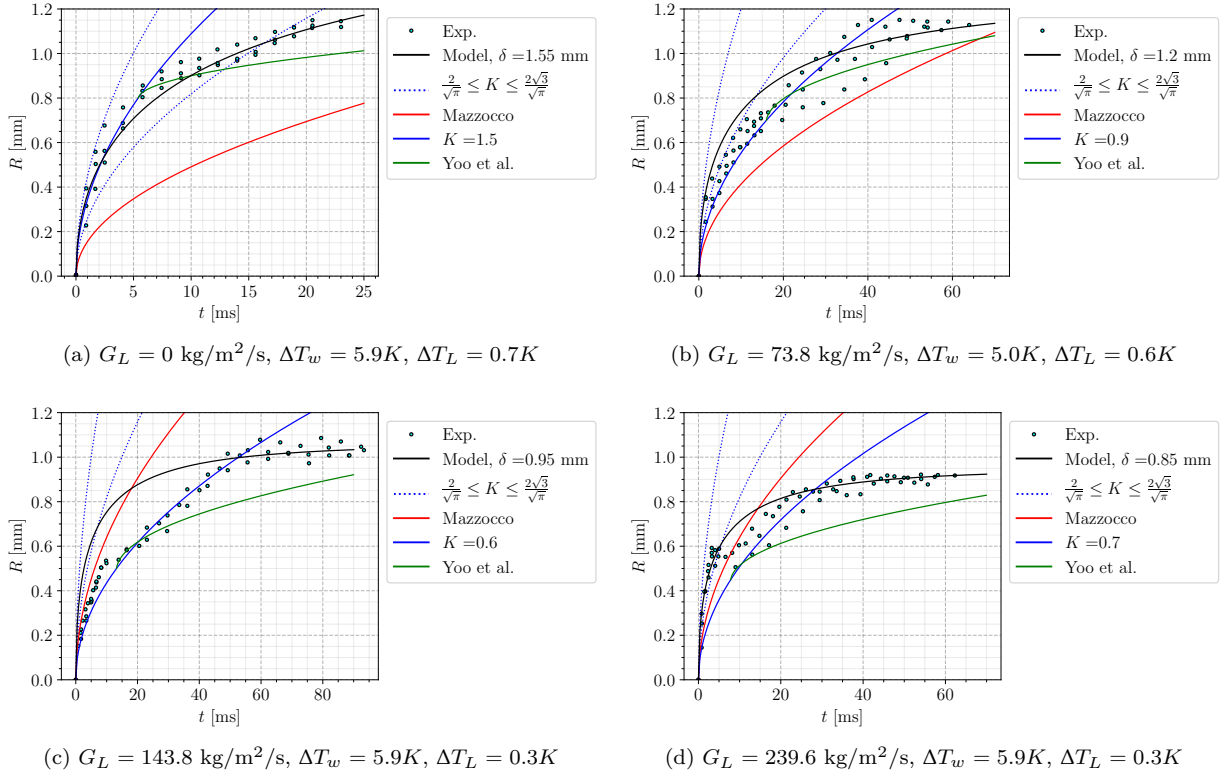


Figure 6.12: Comparison with experimental measurements of Maity [35].

The new formulation globally reproduces the experimental results better than the other models. In particular, the progressively damped growth rate when the bubble start to face colder liquid seems to correctly captures the nonlinear experimental growth. Values of δ needed to produce those results were between 0.85 mm and 1.55mm, which reasonably agrees with measurements of Maity in his experiment for horizontal flow giving δ roughly between 1 mm and 1.5 mm.

Remark : We can note that the optimal value of δ decreases as liquid mass flux increases, which is physically coherent as the thermal boundary layer will diminish in size with the Reynolds number.

On the other hand, the fitted value of K is often smaller than the lower bound $\frac{2}{\sqrt{\pi}}$ suggested by Zuber [76]. This is a consequence of the subcooled flow which deviates from the uniformly superheated liquid from which those values were derived. This fitted profile manages to capture some stages of bubble growth but can not predict the asymptotic behavior where bubble reaches a quasi-constant radius.

We see that the growth constant computed by Mazzocco *et al.* (Eq. 6.83) produce slightly better results compared to the analytic values of K but can lead to underestimations as for the pool boiling case.

Finally, we see that the model of Yoo *et al.* underestimates the bubble radius. We suspect this could come from the assumption considering that half of the bubble faces subcooled liquid ($f = 0.5$, Eq. 6.81), which is hardly reasonable especially at early growth stages.

6.3.7.2 High Pressure Measurements

The model is now compared to higher pressure measurement (20 bar and 40 bar) for water boiling by Kossolapov [28]. All the experiments are conducted with 10K of subcooling, and we take a contact angle of $\theta = 80^\circ$ (typical for water and ITO). The range of the measured diameters over time are represented since Kossolapov observed the growth of thousands of bubbles over the heater surface. Results are presented on Figure 6.13. We could not compare the model of Mazzocco because the formulation of Eq. 6.83 yielded negative growth constant.

The values of δ needed to match the experimental measurements using Eq. 6.97 are much smaller than the low pressure case, with $\delta \leq 0.1$ mm. The higher mass fluxes in Kossolapov measurements could explain lower values of δ , nevertheless they do not follow a particular trend with G_L .

Contrary to low pressure measurements, the Plesset & Zwick solution with $\frac{2}{\sqrt{\pi}} \leq K \leq \frac{2\sqrt{3}}{\sqrt{\pi}}$ provides an acceptable estimation of the bubble radius. This is probably due to the smaller bubble size in pressurized boiling (roughly 10 times smaller compared to atmospheric pressure).

Remark : The non-dimensional distances associated to the bubble radius $R^+ = \frac{R u_\tau}{\nu_L}$ rise up to 40 for Maity cases and 20 for Kossolapov cases while having way larger liquid mass fluxes. This supports the fact that bubbles at higher pressure are less likely to be impacted by subcooled liquid, spending most of their lifetime between the viscous and buffer layer.

6.3.8 Conclusions on Bubble Growth Modeling

- Recent experimental and numerical research have shown that the presence of a liquid microlayer contributing to the bubble growth strongly depends on the boiling conditions. In particular, disappearance of this microlayer at pressures higher than 3 bar have been observed by Kossolapov [28]. This microlayer should thus not be systematically taken into account.
- A new formulation derived from the heat diffusion in a linear temperature profile has been proposed (Eq. 6.97). Provided a correct value of the thermal boundary thickness δ , validation both on DNS and low pressure measurements shows that the model better captures the growth regime of bubbles in subcooled boiling compared to traditional models. However, this improvement appears limited at higher pressure when bubbles are smaller, where the Plesset & Zwick treatment also proposes an acceptable estimation of the bubble growth.

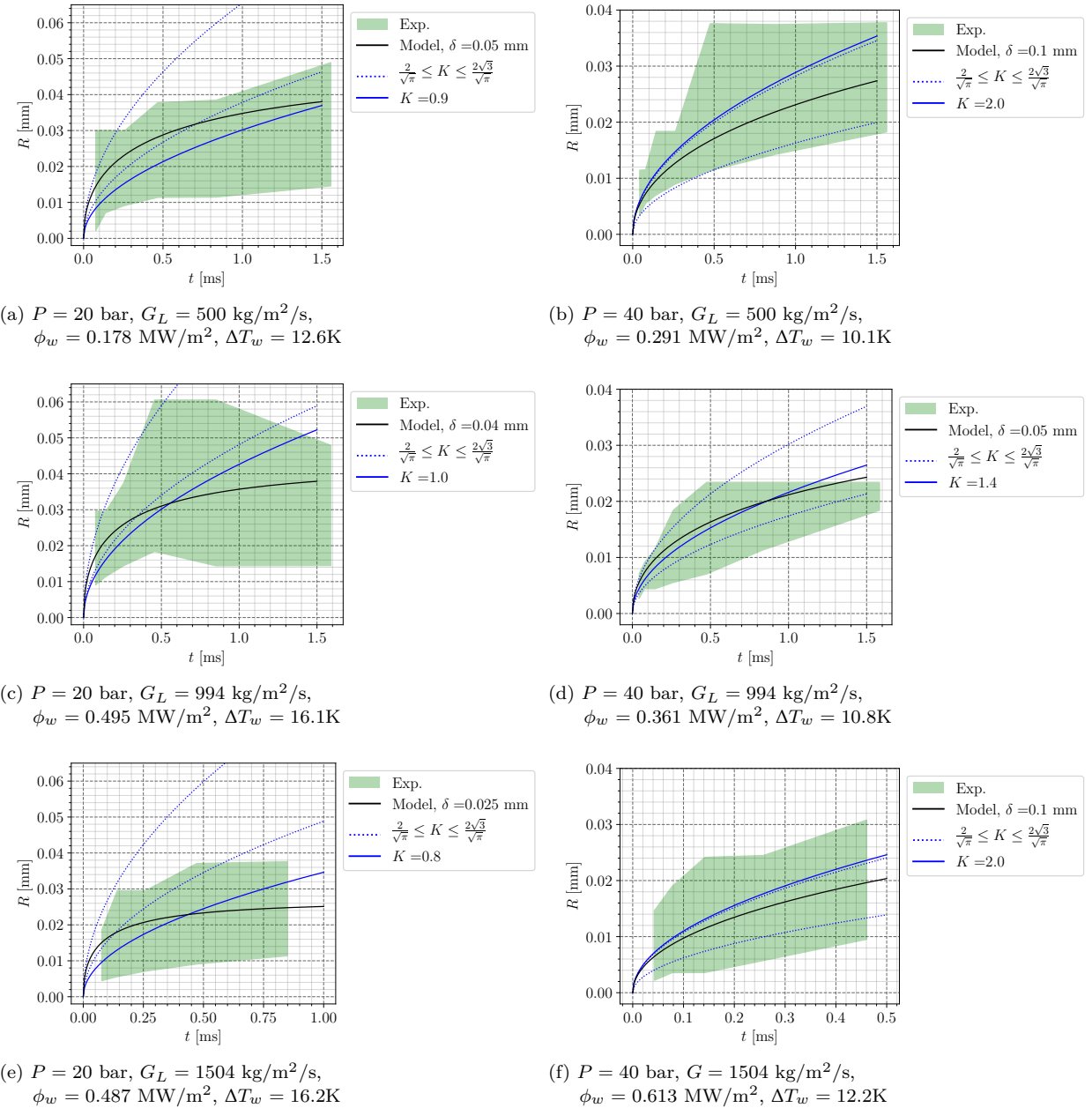


Figure 6.13: Comparison with experimental measurements of Kossolapov [28]. ΔT_w values are recalculated from analytical growth profiles fitted by the author.

- Mechanistic models that includes several heat transfer mechanisms require a certain number of empirical closures that limits the model generality, making them unsuitable for application to any boiling conditions.
- Whatever the conditions, a proper choice of the growth constant K in the $R = K \alpha_w \sqrt{\eta_L t}$ solution for a uniform liquid superheat can yield reasonable results. Moreover, it presents interesting mathematical properties such as the time independence of the products RR' and $R^3\ddot{R}$ that appear in the bubble force balance (Eq. 6.66).

All things considered, it seems that the proposed new growth law of Eq. 6.97 can be of greater interest for low pressure boiling where larger bubbles are more impacted by the bulk flow. Although it provides finer physical representation of bubble radius evolution, its application is limited by the estimation of δ to which the model is strongly sensitive. **On the other hand, less precise yet acceptable predictions of bubble growth are achieved using the $t^{1/2}$ law with a growth constant K close to unity.**

6.4 DEPARTURE BY SLIDING

The question of departure by sliding being central for bubble dynamics in vertical flow boiling, we will tackle the problem by starting with a non-dimensional analysis before moving to predictions of experimental measurements of departure diameters.

6.4.1 Non-Dimensional Analysis

To study the departure by sliding, we rely on force balance parallel to the wall (Eq. 6.65). Before departure, the bubble grows on its nucleation site while staying immobile, thus with a sliding velocity $U_b = \frac{\partial U_b}{\partial t} = 0$. The force balance parallel to the wall becomes:

$$-\pi R \sigma f_{C,x} + \frac{4}{3} \pi R^3 (\rho_L - \rho_V) g + \frac{1}{2} C_D \rho_L \pi R^2 U_L^2 + \frac{4}{3} \pi R^3 \rho_L 3 C_{AM,x} \frac{\dot{R}}{R} U_L = 0 \quad (6.100)$$

We can note that in this equation, departure by sliding is promoted by the buoyancy, the drag and the added mass forces. Only the capillary force keeps the bubble attached to its nucleation site, which will be discussed later. As discussed in the previous section, the bubble growth is modeled as:

$$R(t) = K \text{Ja}_w \sqrt{\eta_L t} \quad (6.101)$$

with K as an adjustable constant.

Re-writing Eq. 6.100 in non-dimensional form by dividing the LHS by the added mass force yields:

$$-\frac{1}{2} \frac{f_{C,x}}{K^2 C_{AM,x}} \frac{1}{\text{Ca}} \frac{\text{Pr}_L}{\text{Ja}_w^2} + \frac{1}{3} \frac{1}{K^2 C_{AM,x}} \frac{\text{Re}_b}{\text{Fr}} \frac{\text{Pr}_L}{\text{Ja}_w^2} + \frac{1}{8} \frac{C_D}{K^2 C_{AM,x}} \text{Re}_b \frac{\text{Pr}_L}{\text{Ja}_w^2} + 1 = 0 \quad (6.102)$$

where we have the following non-dimensional numbers:

$$\begin{aligned} \text{Re}_b &= \frac{2 R U_L}{\nu_L} ; \text{Fr} = \frac{\rho_L U_L^2}{(\rho_L - \rho_V) g R} ; \text{We} = \frac{\rho_L U_L^2 R}{\sigma} ; \text{Eo} = \frac{(\rho_L - \rho_V) g R^2}{\sigma} ; \\ \text{Ja}_w &= \frac{(T_w - T_{sat}) \rho_L c_{P,L}}{\rho_V h_{LV}} ; \text{Pr}_L = \frac{\nu_L}{\eta_L} ; \frac{\dot{R}}{U_L} = \frac{K^2 \text{Ja}_w^2}{\text{Pr}_L \text{Re}_b} ; \text{Ca} = \frac{\mu_L U_L}{\sigma} \end{aligned}$$

Eq. 6.102 exhibits terms that can be used to compare the magnitude of each detaching forces and obtain the following conditions:

$$\text{Added mass force greater than drag if: } \frac{\text{Ja}_w^2}{\text{Pr}_L} > \frac{1}{8} \frac{C_D}{C_{AM,x}} \frac{1}{K^2} \text{Re}_b \quad (6.103)$$

$$\text{Added mass greater than buoyancy if: } \frac{\text{Ja}_w^2}{\text{Pr}_L} > \frac{1}{3} \frac{1}{C_{AM,x} K^2} \frac{\text{Re}_b}{\text{Fr}} \quad (6.104)$$

$$\text{Drag greater than buoyancy if: } \text{Re}_b > \frac{16}{3} \frac{1}{C_D} \frac{\text{Eo}}{\text{Ca}} = \text{Re}_c \quad (6.105)$$

Those three conditions can be seen as boundaries in a $(\text{Ja}_w^2 / \text{Pr}_L ; \text{Re}_b)$ plane. With a given fluid and bubble diameter $D = 2R$, we can represent the different regimes of force dominance by plotting those three boundaries simultaneously on a regime map. An example of such a map is presented on Figure 6.14. This allows to visualize the operating conditions under which each of the detaching forces will be dominant. Logically, buoyancy dominates for low Re_b regimes contrary to drag. Added mass dominates when values of $\text{Ja}_w^2 / \text{Pr}_L$ are high *i.e.* when bubble grows rapidly.

6.4.1.1 Influence of Pressure

On Figure 6.15, we draw the regime map for 3 different pressures and associated orders of magnitude of bubble departure diameter [25].

The impact of pressure is mostly seen through the decrease of bubble departure diameter. As pressure increases, buoyancy force decreases while drag and added mass forces display much larger dominance zones. The competition between those two terms mainly relies on the competition between liquid flow velocity and wall superheat or heat flux.

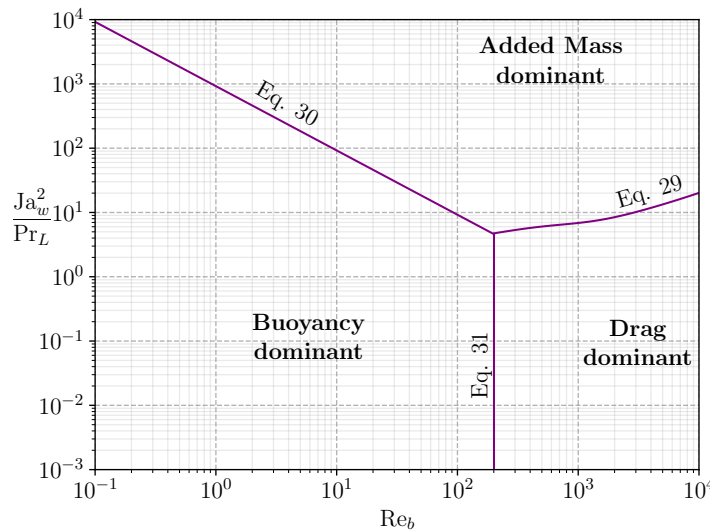


Figure 6.14: Regime map regarding departure by sliding. Boundaries plotted for water at 1 bar and $D_d = 0.5\text{mm}$. ($K = 2$)

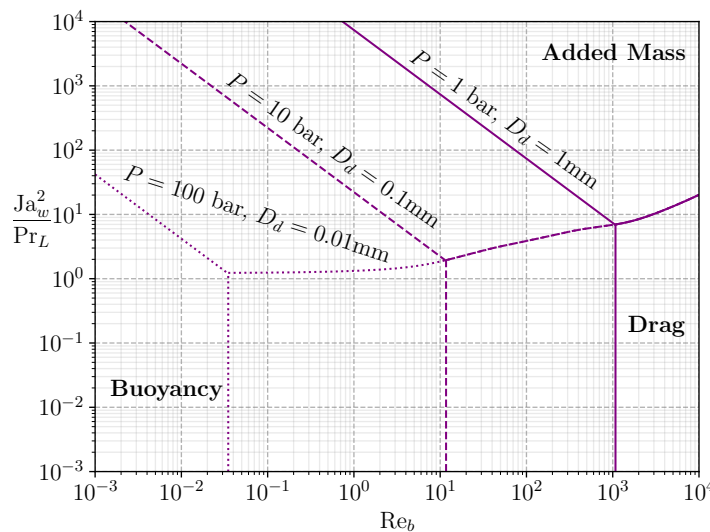


Figure 6.15: Regime map plotted for water at different pressures and bubble departure diameters. ($K = 2$)

6.4.1.2 Comparison between Fluids

On Figure 6.16, we compare the dominance zones for R12 at 26 bar and water at 155 bar. Moderately pressurized R12 (10 to 30 bar) has often been used as a simulating fluid to mimic water in PWR since it has the same density ratio and Weber number for instance (see Section ?? related to the DEBORA experiments).

Assuming that the conservation of Weber and Boiling numbers may lead to similar bubble departure diameters, we can observe that the boundaries between the two fluids are very close. This qualitatively indicates that R12 shall present bubble departure by sliding mechanisms similar to what happens in PWR.

Remark : This approach could easily be applied to comfort the confidence one may have in extrapolating the observations done using a simulating fluid to industrial applications.

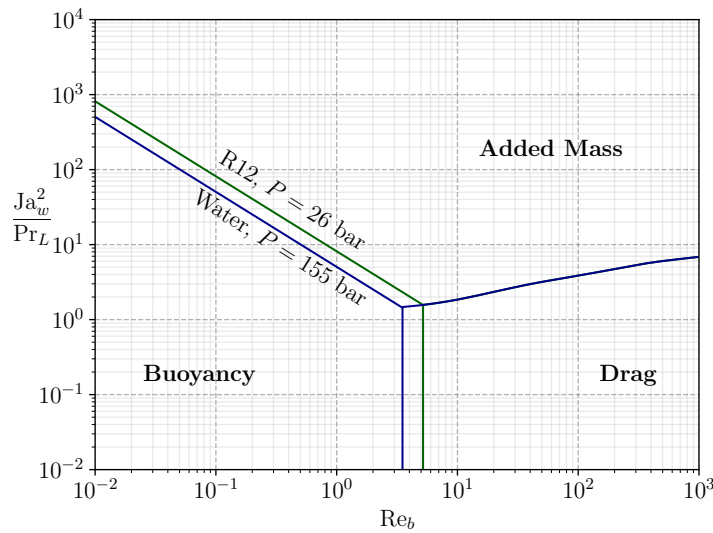


Figure 6.16: Regime map for R12 as simulating fluid for PWR. $D_d = 0.05\text{mm}$ is chosen according to R12 measurements from Garnier *et al.* [17] who observed bubbles of $\sim 0.1\text{mm}$ diameter after lift-off. The same value is taken for water. ($K = 2$)

6.4.2 Application to Experimental Data

Now we want to apply this non-dimensional approach to experimental measurement in order to determine the actual bubble departure by sliding regimes. We rely on 7 experiments in which bubble departure diameters in vertical flow boiling were measured. The operating conditions are gathered in Table 6.3.

Author	Fluid	D_h [mm]	P [bar]	G_L [$\text{kg}/\text{m}^2/\text{s}$]	ΔT_L [K]	ϕ_w [kW/m^2]	ΔT_w [K]	D_d [mm] (N_{mes})
Thornicroft [61] (1998)	FC-87	12.7	N.A.	0 - 319	0.99 - 3.27	2.83 - 11.8	0.54 - 6.89	0.094 - 0.237 (10)
Maity [35] (2000)	Water	20	1.01	0 - 239.6	0.3 - 0.7	N.A.	5 - 5.9	0.788 - 1.71 (9)
Chen [4] (2012)	Water	3.8	1.2 - 3.35	214 - 702	14.5 - 30.3	83.6 - 334	N.A.	0.549 - 2.255 (22)
Sugrue [58] (2014)	Water	16.6	1.01	250 - 400	10 - 20	50 - 100	2 - 6	0.229 - 0.391 (16)
Guan [19] (2014)	Water	9	1.01	87.3 - 319.2	8.5 - 10.5	68.2 - 104	4.5 - 8.5	0.62 - 1.85 (12)
Ren [49] (2020)	Water	3.8	2 - 5.5	488.4 - 1654	28.7 - 51	160.7 - 643.2	N.A.	0.045 - 0.111 (42)
Kossolapov [28] (2021)	Water	11.8	19.9 - 39.8	500 - 1500	10	178 - 613	10.1 - 16.2	0.01 - 0.047 (11)

Table 6.3: Bubble departure diameters data sets in vertical flow boiling

If the value of ΔT_w is not available in the considered data-set, we estimate it ΔT_w using Frost & Dzakowic correlation [16].

$$\Delta T_w = \Pr_{L,sat} \sqrt{\frac{8\sigma\phi_w T_{sat}}{\lambda_L \rho_V h_{LV}}} \quad (6.106)$$

To place experimental measurements on the non-dimensional map, we need a bubble detachment diameter value D_d to plot the dominance zones. Since measured D_d vary significantly in each experiment, we draw the boundaries for the maximum and minimum values of D_d as shown on Figure 6.17a. If the considered

data covers different pressures, boundaries for each pressure are plotted to exhibit its impact (Figures 6.17d, 6.17e and 6.17f). We chose a value of $K = 1$ to draw the boundaries.

The Figure 6.17 shows that for most of the low pressure experiments, the detaching forces are the added mass and the buoyancy. Smaller bubbles are mainly detached under the effect of the added mass force (Figures 6.17c, 6.17d and 6.17e). When the bubbles detach at higher diameters, the impact of the buoyancy force naturally increases and is comparable to the added mass force (Figures 6.17a and 6.17b).

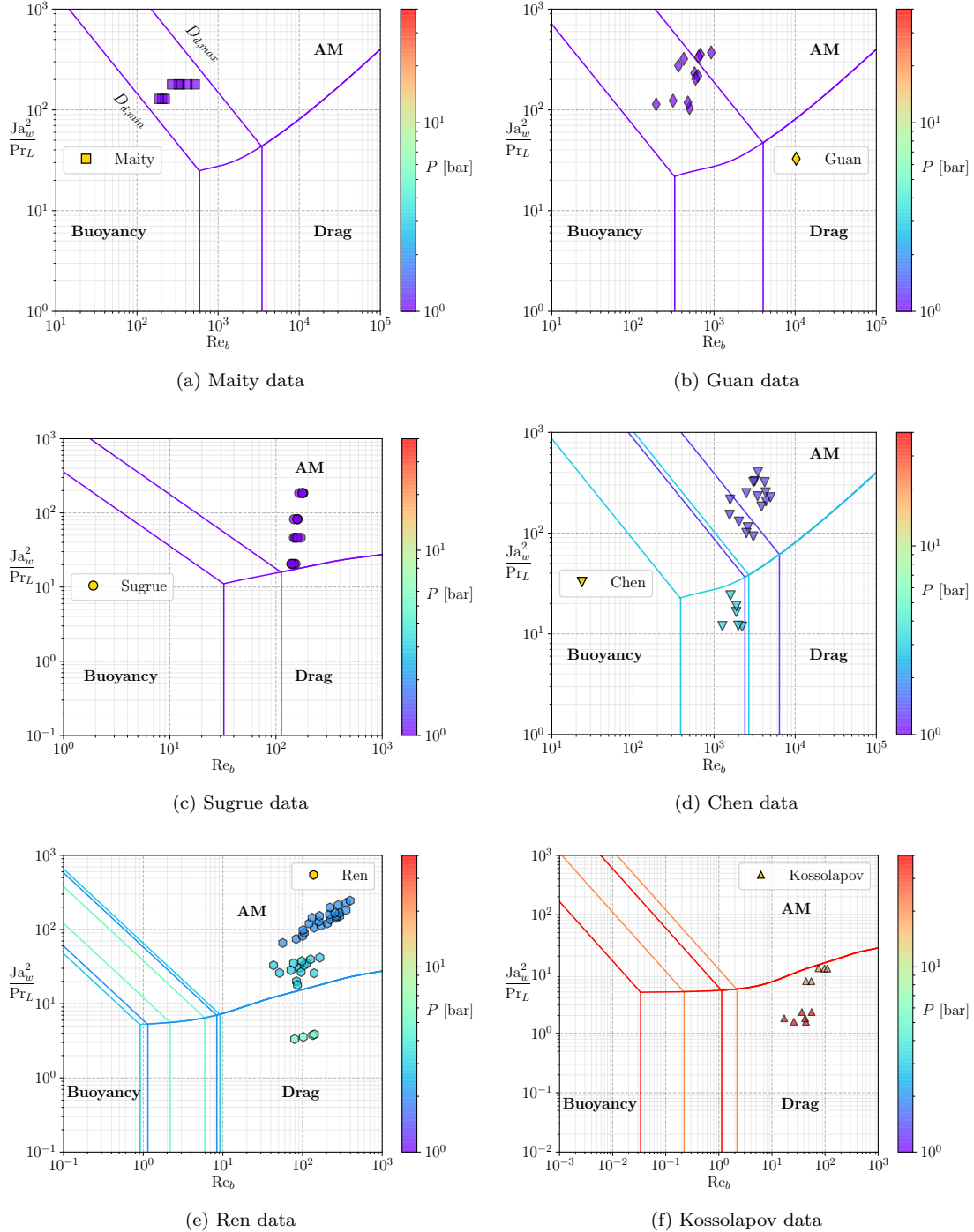


Figure 6.17: Regime maps for each water data sets from Table ??.

When the pressure increases, we observe that the experimental measurements gradually move towards the drag dominant zone as seen on Figures 6.17e and 6.17f. This main difference in the dynamic regime when bubble departs by sliding arises from multiple effects:

- The decrease of ρ_L/ρ_V with pressure, thus reducing Ja_w and the impact of the detaching added mass term ;
- The higher liquid mass fluxes in Kossolapov experiments, increasing the impact of the drag ;
- The decrease of D_d with pressure, reducing the magnitude of buoyancy.

However, we see that some measurements lie close to the added mass / drag boundary (Figure 6.17f), indicating that the added mass force still plays a significant role for bubble detachment. This means that regardless of the operating pressure, the detaching term associated to the coupling between bubble growth and outer liquid flow should not be neglected in the force balance (Eq. 6.100).

6.4.3 Departure Diameter Prediction

6.4.3.1 About the Use of Empiricism

As previously mentioned, the case of bubble detachment in vertical flow boiling is particular since only one force maintains the bubble attached to its nucleation site: the capillary force (Eq. 6.100). Its expression depends on the contact angle θ , the angle half-hysteresis $d\theta$ and the bubble foot radius r_w (or ratio to bubble diameter r_w/R) and is thus very sensitive to those values.

Paradoxically, those terms are among the least precisely known due to the difficulty of measurement and associated uncertainties. For instance, conducting precise evaluations of the contact angle near the bubble base through optical techniques can be challenging because of the strong temperature gradients close to the heated surface.

Consequently, empirical choices have to be made in order to set a value to those parameters, often by relying on data-fitting or approximate measurements in other conditions. For instance, contact angles are often taken as arbitrary average values [49] or measurements in room conditions [58] and applied over a whole set of experiments. This is questionable since contact angle is unlikely to remain unchanged over different operating conditions and surfaces with varying roughness and properties [57].

However, no better information except those given by the authors can be used to evaluate the capillary force since no generic model exist to compute the contact angle and hysteresis. In this work, admitting a significant uncertainty (typically 5° , as in Guan [19]), we will use the following values for the contact angles :

- $\theta_u = 25.3^\circ$ and $\theta_d = 6.6^\circ$ for Thorncroft data (measured values for FC-87 on nichrome [62]) ;
- $\theta_u = 50^\circ$ and $\theta_d = 40^\circ$ for Maity data (measured average contact angles for each bubble during its lifetime [35]) ;
- $\theta_u = 130^\circ$ and $\theta_d = 65^\circ$ for Chen data (chosen values in their study following measurements for water on stainless steel at high temperature by Kandlikar *et al.* [23]) ;
- $\theta_u = 91^\circ$ and $\theta_d = 8^\circ$ for Sugrue data (measured values at room temperature [60]) ;
- $\theta_u = 75^\circ$ and $\theta_d = 30^\circ$ for Guan data (measured average value through experimental visualizations [19]) ;
- $\theta_u = 45^\circ$ and $\theta_d = 36^\circ$ for Ren data (chosen values in their study [49]) ;
- $\theta = 80^\circ$ for Kossolapov data (typical contact angle for water on ITO [28]) and $d\theta = 1^\circ$ assuming that the very small bubbles at high pressure are nearly not tilted.

Similarly, the bubble foot radius r_w is often empirically assumed to be either constant [24] proportional to the bubble radius [37, 58] or to follow a linear or logarithmic law of R [19, 75]. That is why we chose to use the truncated sphere hypothesis (Eq. 6.14) to compute r_w using R and θ .

Finally, we would like to acknowledge that the empiricism to evaluate those parameters represents one of the biggest flaws of the force-balance approach. Indeed, such a model aims to detect small sign changes in a sum of a few μN of forces that are decades larger as pointed out by Bucci *et al.* [2]. Mechanistic models are thus strongly sensitive to any extra parameter included in the modeling of the forces.

6.4.3.2 Growth Constant Value

As discussed in Section 6.3, the growth constant K with a value close to one or lower usually provides reasonable approximation of the bubble radius. In particular, subcooled flow boiling may need smaller values of K , as well as fluids with high Prandtl numbers.

To avoid a systematic overestimation of the added mass term which could lead to strong underestimations of the departure diameter in cases that would present strong subcoolings, liquid velocity or working fluids with low thermal conductivity, we will use:

$$K = \frac{2b}{\sqrt{\pi}}, \quad b = 0.24 \quad (6.107)$$

as proposed by Yoo *et al.* [70] to model the superheated liquid diffusion growth term.

6.4.3.3 Predictions

We consider the non-dimensional force balance before departure.

$$C_{AM,x} K^2 \frac{Ja_w^2}{Pr_L} + \frac{1}{3} \frac{Re_b}{Fr} + \frac{1}{8} C_D Re_b = \frac{1}{2} \frac{f_{C,x}}{Ca} \quad (6.108)$$

Since we only have the capillary term hindering departure as a first approach, we can suppose that departure is reached when:

$$C_{AM,x} K^2 \frac{Ja_w^2}{Pr_L} + \frac{1}{3} \frac{Re_b}{Fr} + \frac{1}{8} C_D Re_b > \frac{1}{2} \frac{f_{C,x}}{Ca} \quad (6.109)$$

which is similar to considering that the other forces overcome the capillary force.

On Figure 6.18, we show the predictions obtained with the proposed modeling and those obtained with Mazzocco's recent model [37].

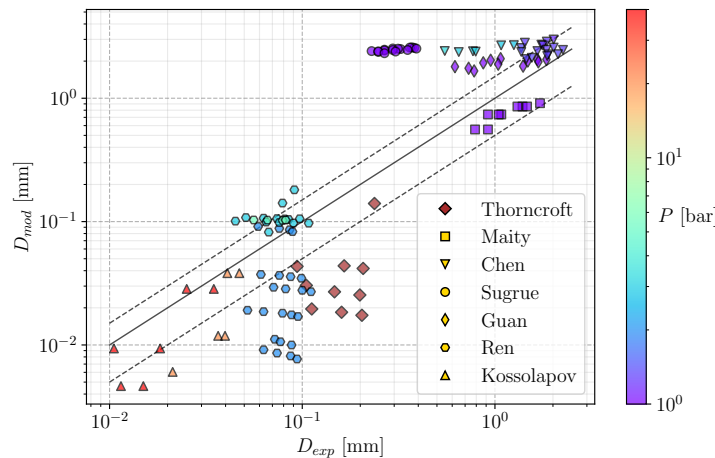
The model have an acceptable trend on some experimental sets, but strong overestimation occur on the cases of Sugrue. Moreover, we observe significant underestimations on the data of Ren at 2 bar and Thorncroft.

Mazzocco's model provides a good accuracy on the data of Sugrue, Guan, Maity and Ren (2 bar). However, we observe very large overestimation over Thorncroft's measurements and significant underestimation on Chen, Ren (3 and 5 bar) and Kossolapov measurements.

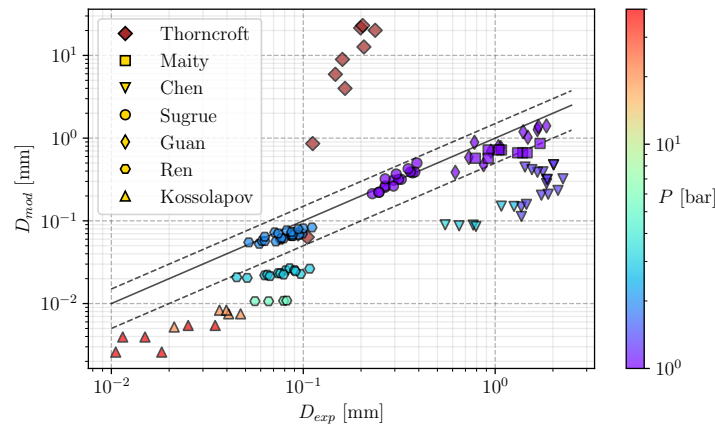
6.4.4 Discussion and accounting for parameters uncertainties

The aforementioned errors observed for the proposed model may originate from various reasons:

- The contact angle proposed for Sugrue cases is high with a large hysteresis, suggesting strongly deformed and flattened bubbles under the truncated sphere hypothesis. Based on images from Sugrue's work [59], a comparison between a real bubble with the assumed shape is presented on Figure 6.19. This shows a huge difference which indicates that the contact angle and hysteresis values may be overestimated. Using the available images, the ratio of the bubble diameter to the apparent bubble foot would lead to an average contact angle $\theta \approx 20^\circ$ for a truncated sphere. Noting that a larger inclination is observed for the bubbles under higher mass fluxes leads us to suppose a value $d\theta \approx 15^\circ$. This represent a similar inclination to contact angle ratio ($d\theta/\theta$) compared to the initially proposed values. The resulting new shape is also presented on Figure 6.19 and seem to better represent the actual bubble.
- For cases where limited under and overestimation is observed, we may allow to account for an uncertainty as high as 5° for the average contact angle θ and half-hysteresis $d\theta$.
- As mentioned earlier, applying the same contact angle and hysteresis over a wide range of measurements is a strong assumption, especially for cases where different pressures and bubble diameter variations are observed. Thus, we may slightly distinguish the applied values of θ and $d\theta$ for different pressures within a given experiment, keeping a change no larger than 5° .



(a) Proposed model without accounting for contact angle uncertainties



(b) Mazzocco model

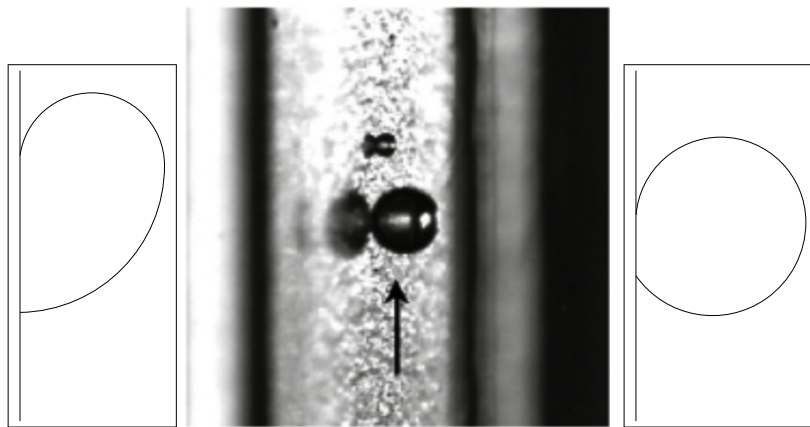
Figure 6.18: Predicted bubble departure diameters. $\pm 50\%$ error bars are indicated.

Figure 6.19: Initially assumed, real and reassessed bubble shape for Sugrue cases (picture adapted from [59]).

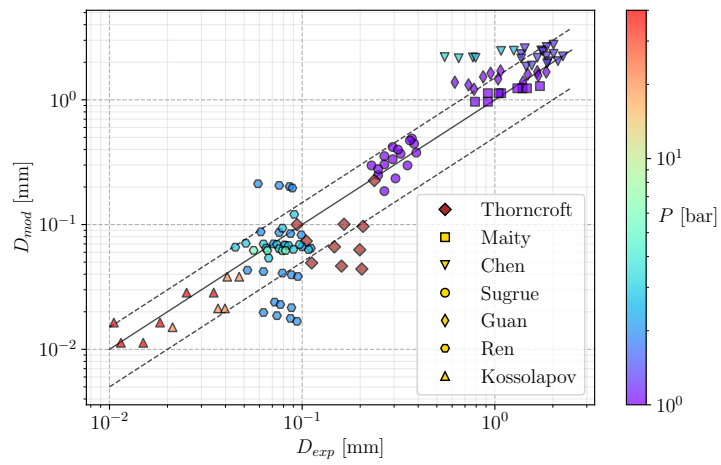
- Kossolapov cases at $G_L = 500 \text{ kg/m}^2/\text{s}$ are better predicted. Cases under higher mass fluxes (1000 and 1500 $\text{kg/m}^2/\text{s}$) present underestimation that could come from the value of $d\theta$. At such mass fluxes, the Weber number can be up to a decade higher and bubbles may thus accept a larger inclination before detachment.
- Cases of Ren and Chen rely on chosen values for θ and $d\theta$ and not on measured ones. They are therefore subject to strong uncertainties. We can note that the values for Chen cases are significantly high.

- The proposed growth law is still rather simple and may miss significant information, especially regarding bubble size and fluid properties such as the Prandtl number.
- Errors on Thorncroft cases may be linked to uncertainties regarding FC-87 properties. Indeed, we use the values given at $T_{sat} = 29^\circ$ at 1 bar in his work [61]. However, the saturation temperature indicated in his test matrix is close to 40° which means that measurements were conducted at a higher pressure, for which we do not have FC-87 properties.

Therefore, using modified values of θ and $d\theta$ among experimental data sets with no more than a 5° change (except for Sugrue cases reassessed values) leads to predictions on Figure 6.20.

Author	θ [°]	$d\theta$ [°]
Thorncroft	21	14
Maity	45	10
Chen	92.5	27.5
Sugrue	20	15
Guan	47.5	17.5
Ren (2 bar)	45.5	7.5
Ren (3 bar)	37.5	3.5
Ren (5 bar)	35.5	3.5
Koss. (500 kg/m ² /s)	80	0.5
Koss. (1000 kg/m ² /s)	80	1
Koss. (1500 kg/m ² /s)	80	1.5

(a) Modified contact angle and hysteresis values.



(b) Predicted bubble departure diameters.

Figure 6.20: Proposed model performance while accounting for contact angle uncertainties

The predictive capacity of the model is significantly enhanced, especially on Sugrue's cases which tends to indicate that the contact angle reassessment was justified under the truncated sphere hypothesis. Table 6.4 summarizes the average errors obtained with the present model and Mazzocco's one.

The proposed model achieves an overall better predictive capability even when excluding measurements from Thorncroft on which Mazzocco's model strongly overestimates the departure diameter. Mazzocco's model is still better on Sugrue and Guan cases since it was built and validated using those measurements. It better predicts results from Ren but only for the 2 bar cases while it underestimates the departure diameter for higher pressures. Those results are a coupled effect of his optimized growth law along with the imposed value of r_w/R and the use of the inclination angle to hinder departure as mentioned in 6.2.7.

The approach demonstrated the importance and the strong influence of the contact angle and hysteresis. A small change of their value (staying in the uncertainty range of 5°) allowed to reach reasonable predictions over a large range of bubble departure diameters with the proposed model, using a reduced number of empirical parameters.

Author	Mazzocco	Present model
Thorncroft	4874%	46.2%
Maity	39.7%	13.8%
Chen	83.8%	73.6%
Sugrue	9.73%	21%
Guan	25.5%	44.5%
Ren	40.32%	47%
Kossolapov	78.3%	24.2%
Total (without Thorncroft)	46.58%	43.3%

Table 6.4: Average relative error reached by the models.

6.5 SLIDING PHASE

6.5.1 Modeling

After departure, bubbles slide over a distance l_{sl} which scales the impact of the sliding phenomenon over the wall heat transfer. Achieving good prediction of bubble sliding velocity is then important if one wishes to correctly quantify its impact. Following the force balance framework presented in Section 6.2, we can write Newton's second law parallel to the wall for the sliding bubble.

$$\rho_V \frac{d(V_b U_b)}{dt} = -\pi R \sigma f_{C,x} + \frac{4}{3} \pi R^3 (\rho_L - \rho_V) g + \frac{1}{2} C_D \rho_L \pi R^2 U_L^2 + \frac{4}{3} \pi R^3 \rho_L \left[3C_{AM,x} \frac{\dot{R}}{R} U_{rel} - C_{AM,x} \frac{dU_b}{dt} \right] \quad (6.110)$$

This equation can be re-written to express the bubble acceleration.

$$\left(1 + \frac{\rho_L}{\rho_V} C_{AM,x} \right) \frac{dU_b}{dt} = \left(\frac{\rho_L}{\rho_V} - 1 \right) g + \frac{3}{8} \frac{C_D}{R} \frac{\rho_L}{\rho_V} (U_L - U_b) |U_L - U_b| + 3 \frac{\dot{R}}{R} \left[C_{AM,x} \frac{\rho_L}{\rho_V} (U_L - U_b) - U_b \right] - \frac{3}{4} \frac{\sigma}{\rho_V} \frac{f_{C,x}}{R^2} \quad (6.111)$$

Then, we numerically solve this equation from the moment when $R \geq R_d$ using a first order Euler scheme for a duration close to the experimental sliding time. To assess the validity of Eq 6.111, we modify the growth constant K in order to roughly match experimental radius measurements. The goal is to verify if the force balance allows a good prediction of bubble velocity provided a correct bubble growth. Next sections compare obtained results against low and high pressure data.

6.5.2 Low Pressure Sliding

Maity [35] provided simultaneous measurements of bubble radius and velocity over time in vertical boiling for three liquid mass fluxes near saturation conditions. The contact angles were kept the same as in 6.4.3 since Maity provided average values over the bubble lifetime.

Results are displayed on Figure 6.21. The model seems to fairly good predict bubble sliding velocity for the 3 cases. The moment of departure is a bit underestimated as previously observed (Figure 6.18).

The biggest discrepancy is observed for the case at $G_L = 143.8 \text{ kg/m}^2/\text{s}$. The slope of the velocity profile is close to the experiments, but the bubble reaches a nearly constant acceleration too rapidly which yields an approximately constant overestimation of 0.1 m/s.

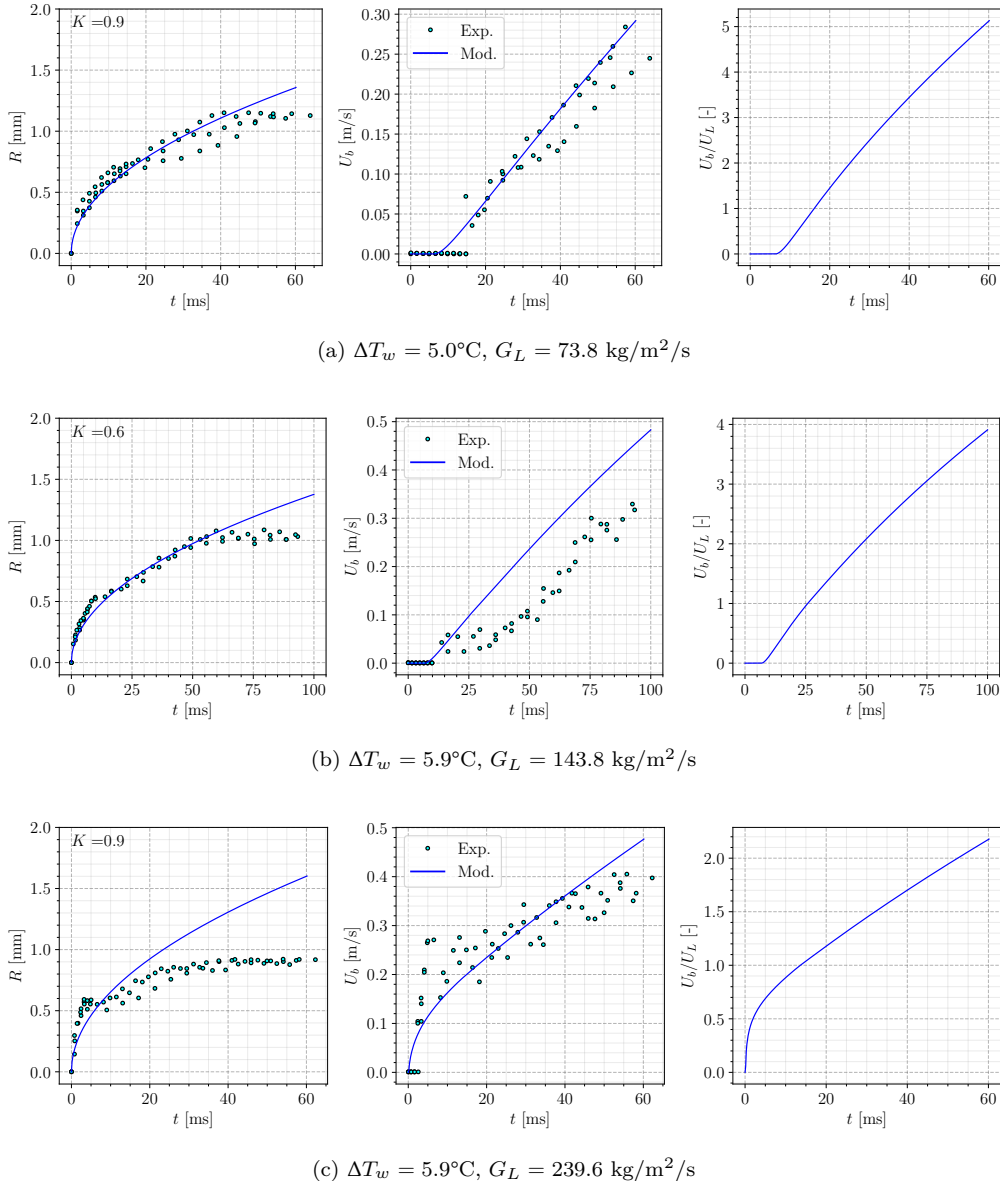


Figure 6.21: Bubble sliding velocity predictions on Maity cases

The $G_L = 239.6 \text{ kg/m}^2/\text{s}$ is well predicted regarding the velocity. However, the growth profile was difficult to match since measurements exhibit significant changes in growth regime after departure, which is probably due to the bubble being large enough to be impacted by the bulk flow. We can note that values of K between 0.5 and 1 were used to better fit the bubble radius time profile.

Regarding the relative velocity between the bubble and the surrounding liquid, the ratio $\frac{U_b}{U_L}$ greatly overcomes 1 which means the bubble slides much faster than the liquid. This is a consequence of both the low values of G_L along with the large bubble sizes inducing a great acceleration by the buoyancy force.

6.5.3 High Pressure Sliding

In his work, Kossolapov [28] conducted measurements of radius and sliding length over thousands of individual bubbles and then provided the associated statistical distributions. To compare our model with his measurements, we took the upper and lower bounds of R and l_{sl} over time and plotted the associated bands of measured values as shown on Figure 6.22 and 6.23.

Comparisons were done for cases at 20 bar and 40 bar and 3 different values of G_L . The value of $d\theta$ for the simulations was kept really small (2° at 20 bar and 0.5° at 40 bar) since bubble tilt is supposed

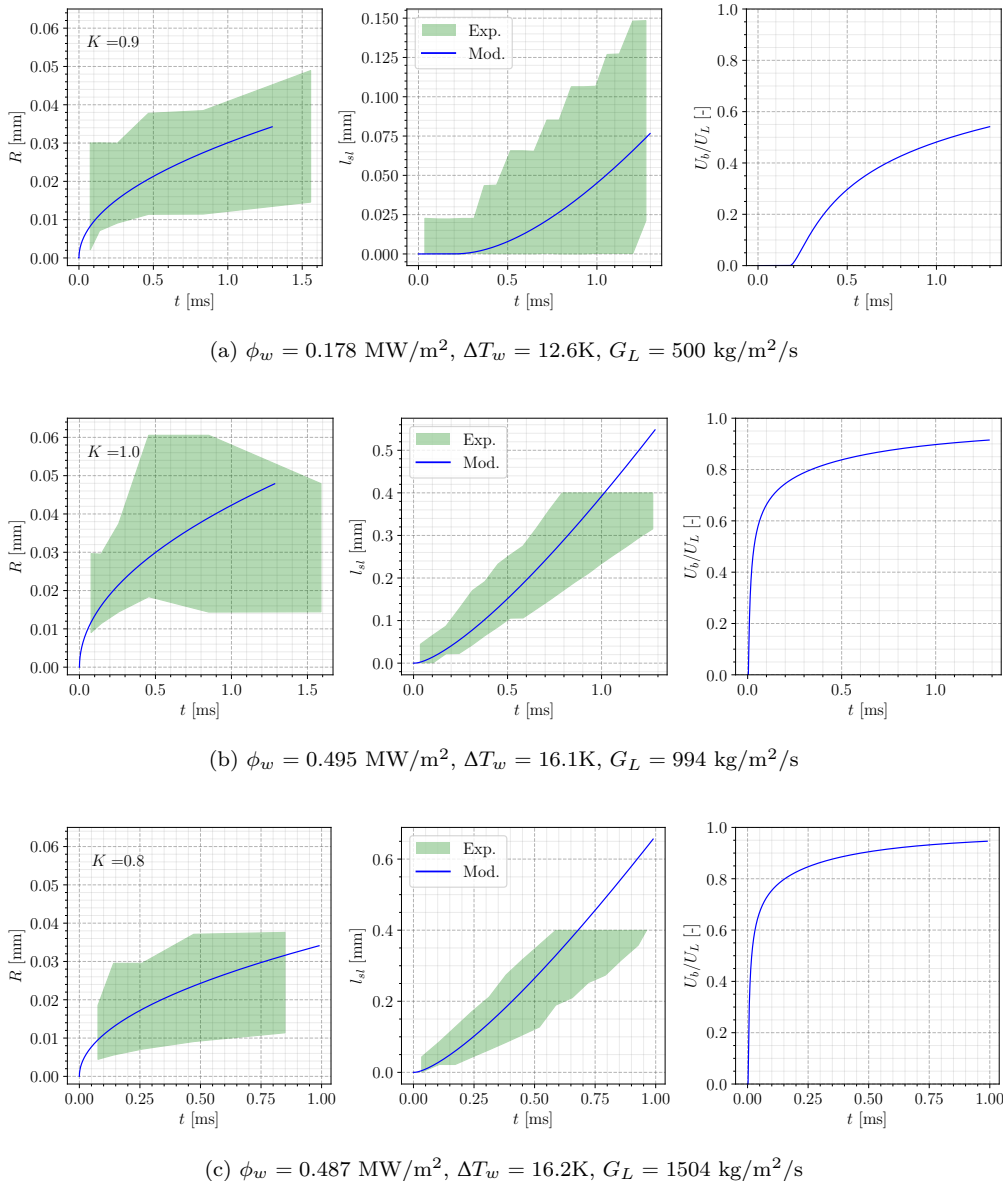


Figure 6.22: Bubble sliding length predictions on Kossolapov cases - $P = 20$ bar

to reduce during sliding because the relative velocity regarding the liquid flow is diminishing. Moreover, higher pressure means smaller bubbles that are even more unlikely to present a significant contact angle hysteresis. We also want to mention that neglecting the capillary term in Eq. 6.111 had a minor impact over the results except that the bubble accelerates a little bit faster.

The obtained results are in good agreement with the sliding length profile vs. time, which means bubble sliding velocity is well predicted for those cases. Values of K between 0.8 and 2 were needed to match the bubble radius measurements.

We see that bubbles are rapidly reaching sliding velocities between 80% and 95% of the local liquid velocity. Only the 20 bar case at $G_L = 500\text{kg/m}^2/\text{s}$ where the bubble departs slightly later, reaching approximately 55% of the liquid velocity.

6.5.4 Comparison of Forces in Sliding Stage

In order to identify the main accelerating forces, we compare the amplitude of the forces during the sliding phase for one low pressure case of Maity and one high pressure case of Kossolapov (Figure 6.24).

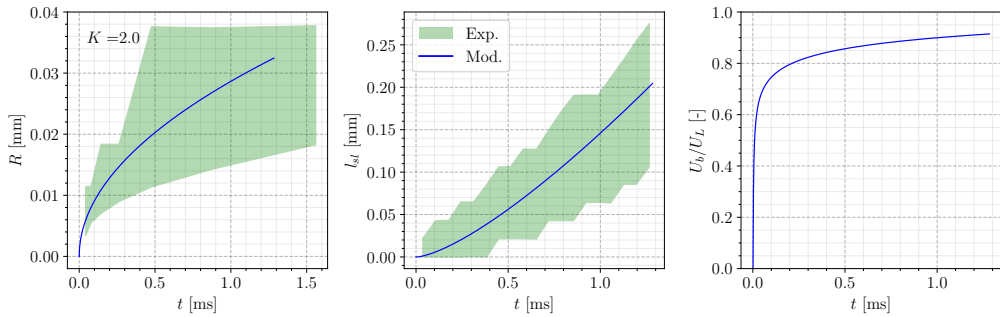
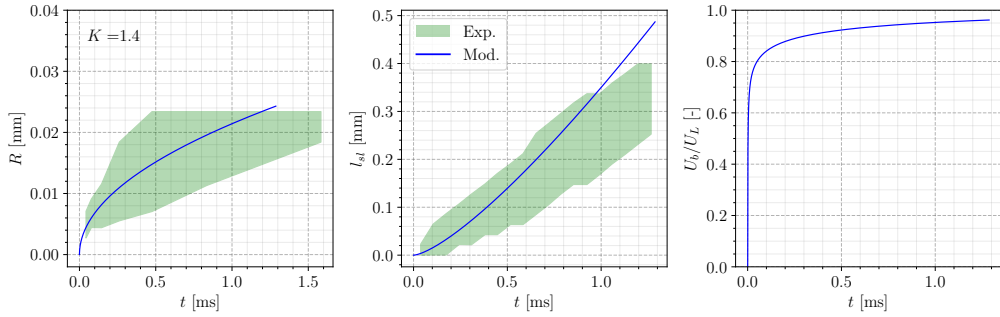
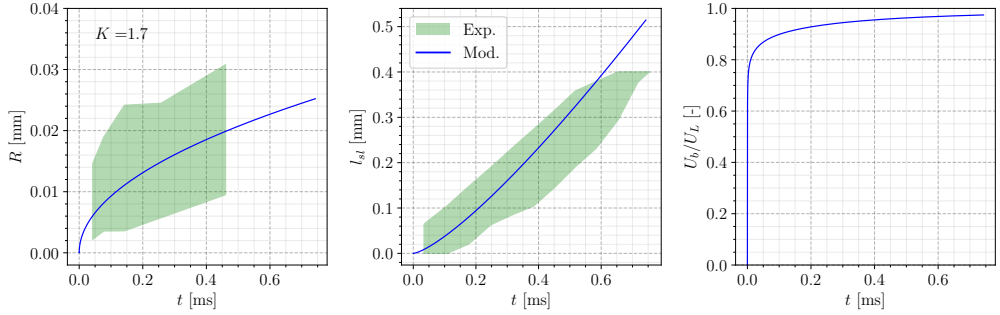
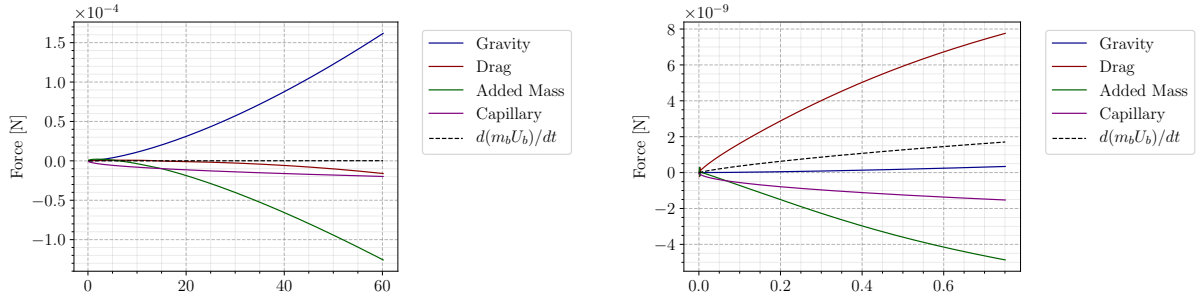
(a) $\phi_w = 0.291 \text{ MW/m}^2, \Delta T_w = 10.1\text{K}, G_L = 500 \text{ kg/m}^2/\text{s}$ (b) $\phi_w = 0.361 \text{ MW/m}^2, \Delta T_w = 10.8\text{K}, G_L = 994 \text{ kg/m}^2/\text{s}$ (c) $\phi_w = 0.613 \text{ MW/m}^2, \Delta T_w = 12.2\text{K}, G_L = 1504 \text{ kg/m}^2/\text{s}$ Figure 6.23: Bubble sliding length predictions on Kossolapov cases - $P = 40$ bar(a) Maity : $\Delta T_w = 5.9^\circ \text{C}, G_L = 239.6 \text{ kg/m}^2/\text{s}$ (b) Kossolapov : $P = 40 \text{ bar}, \phi_w = 0.613 \text{ MW/m}^2, G_L = 1504 \text{ kg/m}^2/\text{s}$

Figure 6.24: Amplitude of each force during sliding

It appears that at high pressure and liquid velocity, the drag force is the main driving force and stays positive since the bubble do not slide faster than the rapid surrounding liquid (reaching approximately

80% of the local liquid velocity). On the other hand, larger bubbles observed at low pressure and liquid velocity are accelerated by buoyancy due to their larger volume, with a nearly negligible Drag force. In both cases, the added mass force can not be neglected especially when bubble velocity rises by limiting its acceleration induced by the larger force (buoyancy or drag in the presented cases). This further emphasizes the importance of a proper derivation of the added mass force regardless of the boiling conditions. The capillary force seem to be a limited but constant slowing term in both cases. Finally, the amplitude of the forces involved can span from roughly 10×10^{-4} N at low pressure (much greater than the rate of change of bubble momentum laying around 10^{-9} N) down to a few nN at higher pressure (same order of magnitude as the rate of change of bubble momentum), especially due to the bubble size.

This comparison highlights the fact that the proposed model is able to represent different forces hierarchy depending on the flow conditions and to acceptably predict the associated bubble sliding velocity, which is an encouraging point regarding its generality.

6.6 BUBBLE LIFT-OFF

6.6.1 Introduction

The question of lift-off for a single bubble in vertical boiling is trickier than for horizontal boiling. Indeed, in horizontal boiling, lift-off is ensured thanks to the buoyancy force that will continuously increase as the bubble grows. It can also be promoted by the lift force if the bubble slides slower than the liquid. This facilitates the identification of the moment when bubble leaves the surface (Figure 6.25).

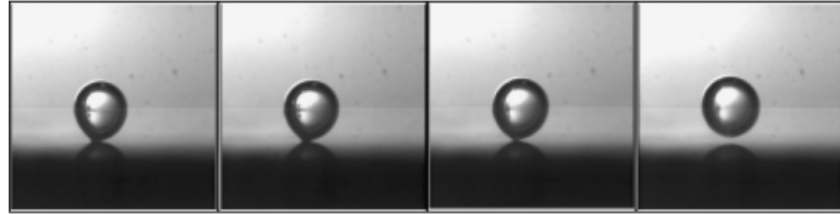


Figure 6.25: Visualization of bubble lift-off in horizontal boiling conducted by and adapted from Maity [35]. The detachment of the bubble base from the surface is clear in the last frame.

However, in vertical boiling, the lift-off from the surface only results of the competition between the added mass force and lift force (capillary force and contact pressure compensating each other for a truncated sphere). The added mass force keeps the bubble attached and the lift force which can either promote lift-off or push the bubble against the wall depending on the value of the lift coefficient C_L . As seen in Subsection 6.2.6, the lift coefficient can become negative when reaching negative relative velocity U_{rel} , yielding negative non-dimensional shear rates Sr in Eq. 6.39. In this case, the force balance perpendicular to the wall (Eq. 6.66) will never become positive and thus never predict bubble lift-off using criterion based on the force balance sign.

In addition, those two forces are difficult to precisely evaluate since they rely on complex phenomena such as the bubble growth (R , \dot{R} , \ddot{R}) and the fine hydrodynamics of a bubble attached to a wall. A small error on the evaluation of one of those forces can therefore lead to erroneous predictions of the lift-off phenomenon.

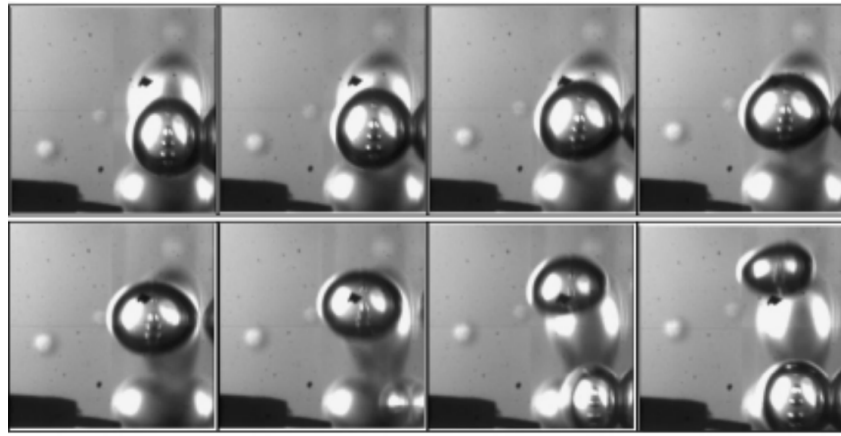
On the experimental side, different behavior for boiling bubbles in vertical boiling have been observed. Single bubble experiments such as those of Maity [35] and Situ *et al.* [56] observed bubble lift-off for single bubble at atmospheric pressure as shown on Figure 6.26.

Although bubble lift-off is observed for those single bubble cases, the exact moment of lift-off is complicated to identify since the bubbles sometimes stay very close to the wall and can even re-attach to the wall, presenting a bouncing motion while moving close to the wall as in Yoo *et al.* [69].

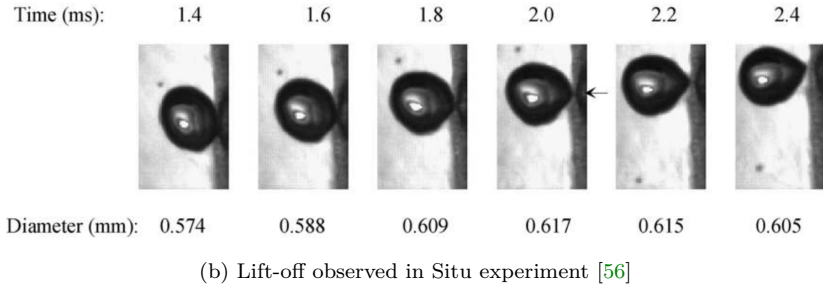
Contrary to those observations, other authors who realized experimental visualizations of vertical flow boiling of surfaces with numerous bubbles saw that single bubbles did not leave the wall by themselves. For instance, Scheiff [53] observed different possible behaviors :

- Bubble growth up to an equilibrium diameter while sliding on the wall and keeping the same size.
- Rapid sudden growth of bubbles can enlarge them up to the subcooled liquid, yielding to condensation while sliding on the wall.
- Bubble lift-off under application of a high heat flux (rapid growth) or after coalescence with an other bubble on its path.

Similar behaviors of bubbles sliding along the wall and not leaving it until a coalescence occurs has also been reported for vertical flow boiling by Prodanovic *et al.* [45] or Thorncroft *et al.* [61]. In particular, Prodanovic *et al.* mentioned that bubbles that would detach from the wall by themselves cannot be interpreted as typical bubble behavior in those conditions since there were very few of them. Typical experimental visualizations of this nature are presented on Figure 6.27

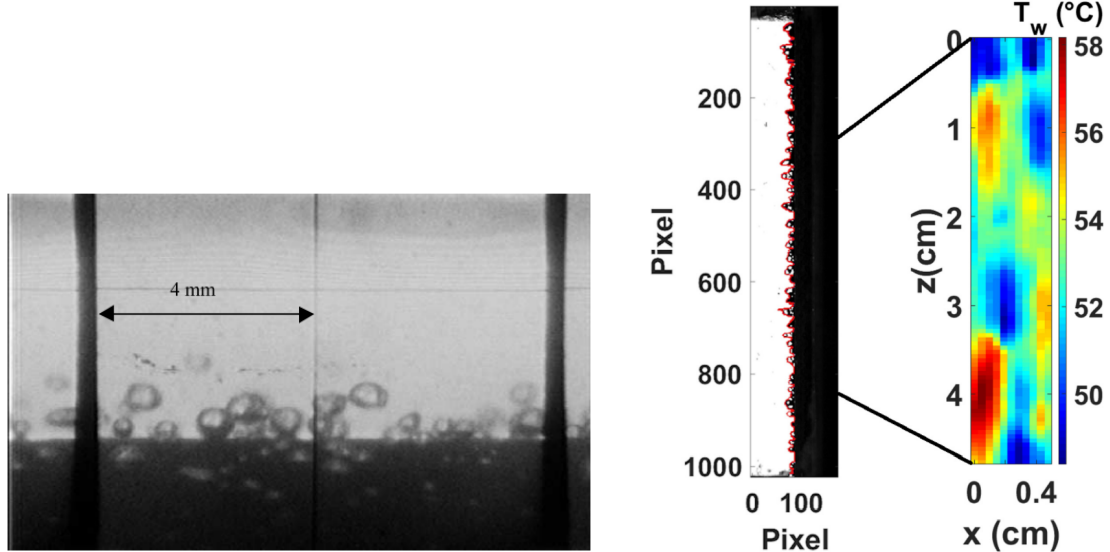


(a) Lift-off observed in Maity experiment [35]



(b) Lift-off observed in Situ experiment [56]

Figure 6.26: Visualization of bubble lift-off in vertical boiling. The moment when bubble leaves the surface appears less clearly than for horizontal boiling.



(a) Boiling visualization by and adapted from Prodanovic *et al.* [prodanovic] in the region where bubble coalescence started to occur.

(b) Boiling visualization by and adapted from Scheiff *et al.* [52], highlighting the observed layer of sliding bubbles.

Figure 6.27: Visualization of boiling surfaces in vertical boiling, where single bubble lift-off is not systematically observed.

Generally speaking, it seems that single bubbles in vertical boiling are not likely to present a lift-off behavior by themselves in every flow conditions that could be explored. As concluded by Okawa *et al.* [43] and discussed in Yoo *et al.* [69], it seems that a more general trigger for bubble

lift-off would be either associated to strong deformation / elongation of the bubble shape (inducing a change in the lift coefficient) or to a coalescence event between two bubbles.

To further discuss this question, we will try to consider the bubble lift-off as a single event and therefore try to attribute a given lift-off diameter D_{lo} based on available experimental measurements.

6.6.2 Experimental Measurements of Lift-Off Diameter

Observations and measurements of bubble diameter in various flow conditions have been conducted by numerous authors since the middle of the XXth century. Although recent experimental techniques allow to identify the moment at which bubble diameter is measured (departure from nucleation site, lift-off, etc.), older experiments could not ensure the nature of the bubbles that were observed.

For instance, the work of Ünal [77] measured the maximum bubble diameter and used other experimental results (Gunther [gunther], Griffith [griffith], Treshchev [treshchev] and Tolubinsky [tolubinsky]) to build a correlation. However, it can not be clearly stated that those measurements were single bubbles lifting off the surface or bubbles resulting of coalescence.

Remark : As explained by Ünal, their measurements (detailed in De Munk [DeMunk_bubbles]) are based on enlarged photographic observations of the bubble population near the boiling surface from which they extracted the maximum diameter, meaning there is no evidence that it was actually a lift-off diameter of a single bubble.

This was also pointed out by Kossolapov [28] who showed that at very high pressure, old measurements of bubble diameter were larger for flow boiling compared to pool boiling, which is intuitively unphysical. This could be explained as mentioned above if those measurements were actually coalesced bubbles which would naturally exhibit larger diameters than single bubbles at lift-off.

However, those measurements can still be interesting since their evolution with the operating conditions should present trends similar to single bubble experiments. To do so, we gathered several experimental data sets of maximum / lift-off diameter from the literature for vertical subcooled flow boiling of water. The experimental conditions of the data set are presented on Table 6.5.

6.6.3 Influence of the Flow Boiling Conditions

To evaluate the influence of the flow boiling conditions over the various experimental measurements, we have represented the values of the non-dimensional lift-off diameter $\frac{D_{lo}}{L_c}$ (L_c is the capillary length) versus 6 non-dimensional flow parameters:

- The reduced Jakob numbers of superheat and subcooling Ja_w^* and Ja_L^* . With $Ja_* = \frac{c_{p,L}\Delta T}{h_{LV}}$ which excludes the impact of pressure through the density ratio.
- The density ratio $\rho^* = \frac{\rho_L}{\rho_V}$, scaling the operating pressure.
- The saturated liquid Prandtl number Pr_L , quantifying the liquid thermal properties.
- The local wall Reynolds number $Re_\tau = \frac{\rho_L U_\tau L_c}{\mu_L}$, evaluating the impact of the liquid flow.
- The capillary number Ca which can be related to bubble deformability under viscous effects.

The results are presented on Figure 6.28.

The experimental values of $\frac{D_{lo}}{L_c}$ display the following trends:

- Increase with Ja_w^* ;
- Decrease with Ja_L^* ;

Author	Fluid	D_h [mm]	P [bar]	G_L [kg/m ² /s]	ΔT_L [K]	ϕ_w [kW/m ²]	ΔT_w [K]	D_d [mm] (N_{mes})
Gunther [gunther_bubblediam] (1951)	Water	6.92	1 - 1.7	1492 - 6070	33 - 86	2.3 - 10.64	N.A.	0.32 - 1.02 (12)
Griffith [griffith_bubdiam] (1958)	Water	12.7	34.5 - 103	4651 - 7593	11 - 80	3.25 - 8.53	N.A.	0.081 - 0.146 (6)
Treshchev [treshchev_1960] (1969)	Water	10.18	5 - 50	1643 - 1789	30 - 62	1.4 - 2.9	N.A.	0.12 - 0.26 (3)
Tolubinsky [63] (1970)	Water	10	1 - 10	72.6 - 198.4	5 - 60	0.47	N.A.	0.19 - 1.24 (9)
Ünal [77] (1976)	Water	8	139 - 177	2082 - 2171	3 - 5.9	0.38 - 0.55	N.A.	0.11 - 0.18 (7)
Maity [35] (2000)	Water	20	1.01	0 - 239.6	0.3 - 0.7	N.A.	5 - 5.9	1.8 - 2.4 (4)
Prodanovic [45] (2002)	Water	9.3	1.01 - 3	76.7 - 815.8	10 - 60	0.1 - 1.2	N.A.	0.366 - 2.68 (44)
Situ [56] (2005)	Water	19.1	1.01	471.8 - 910.8	1.5 - 20	0.06 - 0.2	N.A.	0.145 - 0.605 (90)
Chu [chu] (2010)	Water	22.25	1.45	301 - 702	3.4 - 22.6	0.135 - 0.201	N.A.	0.51 - 1.71 (14)
Ahmadi [ahmadi] (2012)	Water	13.3	0.96 - 1.13	169 - 497	8.4 - 20.6	0.16 - 0.318	11.4 - 18.4	0.12 - 3.9 (13)
Okawa [okawa_bubble] (2018)	Water 2018]	14	1.27 - 1.86	252 - 490	10 - 39	0.161 - 0.487	N.A.	0.64 - 0.188 (10)

Table 6.5: Bubble lift-off diameters data sets in vertical flow boiling

- Increase with ρ^* ;
- Increase with Pr_L ;
- Decrease with Re_τ and Ca .

A great range of D_{lo} values at low pressure (for which we have the larger number of measurements) are reached in the experiments. This further indicates the complicated behavior of bubble lift-off, for which similar flow conditions can lead to very different bubble diameters.

Remark : This variation could be associated to the heater material and surface morphology, which are not quantified here.

Moreover, we can observe that measurements from Ünal do not follow the general tendency of other data as on Figure 6.28c, with values of D_{lo}/L_c above the trend, further supporting the assumption that those experimental values were actually those of coalesced bubbles.

6.6.4 Predicting the Lift-Off with a Force Balance

As previously discussed, the prediction of the lift-off using the force balance perpendicular to the wall (Eq. 6.66) is complicated because:

- The spherical shape without tilt ($d\theta = 0$) leads to exact compensation between contact pressure force and capillary force. Leaving only the added mass force and lift force to predict the lift-off.

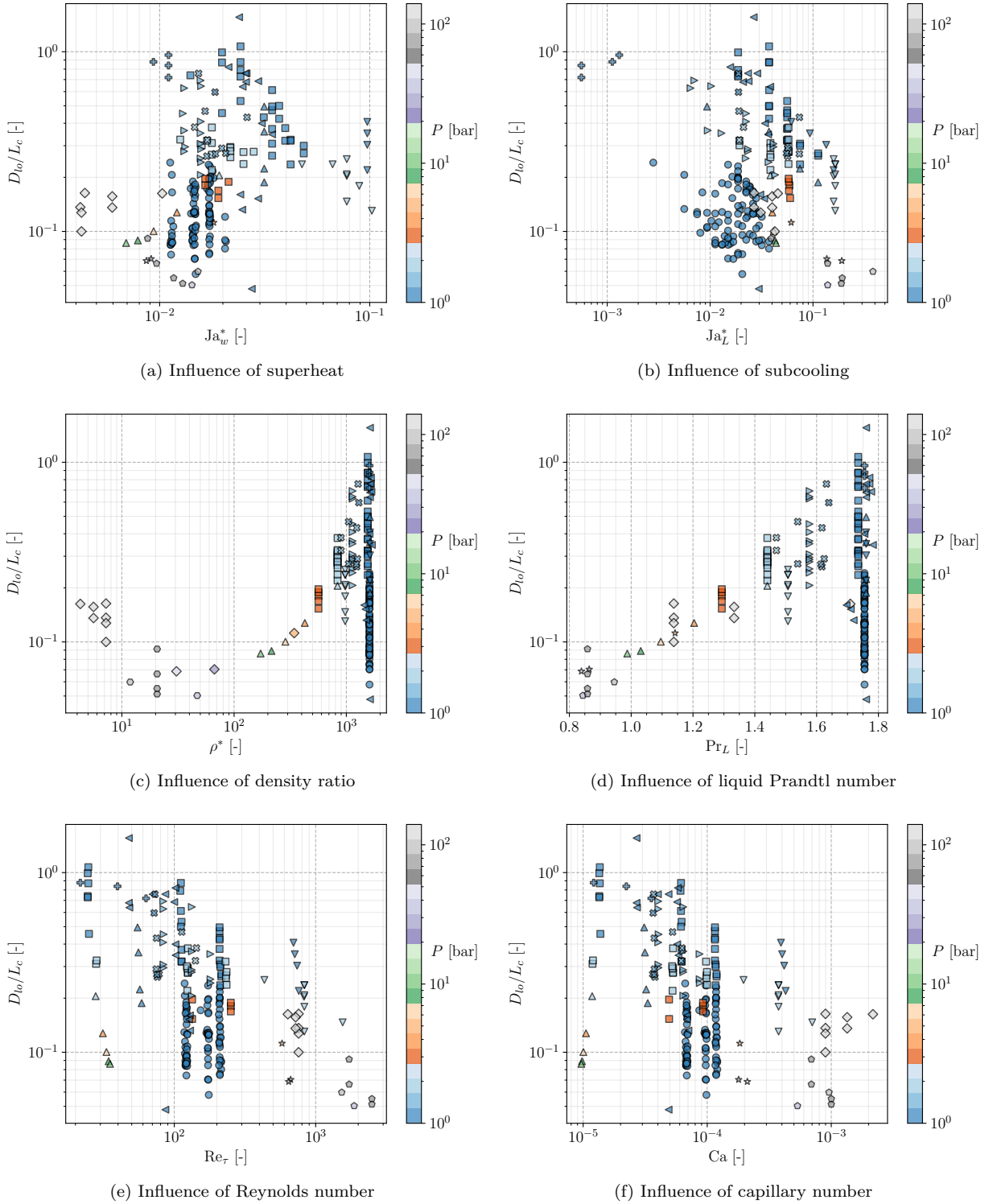


Figure 6.28: Evolution of D_{lo}/L_c depending on the flow conditions. Gunther: ∇ ; Griffith: Pentagons - Treshchev: \star ; Tolubinsky: \triangle ; Ünal: \diamond ; Maity: $+$; Prodanovic: \square ; Situ: \circ ; Chu: \triangleright ; Ahmadi: \triangleright ; Okawa: \times

- Those two forces can both be directed toward the wall depending on the flow conditions, making it impossible for a single bubble to lift-off by itself.
- The estimation of those forces rely on complicated description of thermal and hydrodynamic phenomena, making a simple mistake a source of large errors on lift-off prediction.

This difficulty has already been pointed out by Montout [**montout_phd**] who faced difficulties in consistently using the force balance perpendicular to the wall for bubble lift-off.

To demonstrate this uncertainty, we present on Figure ?? the predictions achieved when the lift-off is associated to a positive force balance perpendicular to the wall (Eq. 6.66).

FIGURE

The results are greatly dispersed and do not seem to demonstrate any coherent trend with the experimental measurements.

6.6.5 A Simple Non-Dimensional Correlation

As an alternative way to estimate the lift-off / maximum bubble diameter D_{lo} , we propose a simple correlation based on non-dimensional numbers as:

$$\frac{D_{lo}}{L_c} = e^{8.779} \text{Pr}_L^{-0.065} \left(\frac{\rho_L}{\rho_V} \right)^{-0.374} \text{Ja}_w^{* 1.188} (1 + \text{Ja}_L)^{-6.853} (1 + \text{Re}_\tau)^{-0.547} \quad (6.112)$$

6.6.6 Conclusion on the Lift-Off

CLOSURE LAWS FOR THE HEAT FLUX PARTITIONING MODEL

7.1 SINGLE-PHASE HEAT TRANSFER COEFFICIENT

The choice of a proper correlation to compute the single-phase heat transfer coefficient is a first but inevitable step to build a HFP model. Indeed, if the single-phase convection term is badly computed, the resulting boiling model will fail to predict the wall temperature.

For instance, if the liquid convective HTC is overestimated, it would result in a delayed increase of the boiling and quenching heat fluxes which would in turn lead to an overprediction of the wall temperature. To assess existing correlations for the single-phase HTC, we will use wall temperature measurements extracted from experimental boiling curves for water where $T_w \leq T_{sat}$. They correspond to the single-phase part of the experimental data later used to assess the HFP model.

The chosen data are presented on Table 7.1.

Author	D_h [mm]	P [bar]	G_L [kg/m ² /s]	ΔT_L [K]	ϕ_w [MW/m ²]	$T_{sat} - T_w$ [K]	N_{mes} [-]
Kossolapov [28] (2021)	12	10.5	500 - 2000	10	0.1 - 0.6	0.22 - 9.5	12
Richenderfer [richenderfer_phd] (2018)	15	1 - 5	1000 - 2000	10-20	0.1 - 0.63	1 - 18.7	13
Jens-Lottes [jens_lottes_data] (1951)	5.74	137.9	2617.5	53.3 - 92.2	0.91 - 2.37	0.33 - 44.1	15
Kennel [kennel_phd] (1948)	4.3 - 13.2	2 - 6.2	284 - 10 577	11.1 - 83.3	0.035 - 1.89	0.35 - 69	52

Table 7.1: Experimental data range of wall temperature measurements from the single-phase part of boiling curves.

On Figure 7.1, we compare the results of wall temperature prediction in the single-phase region obtained with the correlation of Dittus-Boelter (Eq. ??) and Gnielinski (Eq. ??).

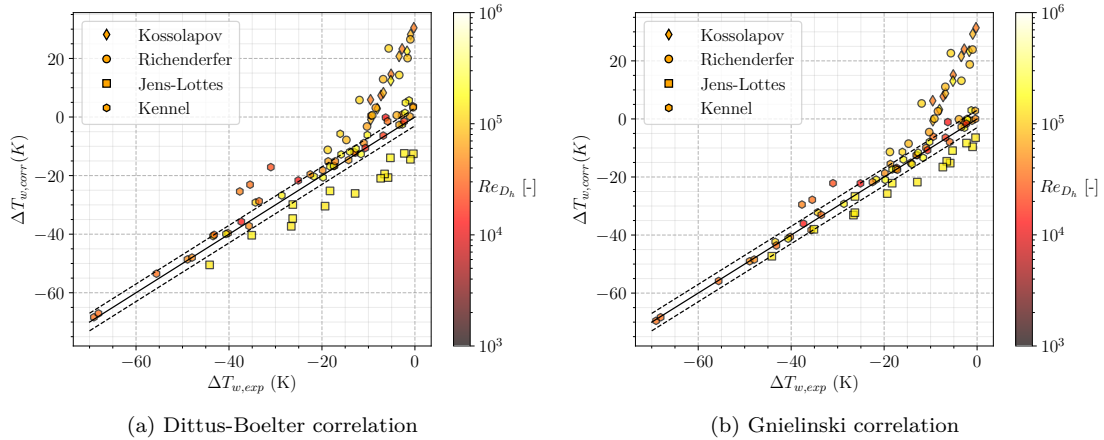


Figure 7.1: Predictive capability of wall temperature by single-phase heat transfer correlations. $\pm 3K$ error bars indicated.

The two correlations are of similar efficiency regarding wall temperature predictions over the considered data sets. They both have very good agreement with Kennel data and clear overestimations of ΔT_w on

Richenderfer and Kossolapov measurements. The slope difference compared to the parity implies that the correlations are predicting too small Nusselt numbers for those cases.

Regarding Jens-Lottes data, both model underestimate the wall temperatures, with better results achieved by Gnielinski correlation.

Remark : We tested different friction factor along with different values of wall roughness in the Gnielinski correlation and observed a negligible impact on the overall results. This allows to stay with a simple formulation for the friction coefficient.

The error obtained on Richenderfer and Kossolapov data can be explained by the definition of the HTC computed by Gnielinski correlation. Indeed, Gnielinski correlated a Nusselt number associated to a forced convection coefficient $h_{fc,Gniel}$ in the case of a internal flow with a completely heated wall.

However, only one side of the channel is heated in Richenderfer and Kossolapov experiments. If S_{heat} denotes this actual heated surface, then Gnielinski correlation estimates the HTC for a surface $4S_{heat}$. With the same imposed total heat power Φ_w and bulk liquid temperature T_L , we have:

$$h_{fc,Gniel} = \frac{\Phi_w}{(T_{w,Gniel} - T_L) 4S_{heat}} \quad (7.1)$$

$$h_{fc,exp} = \frac{\Phi_w}{(T_{w,exp} - T_L) S_{heat}} \quad (7.2)$$

Writing $T_{w,Gniel} = T_{w,real}$ then yields:

$$h_{fc,exp} = 4h_{fc,Gniel} \quad (7.3)$$

Remark : This correction can be interpreted as using the thermal diameter instead of the hydraulic diameter, which is 4 times smaller when only one side of the channel is heated.

On Figure 7.2 we display the predictions of Gnielinski correlation including this correction by a factor 4 on the HTC for Richenderfer and Kossolapov cases. We also test a 10% reduction on the HTC for Jens-Lottes cases to assess the error made by Gnielinski correlation.

On the same Figure, we also present predictions achieved with the local HTC estimation implemented in NCFD (Eq. ??), using a value of $y^+ = 100$.

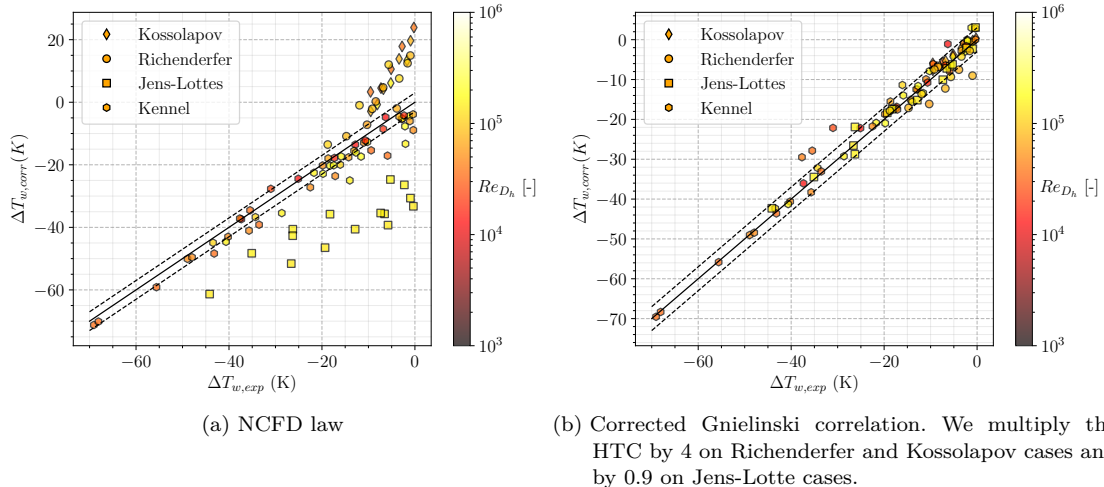


Figure 7.2: Predictive capability of wall temperature by NCFD law and Gnielinski correlation including corrections. $\pm 3K$ error bars indicated.

The NCFD approach yields predictions similar to the 1D correlations (Figure 7.1) with larger underestimations on Jens-Lottes measurements. On the other hand, we see that applying a constant correction to the Gnielinski correlation (4 for Kossolapov and Richenderfer cases, 0.9 for Jens-Lottes cases) suffices to yield accurate predictions on the whole range of wall temperature measurements.

Remark : The NCFD law was tested without running CFD simulations. The equations were re-written in python to allow its testing outside of the whole code. The use of $y^+ = 100$ as well as the Mac Adams correlation (Eq. ??) for the friction velocity U_τ may induce a difference with the predictions that could be achieved by running a complete CFD computation of the considered cases.

The average errors obtained with each model are summed up on Table 7.2

Model	Kossolapov err. [K]	Richenderfer err. [K]	Jens-Lottes err. [K]	Kennel err. [K]
Dittus-Boelter	19.67	15.07	10.09	3.13
Gnielinski	20.31	14.06	6.09	1.74
NCFD law	15.52	9.25	23.69	3.36
Corrected Gnielinski	1.34	3.08	1.57	1.74

Table 7.2: Average errors achieved by the considered models on each data sets.

Recalling that Gnielinski correlation was also providing good results on the DEBORA cases with R12 (Chapter ??), this further indicates it as a proper choice regarding single-phase HTC estimation in the HFP model. However, we will later allow the use of the correction factors when needed to ensure a proper representation of the single-phase part when trying to assess the models associated to boiling.

7.2 SINGLE BUBBLE QUENCHING AREA

When computing the quenching heat flux, we need to provide the total wall area visited by a single bubble $A_{q,1b}$ that will undergo quenching.

In wall boiling model that do not consider bubble sliding [**kurul_podowski**, **ncfd_hfp**, **shaver_podowski**] the impacted area at bubble lift-off is often considered as :

$$A_{q,1b} = F_A \pi R_{lo}^2 \quad (7.4)$$

with F_A being an enhancement factor that accounts for the possibility that the bubble will induce quenching over a surface larger than its projected area.

$$A_{q,1b} = \begin{cases} \pi R_{lo}^2 & \text{if } l_{sl} \leq R_{lo} - R_d \\ \frac{1}{2} \pi R_d^2 + l_{sl} (R_d + R_{lo}) + \frac{1}{2} \pi R_{lo}^2 & \text{if } l_{sl} \geq R_{lo} + R_d \end{cases} \quad (7.5)$$

Which can be re-expressed by defining $l_{sl}^* = \frac{l_{sl}}{R_{lo}}$ and $A_{q,1b}^* = \frac{A_{q,1b}}{\pi R_{lo}^2}$

$$A_{q,1b}^* = \begin{cases} 1 & \text{if } l_{sl}^* \leq 1 - \frac{R_d}{R_{lo}} \\ \frac{1}{2} \left(1 + \left(\frac{R_d}{R_{lo}} \right)^2 \right) + \frac{l_{sl}^*}{\pi} \left(1 + \frac{R_d}{R_{lo}} \right) & \text{if } l_{sl}^* \geq 1 + \frac{R_d}{R_{lo}} \end{cases} \quad (7.6)$$

and we linearly interpolate those two expressions for the region where $1 - \frac{R_d}{R_{lo}} \geq l_{sl}^* \geq 1 + \frac{R_d}{R_{lo}}$.

7.3 GROWTH TIME

In this case, the average radius of the bubble over a growth time t_g (as needed in Subsection ??) is :

$$\overline{R(t)} = \frac{1}{t_g} \int_0^{t_g} R(t) dt = \frac{R_\infty}{t_g} \left[\frac{e^{-2K_a\sqrt{t}} (2K_a\sqrt{t} + 1)}{2K_a^2} + t \right]_0^{t_g} \quad (7.7)$$

$$= \frac{R_\infty}{2K_a^2 t_g} \left(e^{-2K_a\sqrt{t_g}} (2K_a\sqrt{t_g} + 1) + 2K_a^2 t_g - 1 \right) \quad (7.8)$$

Moreover, if we consider a lift-off radius R_d , we can express the associated growth time t_g :

$$t_g = \left[\frac{1}{K_a} \ln \left(\frac{1}{\sqrt{1 - \frac{R_d}{R_\infty}}} \right) \right]^2 = \left[\frac{1}{K_a} \ln \left(\sqrt{1 - \frac{R_d}{R_\infty}} \right) \right]^2 \quad (7.9)$$

This expression could then be used as a closure relationship for t_g in the HFP model, meaning that this growth time will depend on the departure diameter closure for R_d .

7.3.1 Estimation of the thermal boundary layer thickness δ

In order to fully close the modeling of the bubble growth, we have to compute the thermal boundary layer thickness δ .

To do so, we test a first approach based on the hydrodynamic boundary layer profile. In the turbulent layer, the non-dimensional liquids velocity u_l^+ is :

$$u_l^+ = \frac{1}{\kappa} \ln(y^+) + B, \text{ with } \kappa = 0.41 \text{ and } B = 5.25 \quad (7.10)$$

Since $u_l^+(y^+) = u_l(y)/u_\tau$ and $y^+ = yu_\tau/\nu_l$, we can compute the height of the hydrodynamic boundary layer δ_h where $u_l(\delta_h) = 0.99u_{l,bulk}$ as :

$$\delta_h = e^{\kappa(0.99u_{l,bulk}\sqrt{\rho_l/\tau_w} - B)} \times \nu_l \sqrt{\frac{\rho_l}{\tau_w}} \quad (7.11)$$

where τ_w is computed using the Mac Adams correlation (Eq. ??).

Finally, to get an approximation of the thermal boundary layer thickness, we consider a simple first approach as :

$$\delta = \frac{1}{Pr} \delta_h \quad (7.12)$$

Since the Prandtl number is the ratio of momentum diffusivity to thermal diffusivity, its inverse shall approximately scale the ratio between the thermal boundary layer and hydrodynamic boundary layer thickness.

7.3.2 Estimation of t_g against experimental data

In order to assess the proposed approach to compute t_g , we compare the yielded results with data taken from Unal of maximum bubble growth.

Only 6 measurements of maximum growth time are available (**Je vais en ajouter d'autres par la suite**) but they are associated with the bubble lift-off diameter. Since those measurements were conducted with boiling water on stainless steel, we set the contact angle at $\alpha = 80^\circ$.

We also compare the predictions with the model proposed by Kommajosyula :

$$t_g = \left(\frac{D_d}{4K} \right)^2 \quad (7.13)$$

$$K = \frac{\sqrt{\eta_l} \text{Ja}_w}{0.804\sqrt{\text{Pr}_l}} + \chi 1.95 \text{Ja}_w \eta_l, \text{ with } \chi = A - B\zeta \quad (7.14)$$

where $\zeta = \text{Ja}_l/\text{Ja}_w$ and both $A = 1.55$ and $B = 0.05$ have been fitted over the data of Klausner by Mazzocco *et al.*.

The results are displayed on Figure 7.3.

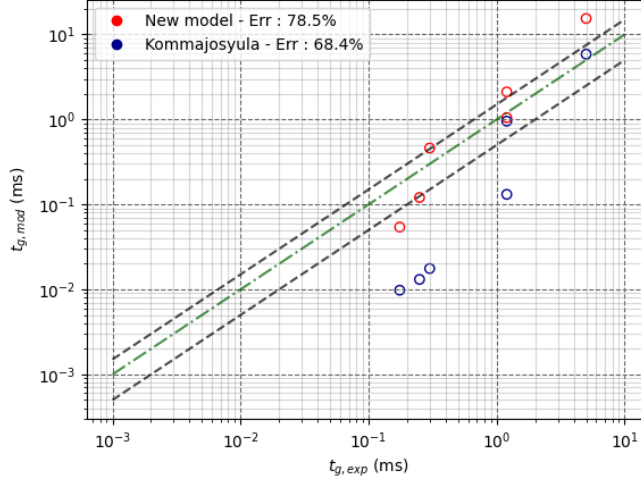


Figure 7.3: Comparison of the proposed model and Kommajosyula model against experimental data from Unal. Black lines represent the $\pm 50\%$ error bars.

As we can see, the average error from our model is greater than Kommajosyula's one. However, this is mainly due to the highest measured growth time (upper right point). Without this measurement, the average error reaches 52.5%, indicating that a much greater number of experimental measurements should be needed properly evaluate each model.

On the other hand, we may consider that the proposed approach could be of interest since it is not based on data-fitted parameters while providing reasonable results.

Author	Fluid	D_h [mm]	P [bar]	G_L [kg/m ² /s]	ΔT_L [K]	ϕ_w [kW/m ²]	ΔT_w [K]	D_d [mm] (N_{mes})
Maity [35] (2000)	Water	20	1.01	0 - 239.6	0.3 - 0.7	N.A.	5 - 5.9	0.788 - 1.71 (9)
Kossolapov [28] (2021)	Water	20	20 - 40	500 - 1500	0.3 - 0.7	N.A.	5 - 5.9	0.788 - 1.71 (9)

Table 7.3: Bubble growth time data in vertical flow boiling

7.4 BUBBLE WAIT TIME

The wait time between two nucleation events on an active site corresponds to the time needed for the thermal boundary layer to reconstruct after its disruption due to bubble departure from the nucleation site.

Formulation of Basu *et al.* [basu_heat_2005]:

$$t_w = 139.1 \Delta T_w^{-4.1} \quad (7.15)$$

Formulation of Kommajosyula [Komma]:

Author	Fluid	D_h [mm]	P [bar]	G_L [kg/m ² /s]	ΔT_L [K]	ϕ_w [kW/m ²]	ΔT_w [K]	D_d [mm] (N_{mes})
Basu <i>et al.</i> [basu_heat] (2005)	Water	20	1.01	0 - 239.6	0.3 - 0.7	N.A.	5 - 5.9	0.788 - 1.71 (9)
Richenderfer <i>et al.</i> [richenderfer_investigations_2018] (2018)	Water	20	1.01	0 - 239.6	0.3 - 0.7	N.A.	5 - 5.9	0.788 - 1.71 (9)
Kossolapov <i>et al.</i> [28] (2021)	Water	20	1.01	0 - 239.6	0.3 - 0.7	N.A.	5 - 5.9	0.788 - 1.71 (9)

Table 7.4: Bubble wait time data in vertical flow boiling

$$t_w = 0.061 \frac{\text{Ja}_L^{0.63}}{\Delta T_w} \quad (7.16)$$

Remark : Kommajosyula's correlation yields a zero wait time when bulk liquid approaches saturation. This behavior is questionable

Mikic & Rosenhow analytical expression [**mikic**]:

$$t_w = \frac{1}{\pi \eta_L} \left[\frac{(\Delta T_w + \Delta T_L) R_c}{\Delta T_w - T_{sat} \left(\frac{1}{\rho_V} - \frac{1}{\rho_L} \right) \frac{2\sigma}{h_{LV} R_c}} \right]^2 \quad (7.17)$$

A relevant

7.5 NUCLEATION SITE DENSITY

The Nucleation Site Density is among the most influencing parameters over the HFP models predictions, particularly regarding wall temperature. Indeed, its value directly controls the density of bubbles generated at the heater and therefore impacts both the boiling (ϕ_e) and quenching (ϕ_q) heat fluxes to the first order. Being able to come up with correct predictions of the NSD is thus critical if one wishes to properly capture the thermal behavior of the boiling surface.

However, the value of N_{sit} is actually influenced by many parameters being either linked to thermal-hydraulics (wall temperature, pressure, operating fluid) or the heater material (roughness, wettability). That is why its value is often estimated through empirical correlations, for which many different expression have been proposed over the years since the end of the XXth century.

One of the firstly identified behavior of the NSD was its power dependency with the wall superheat ($N_{sit} \propto \Delta T_w^m$), which is form adopted in the correlation of Lemmert & Chawla [**Lemmert**] :

$$N_{sit} = [210 (T_w - T_{sat})]^{1.8} \quad (7.18)$$

Remark : This law is used in the HFP model of Kurul & Podowski and NEPTUNE_CFD to compute N_{sit} .

However, such an expression misses the influence of other parameters such as pressure, which has been proven to be strongly impacting the range of active cavities that can generate bubbles as shown on Figure 7.4 and induces a larger bubble density over the heater.

Moreover, experimental measurements such as in Borishanskii [**borishanskii**] showed that the power dependency on the wall superheat changes by increasing both with pressure and the superheat value itself.

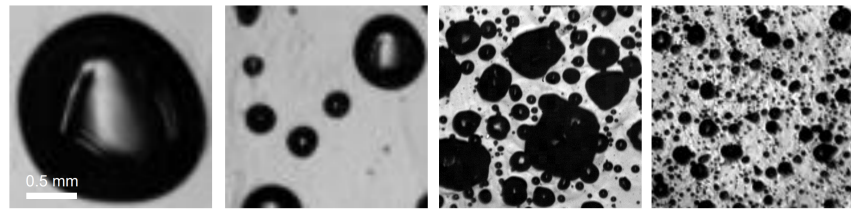


Figure 7.4: HSV Visualization of bubble density at various pressures adapted from Kossolapov [28] (left to right: 1.01 bar, 3 bar, 19.8 bar, 75.8 bar).

This was accounted for by Hibiki & Ishii in 2003 [[hibiki_ishii](#)] who came up with a new correlation that requires an estimation of the minimum activated cavity radius R_c :

$$N_{sit} = N_0 \left(1 - \exp \left(-\frac{\theta^2}{8\mu^2} \right) \right) \left[\exp \left(f(\rho^+) \frac{\lambda'}{R_c} \right) - 1 \right] \quad (7.19)$$

$$R_c = \frac{2\sigma \left(1 + \frac{\rho_V}{\rho_L} \right) / P}{\exp \left(\frac{h_{LV} \Delta T_w}{R_g T_w T_{sat}} \right) - 1} \quad (7.20)$$

$$f(\rho^+) = -0.01064 + 0.48246\rho^+ - 0.22712\rho^{+2} + 0.05468\rho^{+3} \quad (7.21)$$

with R_g the perfect gas constant times the molar mass of the fluid, $N_0 = 4.72 \times 10^5 \text{ m}^{-2}$, $\mu = 0.722 \text{ rad}$, $\lambda' = 2.5 \times 10^{-3} \text{ m}$ and $\rho^+ = \log_{10} \left(\frac{\rho_L - \rho_V}{\rho_V} \right)$.

Remark : This law is used in the HFP model of Gilman & Baglietto [[gilman_baglietto](#)].

We can note that it also includes the value of the static contact angle θ which can be used as a parameter to accounts for wall properties, since it is dependent on the wall roughness, wettability and the operating fluid.

Indeed, a high-wetting material (low values of θ) will allow smaller cavities to be flooded by the surrounding liquid, thus hindering non-condensable gases to be captured inside and become a potentially active nucleation site (Figure 7.5).

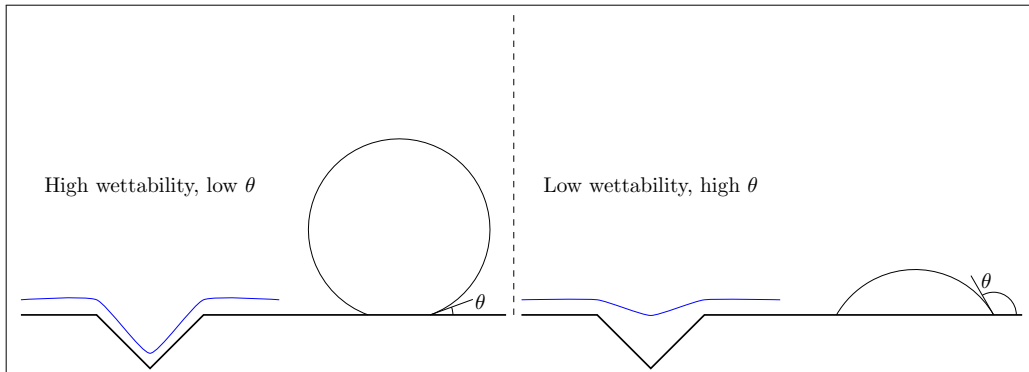


Figure 7.5: Sketch of the link between bubble contact angle and wettability / cavity flooding

This influence of the contact angle on the NSD was confirmed by experimental obversations of Basu *et al.* [[basu_nsit](#)] and was also included in a law correlated on their own measurements :

$$N_{sit} = \begin{cases} 0.34 [1 - \cos(\theta)] \Delta T_w^2 & \text{if } \Delta T_{w,ONB} < \Delta T_w < 15 \text{ K} \\ 3.4 \times 10^{-5} [1 - \cos(\theta)] \Delta T_w^{5.3} & \text{if } \Delta T_w > 15 \text{ K} \end{cases} \quad (7.22)$$

Similarly, Zhou *et al.* [[zhou_nsd](#)] correlated their measurements, including an influence of the pressure:

$$N_{sit} = N_0 (1 - \cos(\theta)) [\exp(f(P) \Delta T_w) - 1] \quad (7.23)$$

$$f(P) = 0.218 \ln\left(\frac{P}{P_0}\right) + 0.1907 \quad (7.24)$$

with $N_0 = 55\,395.26 \text{ m}^{-2}$ and $P_0 = 1.01 \text{ bar}$.

Finally, one of the most recent NSD correlation has been proposed by Li *et al.* in 2018 [li_new_2018] and validated over a large range of measurements by including a more realistic power law for ΔT_w . It avoids the divergence of N_{sit} observed in Hibiki & Ishii law (Eq. 7.19) when reaching high pressure and superheats. It also includes the impact of pressure and contact angle and its evolution with temperature *e.g.* its decrease close to 0° when approaching the critical temperature [song_fan_contact_angle]:

$$N_{sit} = N_0 e^{f(P)} \Delta T_w^{A \Delta T_w + B} (1 - \cos(\theta)) \quad (7.25)$$

$$f(P) = 26.006 - 3.678e^{-2P} - 21.907e^{-P/24.0.65} \quad (7.26)$$

$$A = -2 \times 10^{-4} P^2 + 0.0108P + 0.0119 \quad (7.27)$$

$$B = 0.122P + 1.988 \quad (7.28)$$

$$1 - \cos(\theta) = (1 - \cos(\theta_0)) \left(\frac{T_c - T_{sat}}{T_c - T_0} \right)^\gamma \quad (7.29)$$

with P in MPa, θ_0 the contact angle at room temperature T_0 , and default value being for water $\theta_0 = 41.37^\circ$, $T_c = 374^\circ\text{C}$ $T_0 = 25^\circ\text{C}$, $\gamma = 0.719$.

Remark : We can question the absence of bulk liquid velocity and temperature in the presented law since they should logically influence the nucleation process. However, this impact is rather limited as observed in experimental measurements of Zhou *et al.* and Kossolapov.

In order to assess existing NSD correlations and choose the most pertinent to include in a HFP model, we gather NSD measurements from 4 different authors. The different operating conditions of the chosen data sets are gathered on Table 7.5.

Author	Fluid	P [bar]	G_L [kg/m ² /s]	ΔT_L [K]	ΔT_w [K]	θ_0 [°]	N_{mes} [-]
Zhou [zhou_nsit] (2020)	Water	1.21 - 3.12	482.7 - 1930.6	8 - 15	6.7 - 20.2	51	60
Richenderfer [richenderfer] (2018)	Water	1.01	500 - 1000	10	21.7 - 42.8	80	49
Kossolapov [28] (2021)	Water	1.01 - 75.8	500 - 2000	80	10	80°	63
Borishanskii [borishanskii] (1966)	Water	1.01 - 198	N.A.	N.A.	1.75 - 17.3	45	132

Table 7.5: Nucleation Site Density data in flow boiling

We then compare the predictions achieved by the model of Lemmert & Chawla (Eq. 7.18), Hibiki & Ishii (Eq. 7.19), Zhou *et al.* (Eq. 7.23) and Li *et al.* (Eq. 7.25). The comparison with measurements are presented on Figure 7.6.

The Lemmert & Chawla model appears to fail in predicting the NSD at high pressures. This is a logical drawback of its sole dependence on the wall superheat. More importantly it increasingly underestimates the NSD as pressure increases, which makes it a clearly unsuitable correlation to compute N_{sit} particularly for pressurized flows such as in PWR.

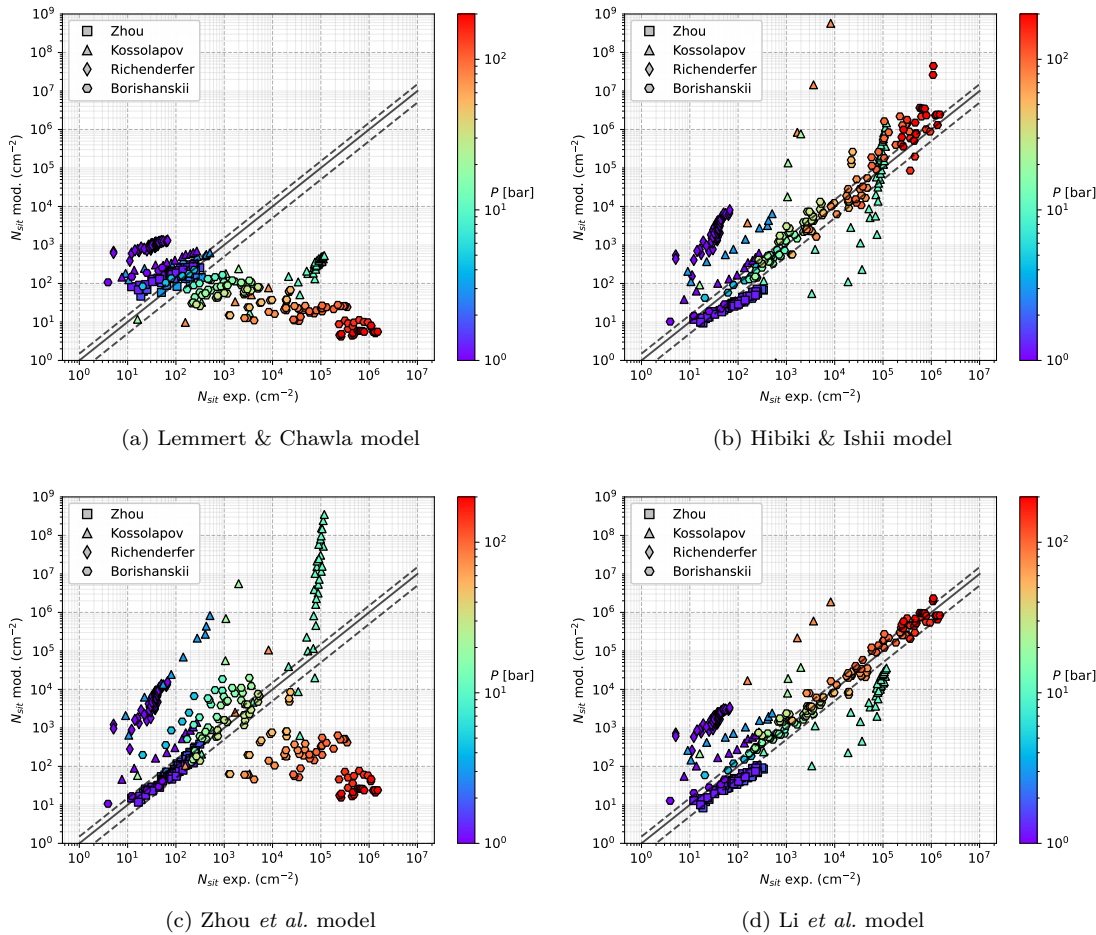


Figure 7.6: Predictions of the chosen models against the experimental data of Table 7.5 with $\pm 50\%$ error bars.
The contact angles

Altough the model of Zhou *et al.* includes a pressure term, its partial calibration on data covering a low range of pressure may explain the large error observed when compared to higher pressure measurements. On the contrary, models from Hibiki & Ishii and Li *et al.* seem to better reproduce the different trends with flow conditions, especially with pressure. The model from Li *et al.* achieves better predictions by avoiding to reach unphysically high values of N_{sit} at higher wall superheat compared to Hibiki & Ishii. This behavior is clear over Kossolapov data at high pressure, where both model lead to overestimations, the strongest discrepancy being associated to Hibiki & Ishii model.

Overall, the model of Li *et al.* is the most efficient with an acceptable agreement on most of the data of Borishanskii and Zhou *et al.*. The measurements of Richenderfer and Kossolapov fail to be precisely reproduced, but it shows a coherent trend and the most limited error when compared to other correlations.

Remark : The coherency of NSD predictions is hard to ensure since we do not know the exact contact angle and boiling surface morphology in the experiments. This was pointed out by Richenderfer [Richen_phd] who observed significant variation in the NSD value depending on the heater, though keeping the same material (ITO). For instance, this may explain the fact that the NSD measured by Kossolapov at 10.5 bar is higher than any other pressure on his experiment, leading to both underpredictions and overpredictions of the model of Li *et al.* depending on the pressure.

All things considered, those comparisons show that the Nucleation Site Density remains among the most difficult quantity to evaluate because of its very large variations over experiments, boiling surfaces and flow conditions. Dedicated correlations are hardly precise outside of their establishment databases. However, it remains the best yet only way to compute N_{sit} . In that regard, the NSD correlation of Li *et al.* appears to be the most coherent choice.

7.6 CONSIDERATIONS ON BUBBLE INTERACTION AND NUCLEATION SITES DEACTIVATION

NSD correlation actually compute the total number of sites where bubbles can nucleate on a surface. However, they do not represent how important a nucleation site will be in term of bubbles generation compared to another.

In fact, Kossolapov has observed that each nucleation site has its own bubble nucleation frequency. Thus implying that some sites play a much greater role in wall nucleation compared to others. One can even consider that some nucleation sites can be neglected regarding their small impact on the whole phase change process.

In order to physically take into account this effect, Gilman considered a statistical approach, by assuming that nucleation site are randomly distributed over the heater surface (Complete Spatial Randomness). Then, considering that a nucleation site located under a bubble will be deactivated, one can express the number of sites actually contributing to bubble nucleation $N_{sit,a}$ as :

$$N_{sit,a} = (1 - \mathcal{P}) N_{sit}, \text{ with } \mathcal{P} = 1 - e^{-N_b \pi (D_b/2)^2} \quad (7.30)$$

where $N_b = t_g f N_{sit}$ is the actual average density of bubbles on the heater surface.

The resulting number of sites is a solution of the implicit equation on N_{sit} , which can be solved numerically or using the Lambert function (reciprocal of $w \rightarrow we^{-w}$).

Je vais détailler un peu plus cela avec des schémas clairs, ainsi qu'un exemple de comment cela pondère la densité de site totale, puisque cela permet d'éviter la divergence dans une loi telle que celle de Hibiki & Ishii à haute surchauffe pariétale

7.6.1 Static suppression

If we suppose that the nucleation sites follow a homogeneous spatial Poisson process with an event density λ , we can express the probability of finding n sites within an area A as :

$$\mathcal{P}(N(A) = n) = \frac{(\lambda A)^n}{n!} e^{-\lambda A} \quad (7.31)$$

If we consider the actual number of bubble-generating sites N_b , those sites are holding a bubble over a fraction $t_g f$ of the nucleation cycles in average. Thus, the actual density of bubbles held by the sites is : $t_g f N_b$. To derive N_b from the value N_{sit} provided by NSD correlations, we have to evaluate the probability of nucleation site overlapping, which corresponds to a distance r lower than R_d between two bubbles.

$$\mathcal{P}(r \leq R_d) = 1 - \mathcal{P}(N(\pi R_d^2) = 0) \quad (7.32)$$

$$= 1 - e^{-N_b t_g f \pi R_d^2} = \mathcal{P} \quad (7.33)$$

This probability thus represents the proportion of bubble that can't be geometrically accomodated on the surface. We can then evaluate N_b from N_{sit} as :

$$N_b = (1 - \mathcal{P}) N_{sit} \quad (7.34)$$

$$\Leftrightarrow N_b t_g f \pi R_d^2 e^{N_b t_g f \pi R_d^2} = N_{sit} t_g f \pi R_d^2 \quad (7.35)$$

$$\Leftrightarrow N_b = \frac{\mathcal{W}(N_{sit} \mathbf{A})}{\mathbf{A}} \quad \text{where } \mathbf{A} = t_g f \pi R_d^2 \quad (7.36)$$

7.6.2 Static coalescence

Now that the actual number of bubble-generating sites have been identified, we can consider other interaction phenomena that can occur on the boiling surface. For instance, if two sites are simultaneously

generating a bubble at a distance d between R_d and $2R_d$, the bubbles will coalesce while growing up to the detachment diameter. To estimate the probability of having a bubble on a site in this distance range, we consider the probability density function of the nearest-neighbour in the case of a homogeneous spatial Poisson process f with an event density λ .

$$f(r) = 2\lambda\pi r e^{-\lambda\pi r^2} \quad (7.37)$$

The considered probability of interaction is then :

$$\mathcal{P}(R_d \leq r \leq 2R_d) = \int_{R_d}^{2R_d} f(r) dr \quad (7.38)$$

$$= e^{-\lambda\pi R_d^2} - e^{-4\lambda\pi R_d^2} \quad (7.39)$$

$$= e^{-\lambda\pi R_d^2} \left[1 - \left(e^{-\lambda\pi R_d^2} \right)^3 \right] \quad (7.40)$$

$$= \mathcal{P}_{coal,st} \quad \text{with } \lambda = t_g f N_b \quad (7.41)$$

The density of bubble-generating sites that will lead to a static coalescence can then be estimated as :

$$N_{coal,st} = \mathcal{P}_{coal,st} N_b \quad (7.42)$$

If we suppose that coalescing bubbles will instantly lift-off due to the perturbation associated with the coalescence process, this yields an associated boiling flux :

$$\phi_{e,coal,st} = N_{coal,st} f \rho V h_{LV} \frac{4}{3} \pi R_{coal,st}^3 \quad \text{where } R_{coal,st} = \sqrt[3]{2} R_d \quad (7.43)$$

considering that the bubbles will merge approximately at $R = R_d$.

7.6.3 Sliding coalescence

Now that suppressed sites and sites that will lead to static coalescence have been identified, the remaining sites $N_{sl} = (1 - \mathcal{P}_{coal,st}) N_b$ will generate sliding bubbles. While sliding, a single bubble swipes an area :

$$A_{sl,1b} \approx l_{sl,1b} \frac{D_d + D_{lo}}{2} \quad (7.44)$$

In this area, there are an average number of bubble-generating sites $N_b A_{sl,1b}$ and an average number of growing bubbles on their sites $t_g f N_b A_{sl,1b}$

Two situations can happen from the sliding process :

- The bubble slides without coalescing
- The bubble coalesces while sliding with a bubble growing on its site and lifts-off

Following the same approach from the static suppression, we can estimate the probability of finding no growing bubble over the sliding surface :

$$\mathcal{P}(N(A_{sl,1b}) = 0) = e^{-N_b t_g f A_{sl,1b}} \quad (7.45)$$

Thus, if a sliding bubble among the N_{sl} does not encounter any growing bubble, the sites on its sliding area will be wiped and thus be quenched by cold liquid. This means that those sites will be suppressed due to the sliding of other bubbles over them.

Among the N_b bubble generating sites we can identify 4 categories of sites :

- Sites generating bubbles which will slide without encountering any growing bubble on their path :

$$N_{sl,NC} = N_{sl} e^{-f t_g N_b A_{sl,1b}}$$

- Sites generating bubbles that will coalesce with a growing bubble during sliding :

$$N_{sl,C} = N_{sl} \left(1 - e^{-ft_g N_b A_{sl,1b}} \right)$$

- Sites which will be suppressed by bubbles sliding without coalescing :

$$N_{sup,sl} = N_{sl,NC} N_b A_{sl,1b}$$

- Sites generating bubbles that will coalesce with a sliding bubble coming from upstream. Those bubbles are still in the growing phase up to detachment when they are coalescing with sliding bubbles. Therefore, there are equal to the number of sliding bubbles that will coalesce :

$$N_{g,C} = N_{sl,C}$$

This allows to finally write :

$$N_b = N_{sl,NC} + N_{sl,C} + N_{sup,sl} + N_{g,C} \quad (7.46)$$

$$= N_{sl} \left[2 - e^{-ft_g N_b A_{sl,1b}} (A_{sl,1b} N_b - 1) \right] \quad (7.47)$$

Which finally yields the total number of sliding bubbles :

$$N_{sl} = \frac{N_b}{2 - e^{-ft_g N_b A_{sl,1b}} (A_{sl,1b} N_b - 1)} \quad (7.48)$$

8

ASSEMBLING A NEW HEAT FLUX PARTITIONING MODEL

8.1 GENERAL DESCRIPTION OF THE MODEL

The main goal of such a model is to provide a way to compute the wall temperature T_w resulting from the applied wall heat flux ϕ_w , or the other way around.

In order to try to be as extensive as possible regarding the different heat transfer mechanisms at stake, the wall heat flux is supposed to be split between 4 different contributions (Figure 8.1) :

- A convective heat flux towards the liquid phase, unaffected by the presence of bubbles on the heater surface : $\phi_{c,l}$
- A boiling heat flux, representing the energy removed from the wall to grow a bubble up to its lift-off diameter : ϕ_b
- A quenching heat flux, accounting for transient heat transfer to the liquid phase when bubbles slide or lift-off from the wall : ϕ_q
- A convective heat flux towards the vapor phase, representing the heat transfer occurring through the dry areas of the surface beneath the bubbles : $\phi_{c,v}$

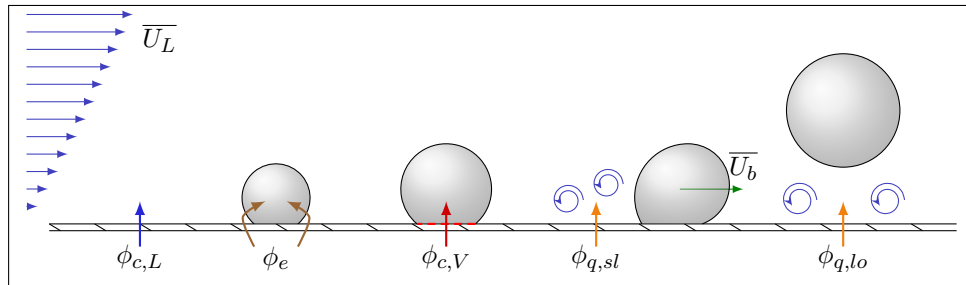


Figure 8.1: Sketch of the considered HFP

The supposed mechanisms yields the total wall heat flux partitioning (8.1) :

$$\phi_w = \phi_{c,l} + \phi_e + \phi_q + \phi_{c,v} \quad (8.1)$$

In the following subsections, we focus our analysis on each term to detail its modeling.

8.1.1 Convective heat fluxes

The convective heat fluxes towards the liquid phase $\phi_{c,l}$ and the vapor phase $\phi_{c,v}$ can be written using an associated heat transfer coefficient (8.2) :

$$\phi_{c,l} = a_{c,l} h_{c,l} (\textcolor{red}{T}_w - \textcolor{blue}{T}_l) \quad \text{and} \quad \phi_{c,v} = a_{c,v} h_{c,v} (\textcolor{red}{T}_w - \textcolor{blue}{T}_v) \quad (8.2)$$

8.1.2 Boiling heat flux

The total energy associated with the nucleation of a bubble with a volume V_b can be expressed as $V_b \rho_v h_{lv}$. If one knows the nucleation frequency f at which bubbles are generated along with the nucleation site density on the heater surface N_{sit} , the resulting heat flux associated with the nucleation phenomenon can thus be written as (8.3) :

$$\phi_b = N_{sit} f V_b \rho_v h_{lv} \quad (8.3)$$

8.1.3 Quenching heat flux

The quenching heat flux accounts for the transient heat transfer which occurs when cold liquid is brought close to the wall when a bubble slides or lifts-off, thus disrupting the previously established thermal boundary layer.

DEL VALLE & KENNING have supposed that this kind phenomenon can be represented as a semi-infinite transient heat transfer between the liquid at T_l and the wall at T_w . Solving the conductive heat transfer problem yields an instantaneous heat flux expressed as Eq. 8.4.

$$\phi_q(t) = \frac{\lambda_l (\textcolor{red}{T}_w - \textcolor{blue}{T}_l)}{\sqrt{\pi \eta_l t}} \quad (8.4)$$

Therefore, we can average this heat flux over a time t_w , during which the quenching operates, and ponderating it both by the portion of the affected heater area a_q and the fraction of quenching time over a total bubble nucleation cycle $t_w f$, yielding :

$$\phi_q = \textcolor{brown}{a}_q \textcolor{blue}{t}_w f \frac{1}{\textcolor{blue}{t}_w} \int_0^{\textcolor{blue}{t}_w} \frac{\lambda_l (\textcolor{red}{T}_w - \textcolor{blue}{T}_l)}{\sqrt{\pi \eta_l t}} dt = \textcolor{brown}{a}_q \textcolor{blue}{t}_w f \frac{2 \lambda_l (\textcolor{red}{T}_w - \textcolor{blue}{T}_l)}{\sqrt{\pi \eta_l \textcolor{blue}{t}_w}} \quad (8.5)$$

8.1.4 Needed closure relationships

After expressing each heat flux components of the global partitioning, the resulting formulations yields a first list of parameters for which closure relationships (or at least precise definition) are needed. Terms previously highlighted in orange will be given a specific definition, terms in blue require a closure law, wall temperature is indicated in red.

The different terms needing further development are listed below :

- The fractions of the heater area ponderating convective and quenching heat transfers : $a_{c,l}$, $a_{c,v}$ and $a_q(??)$
- The convective heat transfer coefficients : $h_{c,l}$ and $h_{c,v}$ (Section ??)
- The nucleation site density over the heater surface : N_{sit} (Section : ??)
- The nucleation frequency, which includes both the growth time t_g (Section ??) of a bubble and the waiting time t_w (Je dois encore proposer une modélisation pour t_w , à discuter) : $f = 1 / (t_g + t_w)$
- The total bubble volume V_b (??) generated until its lift-off, thus including the modeling of the bubble lift-off diameter : D_{lo}
- The phases temperature : T_l (??) and T_v (??)

Part IV
TOWARDS THE INDUSTRIAL GEOMETRY

PROMOTEUR

9.1 BOILING FREON IN A TUBE WITH MIXING VANES : DEBORA-PROMOTEUR EXPERIMENTS

In this section, we simulate upward boiling flows of R12 in a vertical tube equipped with mixing vanes and compare the outlet void fraction profile predicted by NEPTUNE_CFD with measurements coming from the DEBORA-Promoteur experiment.

9.1.1 Description of the experiment

In 2003, the wish to investigate boiling flows in complex geometries similar to those in PWR fuel assembly lead CEA and EDF to modify the DEBORA facility to introduce mixing vanes (MV) within the tube. This mixing device has been designed to have the same geometric properties as the mixing vanes attached to rod bundle grids (Figure 9.1).

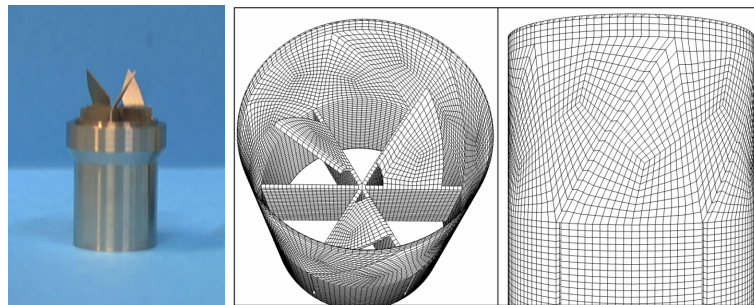


Figure 9.1: Picture of the mixing device (left) and its fine meshing (right).

Two series of measurements were conducted on this geometry :

- Campaign 4800 : measurements of α using two optical probes, mixing device placed $0.455m \approx 23.5D_h$ upstream the end of the heating length
- Campaign 5200 : measurements of α and $U_{G,z}$ using two optical probes, mixing device placed $0.192m \approx 10D_h$ upstream the end of the heating length

The goal of those tests was to observe the impact of the mixing device on the void fraction profile. The induced rotation is expected to gather the bubbles at the center of the tube and enhance condensation for highly subcooled cases. Those expectations are confirmed when looking at experimental α profiles on Figure 9.2. The strong differences compared to simple tube profiles could explain the gain on the CHF value in PWR thanks to the mixing grids. Cases are named following the same nomenclature as presented in Section ??.

9.1.2 Analysis of the Experimental Measurements

ESTIMATION OF BUBBLE DIAMETER USING AGATE PROM MEASUREMENTS OF URAD

9.1.3 NEPTUNE_CFD simulations of DEBORA-Promoteur cases

We simulated 3 cases for each position of the mixing device, covering different local thermodynamic quality near the vanes ($x_{eq,MV}$) :

- 48G3P26W23Te65 & 52G3P26W23Te65 with $x_{eq,MV} \approx -1\%$
- 48G3P26W23Te69 & 52G3P26W23Te69 with $x_{eq,MV} \approx 4\%$
- 48G3P26W23Te75 & 52G3P26W23Te75 with $x_{eq,MV} \approx 12\%$

Computations are conducted using two meshes for Te69 cases : a large one (M1) with 444 703 cells and a fine one (M2) with 3 487 627 cells. Results for void fraction profiles are shown on Figure 9.2.

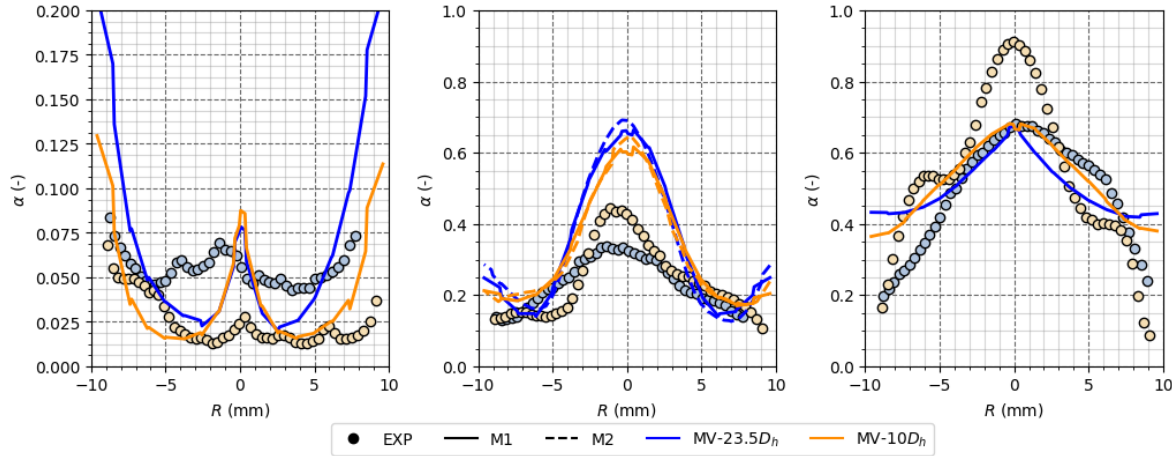


Figure 9.2: NCFD (lines) vs. Exp. (circles) - α profiles for two MV positions ($23.5D_h$ in blue, $10D_h$ in orange)
- $T_{in} = 65^\circ\text{C}$ (left), $T_{in} = 69^\circ\text{C}$ (middle), $T_{in} = 75^\circ\text{C}$ (right) - Simulations using two meshes M1 (coarse) and M2 (fine) for $T_{in} = 69^\circ\text{C}$.

Quantitatively speaking, it seems that NEPTUNE_CFD reproduces the effect of vapor accumulation at the center thanks to the pressure gradient generated by the swirl induced by the mixing vanes. The radial position of the core void fraction peak correctly matches the experimental one.

However, measured void fraction profiles are not predicted correctly. A particularly strong overestimation of the core void fraction is observed as well as close to the wall. The CMFD results tend to rapidly reach a core void fraction around 60% ($T_{in} = 69^\circ\text{C}$ cases) and then flattens with increasing temperature ($T_{in} = 75^\circ$ cases). This contradicts experimental observation where the void fraction profile globally rises when inlet temperature increases, except at the wall where no peak is observed due to bubble removing effect by the liquid's rotation. Moreover, the $T_{in} = 75^\circ$ case with MV at $10D_h$ experimentally shows local α peaks at $R \approx \pm 6\text{mm}$ which remain currently unexplained and not reproduced by the simulations.

To investigate what could be a potential origin for the core void fraction peak overestimation, we present in Section 9.2 single-phase flow simulations in the MV geometry.

9.2 LIQUID WATER FLOW IN A TUBE WITH MIXING VANES : AGATE-PROMOTEUR EXPERIMENT

In this penultimate section, we briefly investigate single-phase flow within the same geometry as Section 9.1.

9.2.1 Description of the experiment

In 2003, using the same experimental geometry as DEBORA-Promoteur cases (Section 9.1), Laser Doppler Velocimetry (LDV) measurements of velocity and turbulent fluctuations for an adiabatic single-phase flow of water were conducted. The outlet pressure was around $P = 2$ bar with an inlet mass flux $G \approx 3000 \text{ kg/m}^2/\text{s}$. Measurements were conducted on 6 different diameters and repeated at various axial positions upstream and downstream the mixing vanes.

A first look at experimental measurements (Figure 9.3) shows that the vanes geometry induces significantly non-symmetric velocity profile. Moreover, we observe high turbulent fluctuations which maximum is located at the same radial position as the maximum radial velocity gradient.

9.2.2 NEPTUNE_CFD simulations of AGATE-Promoteur case

On Figure 9.3, we present some of the results obtained with NEPTUNE_CFD using the $R_{ij} - \varepsilon$ SSG turbulence model on the M2 mesh, along with a smooth wall law and a rough wall law (roughness $\epsilon = 0.01\text{mm}$). The turbulent fluctuations Root Mean Square (RMS) correspond, for instance, to $\sqrt{\langle u_x'^2 \rangle}$ for the x direction where u_i' represents the fluctuating part of the velocity along component i and $\langle \cdot \rangle$ the time-averaging operator. Subscripts R and A stand for radial and axial values ; U_0 is the average inlet velocity.

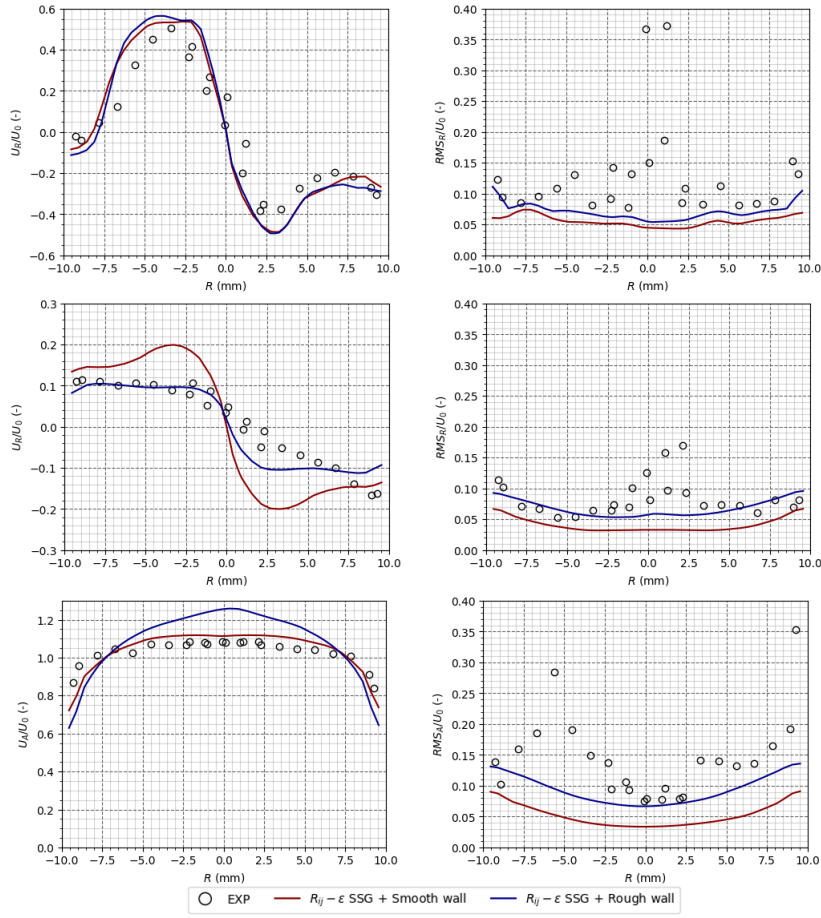


Figure 9.3: NCFD vs. Exp. - Top & Middle : Radial velocity and turbulent RMS ($z = 30\text{mm}$ & $z = 440\text{mm}$) - Bottom : Axial velocity and turbulent RMS ($z = 440\text{mm}$).

Non-symmetric radial velocity profiles close to the MV are quite well reproduced by the simulations. However, far downstream the MV, it appears that the fluid's rotation is overestimated by the model with a smooth wall approach, while applying a roughness helps to reduce the magnitude of the swirl. Moreover, the radial turbulent fluctuations are better estimated by the rough wall approach at $z = 440\text{ mm}$. On the other hand, it seems that the rough wall approach deteriorates the axial velocity profile compared to the experiment. As shown on the bottom part of Figure 9.3, the smooth wall simulation returns a flat velocity profile closer to the experiment than the rough wall one which overestimates the core velocity peak.

Both simulations globally underestimate the turbulent fluctuations, which can have a significant influence over the observed discrepancies on velocity profiles since turbulence plays a key role to homogenize the fluid flow.

Those results finally highlight the fact that simulation of such rotating flows may need a particular wall approach to better capture the induced swirl and its dissipation. Correct prediction of turbulent

fluctuations would be of significant interest to ensure liquid velocity validation. Further investigations on boiling cases could possibly be improved by a roughness approach, which is the current correction used for two-phase wall laws (Subsection 1.6).

Part V
CONCLUSION

Part VI
APPENDIX

A

DETAILS ON THE BUBBLE GROWTH CALCULATION

To further study the bubble growth process, we will try to derive an analytic In this section, computations are conducted using the spherical coordinates $(\bar{e}_r, \bar{e}_\theta, \bar{e}_\varphi)$ with coordinates (r, θ, ϕ) .

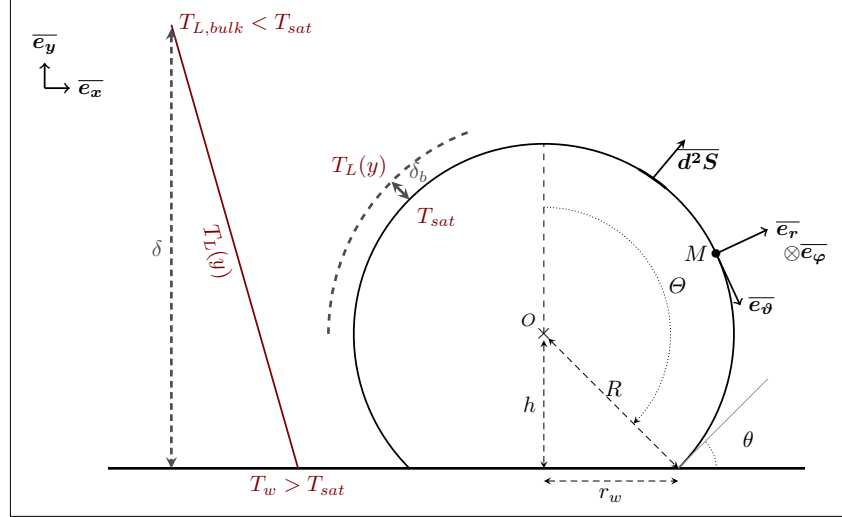


Figure A.1: Studied geometry

Geometrical definitions :

- $\Theta = \pi - \theta$ the angular portion of the truncated sphere in spherical coordinates ;
- $r_w = R\sin(\theta) = -R\sin(\Theta)$ the bubble foot radius ;
- $h = R\cos(\theta) = -R\cos(\Theta)$ the distance between the wall and the center of the bubble (> 0 if $\theta < \pi/2$, < 0 otherwise) ;
- R and $V = \frac{4}{3}\pi R^3 f_V(\theta)$ the radius and the volume of the bubble ;
- $\bar{d}^2 S = R^2 \sin(\theta) d\theta d\varphi \bar{e}_r$ the surface vector in spherical coordinates ;
- $y = R\cos(\theta) + h = R(\cos(\theta) - \cos(\Theta))$ the distance to the wall in cartesian coordinates.

Thermal-hydraulics definitions :

- $\Delta T_L = T_{sat} - T_\infty$ et $\Delta T_w = T_w - T_{sat}$ the subcooling of the liquid and the wall superheat respectively ;
- δ et δ_b the flow boundary layer thickness and the bubble boundary layer thickness respectively ;
- $d^2 Q_b$ the heat received by the bubble between t and $t + dt$ through the surface $d^2 S$;
- $\lambda, \rho, c_p, \eta, h$ the thermal conductivity, density, heat capacity, thermal diffusivity and mass enthalpy respectively (l standing for liquid and g for gas) ;

- $\text{Ja}_w = \Delta T_w \rho_L c_{p,L} / (h_{LV} \rho_V)$ the wall superheat (or boiling) Jakob number and $\text{Ja}_L = \Delta T_L \rho_L c_{p,L} / (h_{LV} \rho_V)$ the subcooled liquid (or condensation) one.

The thermal boundary layer of the flow is assumed to follow a linear profile, giving the expression :

$$T_l(y) = T_w + \frac{T_\infty - T_w}{\delta} y \quad (\text{A.1})$$

If we consider that the bubble stays at a temperature close to T_{sat} , the radial component of the temperature gradient at the bubble's interface yields :

$$\bar{\nabla}(T) \cdot \bar{er} = \frac{\partial T}{\partial r}(R, \theta, \phi) \approx \frac{T_l(y) - T_{sat}}{\delta_b} \quad (\text{A.2})$$

Applying Fourier's law to the liquid close to the bubble : $\bar{j_Q} = -\lambda_l \bar{\nabla}(T)$, then the bubble receives between t and $t + dt$ through d^2S :

$$d^2Q_b = \bar{j_Q} \cdot (-\bar{d^2S}) \quad (\text{A.3})$$

$$= \lambda_l \frac{\partial T}{\partial r}(R, \theta, \varphi) R^2 \sin(\theta) d\theta d\varphi \quad (\text{A.4})$$

$$\approx \lambda_l \frac{T_l(y) - T_{sat}}{\delta_b} R^2 \sin(\theta) d\theta d\varphi \quad (\text{A.5})$$

$$= \lambda_l \frac{1}{\delta_b} \left[T_w + \frac{T_\infty - T_w}{\delta} y - T_{sat} \right] R^2 \sin(\theta) d\theta d\varphi \quad (\text{A.6})$$

$$= \frac{\lambda_l}{\delta_b} \left[\Delta T_w - \frac{\Delta T_w + \Delta T_l}{\delta} R [\cos(\theta) - \cos(\Theta)] \right] R^2 \sin(\theta) d\theta d\varphi \quad (\text{A.7})$$

$$= \frac{\lambda_l}{\delta_b} \left[\Delta T_w R^2 \sin(\theta) - \frac{\Delta T_w + \Delta T_l}{\delta} R^3 [\cos(\theta) - \cos(\Theta)] \sin(\theta) \right] d\theta d\varphi \quad (\text{A.8})$$

The total heat flux received by the bubble can then be derived, supposing that δ_b is constant all around the bubble between t and $t + dt$:

$$Q_b = \int_{\varphi=0}^{\varphi=2\pi} \int_{\theta=0}^{\Theta} d^2Q_b \quad (\text{A.9})$$

$$= \frac{2\pi\lambda_l}{\delta_b} \left[\int_0^\Theta \Delta T_w R^2 \sin(\theta) d\theta + \int_0^\Theta \frac{\Delta T_w + \Delta T_l}{\delta} R^3 \cos(\Theta) \sin(\theta) d\theta - \int_0^\Theta \frac{\Delta T_w + \Delta T_l}{\delta} R^3 \cos(\theta) \sin(\theta) d\theta \right] \quad (\text{A.10})$$

$$= \frac{2\pi\lambda_l}{\delta_b} \left[\Delta T_w R^2 (1 - \cos(\Theta)) + \frac{\Delta T_w + \Delta T_l}{\delta} R^3 \left[\cos(\Theta) (1 - \cos(\Theta)) - \frac{1}{4} (1 - \cos(2\Theta)) \right] \right] \quad (\text{A.11})$$

$$= \frac{2\pi\lambda_l R^2}{\delta_b} \left[\frac{-R}{2\delta} (\Delta T_w + \Delta T_l) (1 + 2\cos(\alpha) + \cos^2(\alpha)) + \Delta T_w (1 + \cos(\alpha)) \right] \quad (\text{A.12})$$

$$= \frac{2\pi\lambda_l R^2}{\delta_b} (1 + \cos(\alpha)) \left[\Delta T_w - \frac{R}{2\delta} (\Delta T_w + \Delta T_l) (1 + \cos(\alpha)) \right] \quad (\text{A.13})$$

Between t and $t + dt$, the bubble receives a $Q_b dt$ energy amount through thermal diffusion. Assuming this energy solely contributes to evaporation of the surrounding liquid, the resulting mass of generated vapor is :

$$dm_g = \rho_g dV = \frac{Q_b dt}{h_{lg}} \quad (\text{A.14})$$

$$\text{then } \frac{dV}{dt} = \frac{Q_b}{\rho_g h_{lg}} \quad (\text{A.15})$$

Since $V = \frac{4}{3}\pi R^3 f_V(\alpha)$, we can write :

$$\frac{dV}{dt} = \frac{4}{3}\pi f_V(\alpha) 3R^2 \frac{dR}{dt} \quad (\text{A.16})$$

Then :

$$\frac{dR}{dt} = \frac{1}{4\pi R^2 f_V(\alpha)} \frac{1}{\rho_g h_{lg}} \frac{2\pi \lambda_l R^2}{\delta_b} (1 + \cos(\alpha)) \left[\Delta T_w - \frac{R}{2\delta} (\Delta T_w + \Delta T_l) (1 + \cos(\alpha)) \right] \quad (\text{A.17})$$

$$= \frac{1}{2f_V(\alpha)} \frac{\Delta T_w}{h_{lg} \rho_g} \frac{\lambda_l}{\delta_b} (1 + \cos(\alpha)) \left[1 - \frac{R}{2\delta} \left(1 + \frac{\Delta T_l}{\Delta T_w} \right) (1 + \cos(\alpha)) \right] \quad (\text{A.18})$$

$$= \frac{\text{Ja}_w \eta_l}{2\delta_b f_V(\alpha)} (1 + \cos(\alpha)) \left[1 - \frac{R}{2\delta} \left(1 + \frac{\text{Ja}_l}{\text{Ja}_w} \right) (1 + \cos(\alpha)) \right] \quad (\text{A.19})$$

If we define :

$$a = \frac{\text{Ja}_w \eta_l}{4\delta_b \delta f_V(\alpha)} \left(1 + \frac{\text{Ja}_l}{\text{Ja}_w} \right) (1 + \cos(\alpha))^2 \quad \text{et} \quad b = \frac{\text{Ja}_w \eta_l}{2\delta_b f_V(\alpha)} (1 + \cos(\alpha)) \quad (\text{A.20})$$

Finally :

$$\frac{dR}{dt} + aR = b \quad (\text{A.21})$$

Solutions of this differential equation depend on the hypothesis over δ and δ_b . In a first approach, we will consider that δ does not vary during the whole bubble growth. This thickness could be expressed using boundary layer thickness correlations for example (laminar or turbulent depending on the Reynolds number).

On the other hand, we will consider 3 different choices to model δ_b :

A.0.1 Case 1 : δ_b is constant

This is a **strong assumption** since it means that δ_b does not depend on the temperature and the flow shear rate facing the bubble. In this case, a and b are constant, giving :

$$\frac{dR}{dt} + aR = b \quad (\text{A.22})$$

With the initial condition $R(t = 0) = 0$ the solution of this differential equation is :

$$R(t) = \frac{b}{a} (1 - e^{-at}) \quad \text{where} \quad \frac{b}{a} = \frac{2\delta}{\left(1 + \frac{\text{Ja}_l}{\text{Ja}_w} \right) (1 + \cos(\alpha))} = R_\infty \quad \text{is the final bubble equilibrium radius.} \quad (\text{A.23})$$

A.0.2 Case 2 : $\delta_b = \sqrt{\eta_l t}$

This expression derives from the growth of a boundary layer through pure diffusion, as studied by LEGENDRE *et al.*

Such a boundary layer thickness is also used when one writes the quenching heat flux (see Section 8.1 and DEL VALLE & KENNING work).

In this case, this means that the boundary layer around the bubble interface grows through diffusion only.

Thus, it yields :

$$\frac{dR}{dt}(t) + a(t)R(t) = b(t) \quad (\text{A.24})$$

$$a(t) = \frac{\text{Ja}_w \sqrt{\eta_l}}{4\delta f_V(\alpha) \sqrt{t}} \left(1 + \frac{\text{Ja}_l}{\text{Ja}_w}\right) (1 + \cos(\alpha))^2 = K_a t^{-1/2} \text{ and } b(t) = \frac{\text{Ja}_w \sqrt{\eta_l}}{2f_V(\alpha) \sqrt{t}} (1 + \cos(\alpha)) = K_b t^{-1/2} \quad (\text{A.25})$$

With the initial condition $R(t=0) = 0$, the solution is given by :

$$R(t) = R_\infty \left(1 - e^{-2K_a \sqrt{t}}\right) \text{ avec } R_\infty = \frac{K_b}{K_a} \quad (\text{A.26})$$

A.0.3 Case 3 : $\delta_b = CR$

In this last case, the bubble boundary layer is assumed to be proportional to the bubble radius R , through a constant coefficient C . This yields :

$$a(t) = \frac{\text{Ja}_w \eta_l}{4\delta f_V(\alpha) CR(t)} \left(1 + \frac{\text{Ja}_l}{\text{Ja}_w}\right) (1 + \cos(\alpha))^2 = K'_a \frac{1}{R(t)} \text{ et } b(t) = \frac{\text{Ja}_w \eta_l}{2f_V(\alpha) CR(t)} (1 + \cos(\alpha)) = K'_b \frac{1}{R(t)} \quad (\text{A.27})$$

Giving :

$$\frac{dR}{dt}(t) + K'_a R(t) = K'_b \frac{1}{R(t)} \quad (\text{A.28})$$

Which the solution with the initial condition $R(t=0) = 0$ is :

$$R(t) = R_\infty \left(W\left(-e^{-tK'_a^2/K'_b - 1}\right) + 1\right) \quad (\text{A.29})$$

With W being the LAMBERT function defined as the reciprocal function of $w \rightarrow we^w$ on \mathbb{C} .

B

DETAILS ON THE BUBBLE FORCE BALANCE

Aliquam lectus. Vivamus leo. Quisque ornare tellus ullamcorper nulla. Mauris porttitor pharetra tortor. Sed fringilla justo sed mauris. Mauris tellus. Sed non leo. Nullam elementum, magna in cursus sodales, augue est scelerisque sapien, venenatis congue nulla arcu et pede. Ut suscipit enim vel sapien. Donec congue. Maecenas urna mi, suscipit in, placerat ut, vestibulum ut, massa. Fusce ultrices nulla et nisl. Etiam ac leo a risus tristique nonummy. Donec dignissim tincidunt nulla. Vestibulum rhoncus molestie odio. Sed lobortis, justo et pretium lobortis, mauris turpis condimentum augue, nec ultricies nibh arcu pretium enim. Nunc purus neque, placerat id, imperdiet sed, pellentesque nec, nisl. Vestibulum imperdiet neque non sem accumsan laoreet. In hac habitasse platea dictumst. Etiam condimentum facilisis libero. Suspendisse in elit quis nisl aliquam dapibus. Pellentesque auctor sapien. Sed egestas sapien nec lectus. Pellentesque vel dui vel neque bibendum viverra. Aliquam porttitor nisl nec pede. Proin mattis libero vel turpis. Donec rutrum mauris et libero. Proin euismod porta felis. Nam lobortis, metus quis elementum commodo, nunc lectus elementum mauris, eget vulputate ligula tellus eu neque. Vivamus eu dolor.

$$r_w = \frac{1}{2} (\sin(\theta_d) R + \sin(\theta_u) R) \quad (B.1)$$

$$= \frac{R}{2} (\sin(\theta_s + d\theta) + \sin(\theta - d\theta)) \quad (B.2)$$

$$= \frac{R}{2} \left[2\sin\left(\frac{\theta_s + d\theta + \theta_s - d\theta}{2}\right) \cos\left(\frac{\theta_s + d\theta - (\theta_s - d\theta)}{2}\right) \right] \quad (B.3)$$

$$= R\sin(\theta_s) \cos(d\theta) \quad (B.4)$$

$$\overline{F_{CP}} = \frac{2\sigma}{R_c} \frac{\pi d_w^2}{4} \overline{e_y} \quad (B.5)$$

$$= \frac{2\sigma}{R} \frac{\pi 4R^2}{4} \sin^2(\theta) \cos^2(d\theta) \overline{e_\perp} \quad (B.6)$$

$$= 2\sigma\pi R \underbrace{\sin^2(\theta) \cos^2(d\theta)}_{f_{cp}} \overline{e_\perp} \quad (B.7)$$

$$= 2\pi R\sigma f_{cp}(\theta, d\theta) \overline{e_\perp} \quad (B.8)$$

$$\overline{F_{CP}} \cdot \overline{e_\perp} = -d_w\sigma \frac{\pi}{\alpha_r - \alpha_u} (\cos(\alpha_a) - \cos(\alpha_r)) \quad (B.9)$$

$$= \pi 2R\sigma \frac{\sin(\alpha + d\alpha) + \sin(\alpha - d\alpha)}{2} \frac{\cos(\alpha + d\alpha) - \cos(\alpha - d\alpha)}{2d\alpha} \quad (B.10)$$

$$= 2\pi R\sigma \frac{2\sin(\alpha) \cos(d\alpha)}{2} \frac{(-2\sin(\alpha) \sin(d\alpha))}{2d\alpha} \quad (B.11)$$

$$= -2\pi R\sigma \underbrace{\sin^2(\alpha) \frac{\sin(2d\alpha)}{2d\alpha}}_{f_{s,\perp}} \quad (B.12)$$

$$= -2\pi R\sigma f_{s,\perp}(\alpha, d\alpha) \quad (B.13)$$

$$(B.14)$$

LABITUR BONORUM PRI NO	QUE VISTA	HUMAN
fastidii ea ius	germano	demonstratea
suscipit instructior	titulo	personas
quaestio philosophia	facto	demonstrated

Table B.1: Autem usu id.

$$\overline{F_s} \cdot \overline{e_{\parallel}} = -1.215d_w\sigma \frac{\pi(\alpha_r - \alpha_u)}{\pi^2 - (\alpha_r - \alpha_u)^2} (\sin(\alpha_r) + \sin(\alpha_u)) \quad (B.15)$$

$$= -1.215d_w\sigma \frac{\pi 2d\alpha}{\pi^2 - 4d\alpha^2} (\sin(\alpha + d\alpha) + \sin(\alpha - d\alpha)) \quad (B.16)$$

$$= -1.215 2R\sigma \frac{\pi d\alpha}{\pi^2 - 4d\alpha^2} (\sin(\alpha + d\alpha) + \sin(\alpha - d\alpha))^2 \quad (B.17)$$

$$= -2\pi R\sigma \frac{1.215d\alpha}{\pi^2 - 4d\alpha^2} 4\sin^2(\alpha) \cos^2(d\alpha) \quad (B.18)$$

$$= -2\pi R\sigma \underbrace{1.215 \frac{d\alpha}{(\frac{\pi}{2})^2 - d\alpha^2} \sin^2(\alpha) \cos^2(d\alpha)}_{f_{s,\parallel}} \quad (B.19)$$

$$= -2\pi R\sigma f_{s,\parallel}(\alpha, d\alpha) \quad (B.20)$$

B.1 APPENDIX SECTION TEST

Nulla in ipsum. Praesent eros nulla, congue vitae, euismod ut, commodo a, wisi. Pellentesque habitant morbi tristique senectus et netus et malesuada fames ac turpis egestas. Aenean nonummy magna non leo. Sed felis erat, ullamcorper in, dictum non, ultricies ut, lectus. Proin vel arcu a odio lobortis euismod. Vestibulum ante ipsum primis in faucibus orci luctus et ultrices posuere cubilia Curae; Proin ut est. Aliquam odio. Pellentesque massa turpis, cursus eu, euismod nec, tempor congue, nulla. Duis viverra gravida mauris. Cras tincidunt. Curabitur eros ligula, varius ut, pulvinar in, cursus faucibus, augue. Nulla mattis luctus nulla. Duis commodo velit at leo. Aliquam vulputate magna et leo. Nam vestibulum ullamcorper leo. Vestibulum condimentum rutrum mauris. Donec id mauris. Morbi molestie justo et pede. Vivamus eget turpis sed nisl cursus tempor. Curabitur mollis sapien condimentum nunc. In wisi nisl, malesuada at, dignissim sit amet, lobortis in, odio. Aenean consequat arcu a ante. Pellentesque porta elit sit amet orci. Etiam at turpis nec elit ultricies imperdiet. Nulla facilisi. In hac habitasse platea dictumst. Suspendisse viverra aliquam risus. Nullam pede justo, molestie nonummy, scelerisque eu, facilisis vel, arcu.

B.2 ANOTHER APPENDIX SECTION TEST

Curabitur tellus magna, porttitor a, commodo a, commodo in, tortor. Donec interdum. Praesent scelerisque. Maecenas posuere sodales odio. Vivamus metus lacus, varius quis, imperdiet quis, rhoncus a, turpis. Etiam ligula arcu, elementum a, venenatis quis, sollicitudin sed, metus. Donec nunc pede, tincidunt in, venenatis vitae, faucibus vel, nibh. Pellentesque wisi. Nullam malesuada. Morbi ut tellus ut pede tincidunt porta. Lorem ipsum dolor sit amet, consectetur adipiscing elit. Etiam congue neque id dolor. Donec et nisl at wisi luctus bibendum. Nam interdum tellus ac libero. Sed sem justo, laoreet vitae, fringilla at, adipiscing ut, nibh. Maecenas non sem quis tortor eleifend fermentum. Etiam id tortor ac mauris porta vulputate. Integer porta neque vitae massa. Maecenas tempus libero a libero posuere dictum. Vestibulum ante ipsum primis in faucibus orci luctus et ultrices posuere cubilia Curae; Aenean quis mauris sed elit commodo placerat. Class aptent taciti sociosqu ad litora torquent per comubia nostra, per inceptos hymenaeos. Vivamus rhoncus tincidunt libero. Etiam elementum pretium justo. Vivamus est. Morbi a tellus eget pede tristique commodo. Nulla nisl. Vestibulum sed nisl eu sapien cursus rutrum.

There is also a useless Pascal listing below: [Listing B.1](#).

Listing B.1: A floating example (`listings` manual)

```
1 for i:=maxint downto 0 do
begin
{ do nothing }
end;
```

BIBLIOGRAPHY

- [1] T. R. Auton. "The lift force on a spherical body in a rotational flow". In: *Journal of Fluid Mechanics* 183 (Oct. 1987). Publisher: Cambridge University Press, pp. 199–218. ISSN: 1469-7645, 0022-1120. DOI: [10.1017/S002211208700260X](https://doi.org/10.1017/S002211208700260X).
- [2] Mattia Bucci, Jacopo Buongiorno, and Matteo Bucci. "The not-so-subtle flaws of the force balance approach to predict the departure of bubbles in boiling heat transfer". In: *Physics of Fluids* 33.1 (Jan. 2021). Publisher: American Institute of Physics, p. 017110. ISSN: 1070-6631. DOI: [10.1063/5.0036956](https://doi.org/10.1063/5.0036956).
- [3] Lubomír Bureš and Yohei Sato. "On the modelling of the transition between contact-line and microlayer evaporation regimes in nucleate boiling". In: *Journal of Fluid Mechanics* 916 (June 2021). Publisher: Cambridge University Press. ISSN: 0022-1120, 1469-7645. DOI: [10.1017/jfm.2021.204](https://doi.org/10.1017/jfm.2021.204).
- [4] Deqi Chen, Liang-ming Pan, and Song Ren. "Prediction of bubble detachment diameter in flow boiling based on force analysis". In: *Nuclear Engineering and Design* 243 (Feb. 1, 2012), pp. 263–271. ISSN: 0029-5493. DOI: [10.1016/j.nucengdes.2011.11.022](https://doi.org/10.1016/j.nucengdes.2011.11.022).
- [5] Zhihao Chen, Atsushi Haginiwa, and Yoshio Utaka. "Detailed structure of microlayer in nucleate pool boiling for water measured by laser interferometric method". In: *International Journal of Heat and Mass Transfer* 108 (May 1, 2017), pp. 1285–1291. ISSN: 0017-9310. DOI: [10.1016/j.ijheatmasstransfer.2017.01.003](https://doi.org/10.1016/j.ijheatmasstransfer.2017.01.003).
- [6] Zhihao Chen, Xiaocheng Hu, Kang Hu, Yoshio Utaka, and Shoji Mori. "Measurement of the microlayer characteristics in the whole range of nucleate boiling for water by laser interferometry". In: *International Journal of Heat and Mass Transfer* 146 (Jan. 1, 2020), p. 118856. ISSN: 0017-9310. DOI: [10.1016/j.ijheatmasstransfer.2019.118856](https://doi.org/10.1016/j.ijheatmasstransfer.2019.118856).
- [7] Marco Colombo and Michael Fairweather. "Prediction of bubble departure in forced convection boiling: A mechanistic model". In: *International Journal of Heat and Mass Transfer* 85 (June 1, 2015), pp. 135–146. ISSN: 0017-9310. DOI: [10.1016/j.ijheatmasstransfer.2015.01.103](https://doi.org/10.1016/j.ijheatmasstransfer.2015.01.103).
- [8] M. G. Cooper and A. J. P. Lloyd. "The microlayer in nucleate pool boiling". In: *International Journal of Heat and Mass Transfer* 12.8 (Aug. 1, 1969), pp. 895–913. ISSN: 0017-9310. DOI: [10.1016/0017-9310\(69\)90154-9](https://doi.org/10.1016/0017-9310(69)90154-9).
- [9] Victor H. Del Valle and D. B. R. Kenning. "Subcooled flow boiling at high heat flux". In: *International Journal of Heat and Mass Transfer* 28.10 (Oct. 1, 1985), pp. 1907–1920. ISSN: 0017-9310. DOI: [10.1016/0017-9310\(85\)90213-3](https://doi.org/10.1016/0017-9310(85)90213-3).
- [10] Etienne Demarly. "A new approach to predicting departure from Nucleate Boiling (DNB) from direct representation of boiling heat transfer physics". Accepted: 2021-02-19T20:35:27Z ISBN: 9781237640528. Thesis. Massachusetts Institute of Technology, 2020.
- [11] G. Duhar, G. Riboux, and C. Colin. "Vapour bubble growth and detachment at the wall of shear flow". In: *Heat and Mass Transfer* 45.7 (May 1, 2009), pp. 847–855. ISSN: 1432-1181. DOI: [10.1007/s00231-007-0287-y](https://doi.org/10.1007/s00231-007-0287-y).
- [12] Géraldine Duhar. "Croissance et détachement de bulles en paroi d'un écoulement cisaillé : étude expérimentale de l'injection et de l'ébullition nucléée". These de doctorat. Toulouse, INPT, Jan. 1, 2003.
- [13] Géraldine Duhar and Catherine Colin. "Dynamics of bubble growth and detachment in a viscous shear flow". In: *Physics of Fluids* 18.7 (July 2006). Publisher: American Institute of Physics, p. 077101. ISSN: 1070-6631. DOI: [10.1063/1.2213638](https://doi.org/10.1063/1.2213638).
- [14] Carlos E. Estrada-Pérez, Yassin A. Hassan, Bandar Alkhudhiri, and Junsoo Yoo. "Time-resolved measurements of liquid–vapor thermal interactions throughout the full life-cycle of sliding bubbles at subcooled flow boiling conditions". In: *International Journal of Multiphase Flow* 99 (Feb. 1, 2018), pp. 94–110. ISSN: 0301-9322. DOI: [10.1016/j.ijmultiphaseflow.2017.10.002](https://doi.org/10.1016/j.ijmultiphaseflow.2017.10.002).
- [15] H. K. Forster and N. Zuber. "Growth of a Vapor Bubble in a Superheated Liquid". In: *Journal of Applied Physics* 25.4 (Apr. 1954). Publisher: American Institute of Physics, pp. 474–478. ISSN: 0021-8979. DOI: [10.1063/1.1721664](https://doi.org/10.1063/1.1721664).

- [16] W Frost, G. S Dzakowic, and American Society of Mechanical Engineers. An extension of the method for predicting flow boiling. OCLC: 459788171. New York, N.Y.: ASME, 1967.
- [17] J. Garnier, E. Manon, and G. Cubizolles. "LOCAL MEASUREMENTS ON FLOW BOILING OF REFRIGERANT 12 IN A VERTICAL TUBE". In: Multiphase Science and Technology 13.1 (2001). Publisher: Begel House Inc. ISSN: 0276-1459, 1943-6181. DOI: [10.1615/MultScienTechn.v13.i1-2.10](https://doi.org/10.1615/MultScienTechn.v13.i1-2.10).
- [18] C. W. M. van der Geld. "The dynamics of a boiling bubble before and after detachment". In: Heat and Mass Transfer 45.7 (May 1, 2009), pp. 831–846. ISSN: 1432-1181. DOI: [10.1007/s00231-007-0254-7](https://doi.org/10.1007/s00231-007-0254-7).
- [19] Peng Guan, Li Jia, Liaoifei Yin, and Zetao Tan. "Bubble departure size in flow boiling". In: Heat and Mass Transfer 51.7 (July 1, 2015), pp. 921–930. ISSN: 1432-1181. DOI: [10.1007/s00231-014-1461-7](https://doi.org/10.1007/s00231-014-1461-7).
- [20] Alexandre Guion, Shahriar Afkhami, Stéphane Zaleski, and Jacopo Buongiorno. "Simulations of microlayer formation in nucleate boiling". In: International Journal of Heat and Mass Transfer 127 (Dec. 1, 2018), pp. 1271–1284. ISSN: 0017-9310. DOI: [10.1016/j.ijheatmasstransfer.2018.06.041](https://doi.org/10.1016/j.ijheatmasstransfer.2018.06.041).
- [21] J. S. Hadamard. "Mouvement permanent lent d'une sphère liquide et visqueuse dans un liquide visqueux". In: Comptes Rendus Hebdomadaires des Séances de l'Académie des Sciences 155 (1911), pp. 1735–1738.
- [22] B. A Kader and A. M Yaglom. "Heat and mass transfer laws for fully turbulent wall flows". In: International Journal of Heat and Mass Transfer 15.12 (Dec. 1, 1972), pp. 2329–2351. ISSN: 0017-9310. DOI: [10.1016/0017-9310\(72\)90131-7](https://doi.org/10.1016/0017-9310(72)90131-7).
- [23] Satish G. Kandlikar and Mark E. Steinke. "Contact angles and interface behavior during rapid evaporation of liquid on a heated surface". In: International Journal of Heat and Mass Transfer 45.18 (Aug. 1, 2002), pp. 3771–3780. ISSN: 0017-9310. DOI: [10.1016/S0017-9310\(02\)00090-X](https://doi.org/10.1016/S0017-9310(02)00090-X).
- [24] J. F. Klausner, R. Mei, D. M. Bernhard, and L. Z. Zeng. "Vapor bubble departure in forced convection boiling". In: International Journal of Heat and Mass Transfer 36.3 (Feb. 1, 1993), pp. 651–662. ISSN: 0017-9310. DOI: [10.1016/0017-9310\(93\)80041-R](https://doi.org/10.1016/0017-9310(93)80041-R).
- [25] G. Kocamustafaogullari. "Pressure dependence of bubble departure diameter for water". In: International Communications in Heat and Mass Transfer 10.6 (Nov. 1, 1983), pp. 501–509. ISSN: 0735-1933. DOI: [10.1016/0735-1933\(83\)90057-X](https://doi.org/10.1016/0735-1933(83)90057-X).
- [26] L. D. Koffman and M. S. Plesset. "Experimental Observations of the Microlayer in Vapor Bubble Growth on a Heated Solid". In: Journal of Heat Transfer 105.3 (Aug. 1, 1983), pp. 625–632. ISSN: 0022-1481. DOI: [10.1115/1.3245631](https://doi.org/10.1115/1.3245631).
- [27] Ravikishore Kommajosyula. "Development and assessment of a physics-based model for subcooled flow boiling with application to CFD". Accepted: 2021-01-05T23:15:30Z. Thesis. Massachusetts Institute of Technology, 2020.
- [28] Artyom Kossolapov. "Experimental Investigation of Subcooled Flow Boiling and CHF at Prototypical Pressures of Light Water Reactors". PhD thesis. Massachusetts Institute of Technology, 2021.
- [29] Sir Horace Lamb. Hydrodynamics. Google-Books-ID: d_AoAAAAYAAJ. University Press, 1895. 632 pp. ISBN: 978-1-4086-1332-0.
- [30] Dominique Legendre, Jacques Borée, and Jacques Magnaudet. "Thermal and dynamic evolution of a spherical bubble moving steadily in a superheated or subcooled liquid". In: Physics of Fluids 10.6 (June 1998). Publisher: American Institute of Physics, pp. 1256–1272. ISSN: 1070-6631. DOI: [10.1063/1.869654](https://doi.org/10.1063/1.869654).
- [31] Dominique Legendre and Jacques Magnaudet. "The lift force on a spherical bubble in a viscous linear shear flow". In: Journal of Fluid Mechanics 368 (Aug. 1998). Publisher: Cambridge University Press, pp. 81–126. ISSN: 1469-7645, 0022-1120. DOI: [10.1017/S0022112098001621](https://doi.org/10.1017/S0022112098001621).
- [32] Octave Levenspiel. "Collapse of Steam Bubbles in Water". In: Industrial & Engineering Chemistry 51.6 (June 1, 1959). Publisher: American Chemical Society, pp. 787–790. ISSN: 0019-7866. DOI: [10.1021/ie50594a045](https://doi.org/10.1021/ie50594a045).

- [33] V. G. Levich. Physicochemical hydrodynamics. Prentice-Hall international series in the physical and chemical engineering sciences. OCLC: 1378432. Englewood Cliffs, N.J.: Prentice-Hall, 1962. 700 pp. ISBN: 978-0-13-674440-5.
- [34] J. Magnaudet and I. Eames. "The Motion of High-Reynolds-Number Bubbles in Inhomogeneous Flows". In: Annual Review of Fluid Mechanics 32.1 (2000). _eprint: <https://doi.org/10.1146/annurev.fluid.32.1.659>, pp. 659–708. DOI: [10.1146/annurev.fluid.32.1.659](https://doi.org/10.1146/annurev.fluid.32.1.659).
- [35] Sandipan Maity. "Effect of Velocity and Gravity on Bubble Dynamics". MSc Thesis. University of California Los Angeles, 2000.
- [36] Philippe (1970 March. "Caractérisation et modélisation de l'environnement thermohydraulique et chimique des gaines de combustible des réacteurs à eau sous pression en présence d'ébullition". These de doctorat. Aix-Marseille 1, Jan. 1, 1999.
- [37] T. Mazzocco, W. Ambrosini, R. Kommajosyla, and E. Baglietto. "A reassessed model for mechanistic prediction of bubble departure and lift off diameters". In: International Journal of Heat and Mass Transfer 117 (Feb. 1, 2018), pp. 119–124. ISSN: 0017-9310. DOI: [10.1016/j.ijheatmasstransfer.2017.09.105](https://doi.org/10.1016/j.ijheatmasstransfer.2017.09.105).
- [38] William H McAdams. Heat transmission. OCLC: 683455. New York: McGraw-Hill, 1954.
- [39] Renwei Mei and J. F. Klausner. "Shear lift force on spherical bubbles". In: International Journal of Heat and Fluid Flow 15.1 (Feb. 1, 1994), pp. 62–65. ISSN: 0142-727X. DOI: [10.1016/0142-727X\(94\)90031-0](https://doi.org/10.1016/0142-727X(94)90031-0).
- [40] Renwei Mei and James F. Klausner. "Unsteady force on a spherical bubble at finite Reynolds number with small fluctuations in the free-stream velocity". In: Physics of Fluids A: Fluid Dynamics 4.1 (Jan. 1992). Publisher: American Institute of Physics, pp. 63–70. ISSN: 0899-8213. DOI: [10.1063/1.858501](https://doi.org/10.1063/1.858501).
- [41] B. B Mikic, W. M Rohsenow, and P Griffith. "On bubble growth rates". In: International Journal of Heat and Mass Transfer 13.4 (Apr. 1, 1970), pp. 657–666. ISSN: 0017-9310. DOI: [10.1016/0017-9310\(70\)90040-2](https://doi.org/10.1016/0017-9310(70)90040-2).
- [42] Louis Melville Milne-Thomson. Theoretical Hydrodynamics. Google-Books-ID: A5hRAAAAMAAJ. Macmillan and Company, limited, 1938. 590 pp.
- [43] Tomio Okawa, Tatsuhiro Ishida, Isao Kataoka, and Michitsugu Mori. "Bubble rise characteristics after the departure from a nucleation site in vertical upflow boiling of subcooled water". In: Nuclear Engineering and Design. Festschrift Edition Celebrating the 65th Birthday of Prof. Richard T. Lahey, Jr. 235.10 (May 1, 2005), pp. 1149–1161. ISSN: 0029-5493. DOI: [10.1016/j.nucengdes.2005.02.012](https://doi.org/10.1016/j.nucengdes.2005.02.012).
- [44] M. S. Plesset and S. A. Zwick. "The Growth of Vapor Bubbles in Superheated Liquids". In: Journal of Applied Physics 25.4 (Apr. 1954). Number: 4, pp. 493–450. ISSN: 0021-8979.
- [45] V Prodanovic, D Fraser, and M Salcudean. "Bubble behavior in subcooled flow boiling of water at low pressures and low flow rates". In: International Journal of Multiphase Flow 28.1 (Jan. 1, 2002), pp. 1–19. ISSN: 0301-9322. DOI: [10.1016/S0301-9322\(01\)00058-1](https://doi.org/10.1016/S0301-9322(01)00058-1).
- [46] W. E. Ranz. "Evaporation from drops". In: Chemical Engineering Progress (Jan. 1, 1952). ISSN: 0360-7275.
- [47] Lord Rayleigh. "VIII. On the pressure developed in a liquid during the collapse of a spherical cavity". In: The London, Edinburgh, and Dublin Philosophical Magazine and Journal of Science 34.200 (Aug. 1, 1917). Publisher: Taylor & Francis _eprint: <https://doi.org/10.1080/14786440808635681>, pp. 94–98. ISSN: 1941-5982. DOI: [10.1080/14786440808635681](https://doi.org/10.1080/14786440808635681).
- [48] H. Reichardt. "Vollständige Darstellung der turbulenten Geschwindigkeitsverteilung in glatten Leitungen". In: Zeitschrift Angewandte Mathematik und Mechanik 31 (Jan. 1, 1951). ADS Bibcode: 1951ZaMM...31..208R, pp. 208–219. ISSN: 0044-2267. DOI: [10.1002/zamm.19510310704](https://doi.org/10.1002/zamm.19510310704).
- [49] Tingting Ren, Zhiqiang Zhu, Rui Zhang, Jiangwu Shi, and Changqi Yan. "Development of force balance model for prediction of bubble departure diameter and lift-off diameter in subcooled flow boiling". In: International Journal of Heat and Mass Transfer 161 (Nov. 1, 2020), p. 120245. ISSN: 0017-9310. DOI: [10.1016/j.ijheatmasstransfer.2020.120245](https://doi.org/10.1016/j.ijheatmasstransfer.2020.120245).
- [50] E. Ruckenstein. "On mass transfer in the continuous phase from spherical bubbles or drops". In: Chemical Engineering Science 19.2 (Feb. 1, 1964), pp. 131–146. ISSN: 0009-2509. DOI: [10.1016/0009-2509\(64\)85117-4](https://doi.org/10.1016/0009-2509(64)85117-4).

- [51] P. G. Saffman. "The lift on a small sphere in a slow shear flow". In: *Journal of Fluid Mechanics* 22.2 (June 1965), pp. 385–400. ISSN: 0022-1120, 1469-7645. DOI: [10.1017/S0022112065000824](https://doi.org/10.1017/S0022112065000824).
- [52] V. Scheiff, F. Bergame, J. Sebilleau, P. Ruyer, and C. Colin. "Experimental study of steady and transient subcooled flow boiling". In: *International Journal of Heat and Mass Transfer* 164 (Jan. 1, 2021), p. 120548. ISSN: 0017-9310. DOI: [10.1016/j.ijheatmasstransfer.2020.120548](https://doi.org/10.1016/j.ijheatmasstransfer.2020.120548).
- [53] Valentin Scheiff. "Etude expérimentale et modélisation du transfert de chaleur de l'ébullition transitoire". These de doctorat. Toulouse, INPT, Dec. 13, 2018.
- [54] L. E. Scriven. "On the dynamics of phase growth". In: *Chemical Engineering Science* 10.1 (Apr. 1, 1959), pp. 1–13. ISSN: 0009-2509. DOI: [10.1016/0009-2509\(59\)80019-1](https://doi.org/10.1016/0009-2509(59)80019-1).
- [55] Pengyu Shi, Roland Rzehak, Dirk Lucas, and Jacques Magnaudet. "Drag and lift forces on a rigid sphere immersed in a wall-bounded linear shear flow". In: *Physical Review Fluids* 6.10 (Oct. 28, 2021). Number: 10 Publisher: American Physical Society, p. 104309. ISSN: 2469-990X.
- [56] Rong Situ, Takashi Hibiki, Mamoru Ishii, and Michitsugu Mori. "Bubble lift-off size in forced convective subcooled boiling flow". In: *International Journal of Heat and Mass Transfer* 48.25 (Dec. 1, 2005), pp. 5536–5548. ISSN: 0017-9310. DOI: [10.1016/j.ijheatmasstransfer.2005.06.031](https://doi.org/10.1016/j.ijheatmasstransfer.2005.06.031).
- [57] Jia-Wen Song and Li-Wu Fan. "Temperature dependence of the contact angle of water: A review of research progress, theoretical understanding, and implications for boiling heat transfer". In: *Advances in Colloid and Interface Science* 288 (Feb. 1, 2021), p. 102339. ISSN: 0001-8686. DOI: [10.1016/j.jcis.2020.102339](https://doi.org/10.1016/j.jcis.2020.102339).
- [58] R. Sugrue and J. Buongiorno. "A modified force-balance model for prediction of bubble departure diameter in subcooled flow boiling". In: *Nuclear Engineering and Design* 305 (Aug. 15, 2016), pp. 717–722. ISSN: 0029-5493. DOI: [10.1016/j.nucengdes.2016.04.017](https://doi.org/10.1016/j.nucengdes.2016.04.017).
- [59] R. Sugrue, J. Buongiorno, and T. McKrell. "An experimental study of bubble departure diameter in subcooled flow boiling including the effects of orientation angle, subcooling, mass flux, heat flux, and pressure". In: *Nuclear Engineering and Design*. SI : CFD4NRS-4 279 (Nov. 1, 2014), pp. 182–188. ISSN: 0029-5493. DOI: [10.1016/j.nucengdes.2014.08.009](https://doi.org/10.1016/j.nucengdes.2014.08.009).
- [60] Rosemary M. Sugrue. "The Effects of Orientation Angle, Subcooling, Heat Flux, Mass Flux, and Pressure on Bubble Growth and Detachment in Subcooled Flow Boiling". PhD thesis. Massachusetts Institute of Technology, 2012.
- [61] G. E. Thorncroft, J. F. Klausner, and R. Mei. "An experimental investigation of bubble growth and detachment in vertical upflow and downflow boiling". In: *International Journal of Heat and Mass Transfer* 41.23 (Dec. 1, 1998), pp. 3857–3871. ISSN: 0017-9310. DOI: [10.1016/S0017-9310\(98\)00092-1](https://doi.org/10.1016/S0017-9310(98)00092-1).
- [62] G.E. Thorncroft, J.F. Klausner, and R. Mei. "Bubble forces and detachment models". In: *Multiphase Science and Technology* 13.3 (2001), pp. 35–76. ISSN: 0276-1459. DOI: [10.1615/multscientechn.v13.i3-4.20](https://doi.org/10.1615/multscientechn.v13.i3-4.20).
- [63] V. I. Tolubinsky and D. M. Kostanchuk. "VAPOUR BUBBLES GROWTH RATE AND HEAT TRANSFER INTENSITY AT SUBCOOLED WATER BOILING". In: International Heat Transfer Conference 4. Begel House Inc., 1970. DOI: [10.1615/IHTC4.250](https://doi.org/10.1615/IHTC4.250).
- [64] A. Urbano, S. Tanguy, and C. Colin. "Direct numerical simulation of nucleate boiling in zero gravity conditions". In: *International Journal of Heat and Mass Transfer* 143 (Nov. 1, 2019), p. 118521. ISSN: 0017-9310. DOI: [10.1016/j.ijheatmasstransfer.2019.118521](https://doi.org/10.1016/j.ijheatmasstransfer.2019.118521).
- [65] A. Urbano, S. Tanguy, G. Huber, and C. Colin. "Direct numerical simulation of nucleate boiling in micro-layer regime". In: *International Journal of Heat and Mass Transfer* 123 (Aug. 1, 2018), pp. 1128–1137. ISSN: 0017-9310. DOI: [10.1016/j.ijheatmasstransfer.2018.02.104](https://doi.org/10.1016/j.ijheatmasstransfer.2018.02.104).
- [66] W. G. J. Van Helden, C. W. M. Van Der Geld, and P. G. M. Boot. "Forces on bubbles growing and detaching in flow along a vertical wall". In: *International Journal of Heat and Mass Transfer* 38.11 (July 1, 1995), pp. 2075–2088. ISSN: 0017-9310. DOI: [10.1016/0017-9310\(94\)00319-Q](https://doi.org/10.1016/0017-9310(94)00319-Q).
- [67] L. Van Wijngaarden and D. J. Jeffrey. "Hydrodynamic interaction between gas bubbles in liquid". In: *Journal of Fluid Mechanics* 77.1 (Sept. 1976). Publisher: Cambridge University Press, pp. 27–44. ISSN: 1469-7645, 0022-1120. DOI: [10.1017/S0022112076001110](https://doi.org/10.1017/S0022112076001110).
- [68] Junsoo Yoo, Carlos E. Estrada-Perez, and Yassin A. Hassan. "Experimental study on bubble dynamics and wall heat transfer arising from a single nucleation site at subcooled flow boiling conditions – Part 1: Experimental methods and data quality verification". In: *International Journal of Multiphase Flow* 84 (Sept. 1, 2016), pp. 315–324. ISSN: 0301-9322. DOI: [10.1016/j.ijmultiphaseflow.2016.04.018](https://doi.org/10.1016/j.ijmultiphaseflow.2016.04.018).

- [69] Junsoo Yoo, Carlos E. Estrada-Perez, and Yassin A. Hassan. "Experimental study on bubble dynamics and wall heat transfer arising from a single nucleation site at subcooled flow boiling conditions – Part 2: Data analysis on sliding bubble characteristics and associated wall heat transfer". In: *International Journal of Multiphase Flow* 84 (Sept. 1, 2016), pp. 292–314. ISSN: 0301-9322. DOI: [10.1016/j.ijmultiphaseflow.2016.04.019](https://doi.org/10.1016/j.ijmultiphaseflow.2016.04.019).
- [70] Junsoo Yoo, Carlos E. Estrada-Perez, and Yassin A. Hassan. "Development of a mechanistic model for sliding bubbles growth prediction in subcooled boiling flow". In: *Applied Thermal Engineering* 138 (June 25, 2018), pp. 657–667. ISSN: 1359-4311. DOI: [10.1016/j.aplthermaleng.2018.04.096](https://doi.org/10.1016/j.aplthermaleng.2018.04.096).
- [71] Byong-Jo Yun, Andrew Splawski, Simon Lo, and Chul-Hwa Song. "Prediction of a subcooled boiling flow with advanced two-phase flow models". In: *Nuclear Engineering and Design*. SI : CFD4NRS-3 253 (Dec. 1, 2012), pp. 351–359. ISSN: 0029-5493. DOI: [10.1016/j.nucengdes.2011.08.067](https://doi.org/10.1016/j.nucengdes.2011.08.067).
- [72] L. Z. Zeng, J. F. Klausner, D. M. Bernhard, and R. Mei. "A unified model for the prediction of bubble detachment diameters in boiling systems—II. Flow boiling". In: *International Journal of Heat and Mass Transfer* 36.9 (Jan. 1, 1993), pp. 2271–2279. ISSN: 0017-9310. DOI: [10.1016/S0017-9310\(05\)80112-7](https://doi.org/10.1016/S0017-9310(05)80112-7).
- [73] Lanying Zeng, Fady Najjar, S. Balachandar, and Paul Fischer. "Forces on a finite-sized particle located close to a wall in a linear shear flow". In: *Physics of Fluids* 21.3 (Mar. 2009). Publisher: American Institute of Physics, p. 033302. ISSN: 1070-6631. DOI: [10.1063/1.3082232](https://doi.org/10.1063/1.3082232).
- [74] Pei Zhou, Shiyang Hua, Cai Gao, Dongfang Sun, and Ronghua Huang. "A mechanistic model for wall heat flux partitioning based on bubble dynamics during subcooled flow boiling". In: *International Journal of Heat and Mass Transfer* 174 (Aug. 1, 2021), p. 121295. ISSN: 0017-9310. DOI: [10.1016/j.ijheatmasstransfer.2021.121295](https://doi.org/10.1016/j.ijheatmasstransfer.2021.121295).
- [75] Pei Zhou, Ronghua Huang, Sheng Huang, Yu Zhang, and Xiaoxuan Rao. "Experimental investigation on bubble contact diameter and bubble departure diameter in horizontal subcooled flow boiling". In: *International Journal of Heat and Mass Transfer* 149 (Mar. 1, 2020), p. 119105. ISSN: 0017-9310. DOI: [10.1016/j.ijheatmasstransfer.2019.119105](https://doi.org/10.1016/j.ijheatmasstransfer.2019.119105).
- [76] Novak Zuber. "The dynamics of vapor bubbles in nonuniform temperature fields". In: *International Journal of Heat and Mass Transfer* 2.1 (Mar. 1, 1961), pp. 83–98. ISSN: 0017-9310. DOI: [10.1016/0017-9310\(61\)90016-3](https://doi.org/10.1016/0017-9310(61)90016-3).
- [77] H. C. Ünal. "Maximum bubble diameter, maximum bubble-growth time and bubble-growth rate during the subcooled nucleate flow boiling of water up to 17.7 MN/m²". In: *International Journal of Heat and Mass Transfer* 19.6 (June 1, 1976), pp. 643–649. ISSN: 0017-9310. DOI: [10.1016/0017-9310\(76\)90047-8](https://doi.org/10.1016/0017-9310(76)90047-8).

DECLARATION

Put your declaration here.

Paris, December 2022

Luc Favre

COLOPHON

This document was typeset using the typographical look-and-feel `classicthesis` developed by André Miede. The style was inspired by Robert Bringhurst's seminal book on typography "The Elements of Typographic Style". `classicthesis` is available for both L^AT_EX and LyX:

<https://bitbucket.org/amiede/classicthesis/>

Happy users of `classicthesis` usually send a real postcard to the author, a collection of postcards received so far is featured here:

<http://postcards.miede.de/>

